Developing a microfluidic blood preparation device for ATR-FTIR spectroscopy

EngD Thesis

Pretheepan Radhakrishnan

Continuum Mechanics and Industrial Mathematics

Department of Mathematics and Statistics

James Weir Fluids Laboratory

Department of Mechanical and Aerospace Engineering

Doctoral Training Centre in Medical Devices & Health Technologies

Department of Biomedical Engineering

University of Strathclyde

Glasgow 2021

Declaration

This thesis is the result of the author's original research. It has been composed by the author and has not been previously submitted for examination which has led to the award of a degree.

Signed:

PRadhakrishnan

Date: 18th September 2021

Acknowledgements

I wish to thank all the people who aided in the completion of this project. Firstly, I would like to express my gratitude to my supervisor, Professor Nigel. J. Mottram, not only for your expertise and guidance in numerical modelling but also the constant support when times were difficult. It is whole-heartedly appreciated that your great advice during this period, which proved monumental towards the completion of this thesis.

I am also grateful for my co-supervisor Dr Mónica S. Oliveira for providing quality feedback on my understanding of microfluidics and the experimental methods is used. I really appreciate the time you spent critiquing my work, giving me the opportunity to improve. I would like to my special regards to Dr Cerys Jenkins for being enthusiastic and supportive when reviewing my spectroscopy work as well as showing concern for my well-being.

Special mention goes to Dr Joana Fidalgo for providing training in fabricating microfluidic channels using soft lithography and on how to carry out microfluidic experiments. I am grateful to you for designing the moulds used in my experiments. Appreciation is also due to Zannib Panni for providing fresh human plasma a serum samples for experiments using ATR-FTIR spectroscopy. I would also like to thank the volunteers for offering blood for these experiments.

I would like to thank the Doctoral Training Centre in Medical Devices & Health Technologies for providing me the opportunity to undertake further study and to the EPSRC for providing the funding. A special thanks for Carol Mcinnes for providing administrative support when I was struggling with the completion of this project.

Finally, I would like to express my gratitude to Eloise A. Lynn for curing my aversion to writing this thesis, without which I might not have finished.

Abstract

There are limited healthcare resources in remote parts of the world and ATR-FTIR spectroscopy has the potential to be used for point-of-care (POC) diagnostics in these locations, but lacks of a portable blood sample preparation method. This thesis looks at development of a microfluidic device that would process a single blood sample in order to prepare serum, infected/damaged red blood cells (RBCs), white blood cells (WBCs) and circulating tumour cells (CTCs) for analysis using ATR-FTIR spectroscopy. After exploring a range of microfluidic blood separation methods and manufacturing techniques, a 4-stage design concept is presented in Chapter 2. ATR-FTIR spectroscopy and bespoke Matlab codes are used, in Chapter 3, to evaluate the serum output quality requirement. A series of experiments to determine how to produce serum was carried out, using horse blood. After which, the difference between the spectra from human plasma and serum was investigated, and concluded that plasma was a better output for a POC application. In Chapter 4, a design tool for creating a microfluidic module that separates the diagnostic outputs from healthy RBCs was being developed. COMSOL Multiphysics and Matlab was used to develop a continuum effective medium (CEM) model that simulated the creation of a cell-free layer (CFL), from which the diagnostic outputs could be collected. The CEM model was compared with experiments, which used expansion-contraction geometries manufactured using soft lithography, and it has been shown that this CEM model can simulate the CFL, although more work is needed to fully validate the model. The research carried out in this project has shown that further work is needed in the ATR-FTIR spectroscopy field in order to ascertain appropriate design requirements to be able to design and develop an efficient device.

Keywords: blood; ATR-FTIR spectrscopy; sample preparation; microfluidics; numerical modelling; point-of-care.

Contents

List of Abbreviations

μTAS micro total analysis systems.

ABS acrylonitrile butadiene styrene / minimum absorbance value.

ATR attenuated total reflectance.

BASW bulk accoustic standing waves.

CAD computer aided design.

CCE counterflow centrifugal elutriation.

CEM continuum effective medium.

CFL cell-free layer.

ChD channel depth.

CLIP continuous liquid interface production.

CoM centre of mass.

CTC circulating tumour cell.

D_C critical diameter.

DEP dielectrophoresis.

DiZnSe diamond zinc selenide.

DLD deterministic lateral displacement.

DLP digital light processing.

DMD digital micromirror device.

DPD dissipative particle dynamics.

DTGS deuterated triglycine sulfate.

EDTA ethylenediamine tetraacetic acid.

ELISA enzyme linked immunosorbant assay.

EM electromagnetic radiation.

FACS fluorescent activated cell sorting.

FDM fused deposition modelling.

FEA finite element analysis.

FFT fast Fourier transform.

FL Fåhræus-Lindqvist.

FPA focal plane array.

FTIR Fourier transform infrared.

HCT haematocrit.

HF hydrophoretic focusing.

IF inertial focusing.

IR infrared.

IRE internal reflection element.

LA linear array.

LBM lattice Boltzmann method.

LC-SLM liquid crystal spatial light modulators.

LOAD lab-on-a-disc.

MACS magnetic activated cell sorting.

List of Abbreviations

MCT mercury cadmium telluride.

MEMS micro-electromechanical systems.

MJM multijet modelling.

N_a period of the array.

nDEP negative dielectrophoresis.

NHS National Health Service.

PAP print and peel.

PBS phosphate buffered saline.

PC-DFA principle component discriminant functional analysis.

PCA principle component analysis.

PDE partial differential equation.

pDEP positive dielectrophoresis.

PDMS polydimethylsiloxane.

PE percentage explained.

PET polyethelene terephthalate.

PFF pinch flow fractionation.

PLA poly-lactic acid.

PMMA poly-methylmethacrylate.

POC point-of-care.

PR photoresist polymer.

QT quality test.

RBC red blood cell.

SAR separation and recombination.

SD standard deviation.

SIRE silicon internal reflection element.

SLA stereolithography.

SLM spatial light modulators.

SPH smoothed particle hydrodynamics.

SSAW surface standing acoustic waves.

TF tissue factor.

UV ultraviolet.

vWF von Willibrand factor.

WBC white blood cell.

ZF Zweifach-Fung.

List of Symbols

a particle radius.

b path length / shear exponent.

C concentration.

c speed of light.

$C_{\mathbf{mig}}$ coefficient of migration.

C_r contraction ratio.

δ retardation.

E energy.

H channel height.

h Plank Constant.

I intensity.

k force constant.

k_B Boltzmann constant.

λ wavelength / eigenvector.

L_c length of contraction.

m mass.

μ_w viscosity of water.

ν frequency.

P pressure.

Pe Peclet number.

ϕ volume fraction.

Q volumetric flow rate.

Re Reynolds number.

Re_w Reynolds number of fluid.

ρ_p density of particles.

ρ_w density of water.

SNR1 signal to noise ratio 1.

SNR2 signal to noise ratio 2.

St Strouhal number.

T_c temperature.

$\boldsymbol{u}$ velocity field.

W channel width.

WVR1 water vapour ratio 1.

WVR2 water vapour ratio 2.

Please note: Some symbols are used as standard in both infrared spectroscopy and fluid mechanics fields, therefore have multiple descriptions.

List of Figures

List of Figures

List of Figures

List of Figures

List of Tables

Chapter 1: Introduction

Healthcare is an essential service that is insufficient or lacking in many parts of the world. This is expected to get worse due to increasing population and increasing redistribution of resources to the "few", since the 1980's. One way to improve the spread of healthcare is to reduce the economic cost; this includes material cost of equipment as well as the cost of the training needed for individuals to administer tests. Significant money is spent on donating equipment to the developing world but a majority of which ends up broken with users lacking access to repair facilities [Perry and Malkin, 2011]. Therefore, devices have to be designed specifically for an application in order to have sustainable impact. Cheaper mass production technology can reduce the cost per test making the test disposable and reducing the need for rationing. The economic skills cost is indicated by the lack of trained healthcare professional in the developing world, which is a serious concern for world health [Naicker et al., 2009], although fully automated devices will overcome this lack of skills in local populations and may be integrated into a future cyber healthcare framework. A cyber healthcare network would allow low skilled physicians in local communities to have access to specialists [Bagula et al., 2018]. One technology that could help address this need is an automated sample preparation device combined with infrared spectroscopy. This chapter will explain the use of blood as the chosen diagnostic sample and the method for diagnostics using attenuated total reflectance - Fourier transform infrared (ATR-FTIR) spectroscopy.

ATR-FTIR spectroscopy , which will be discussed in more detail later in this chapter (Section1.2), has been shown to have the potential for the detection of specific diseases, where in most investigations serum is used due to the fact that it is a standard sample type taken for existing diagnostic tests and, therefore stocks of serum samples exist in biobanks [Baker et al., 2016]. Serum has been used for

detection of a variety of multifactorial diseases with cancer being of particular interest; i.e. brain [Hands et al., 2014], liver [Zhang et al., 2013], ovarian [Gajjar et al., 2013; Owens et al., 2014], endometrial [Gajjar et al., 2013]. Neurological conditions can also result in a detectable change in serum protein content i.e. depression [Depciuch et al., 2016], bipolar and schizophrenia [Öğrüç Ildız et al., 2016]. ATR-FTIR spectroscopic serum analysis also has the potential to be used for infectious diseases such as HIV/AIDS [Sitole et al., 2014] and dengue virus [Santos et al., 2017]. As well as serum analysis, the interrogation of cells using ATR-FTIR spectroscopy is also a growing area of interest [Sabbatini et al., 2017], for instance this type of analysis would be useful since red blood cells (RBCs) have been used in the early detection of malaria [Khoshmanesh et al., 2014]. The many types of white blood cells (WBCs), given in Section 1.1.3, also respond in a detectable way to different diseases and Alam et al. [2004] also showed that is was possible to detect activation of living macrophages using ATR-FTIR spectroscopy. It may therefore be possible to qualitatively identify the change in activated WBCs numbers by type, thus narrowing the disease type to specific pathogen type such as viruses, bacteria, parasites etc. The presence of circulating tumour cells (CTCs) is also a good indicator of cancer and such cells break from the tumour and enter the blood stream, potentially forming a secondary cancer known as a metastasis. Minnes et al. [2017] therefore used ATR-FTIR spectroscopy to look at the membrane fluidity of melanoma cells as an indicator of metastatic potential. There is therefore a potential to identify the origin of the CTCs based on the spectral responses of the different cell types. This type of analysis would allow better targeting of further investigations.

The aim of this project is to evaluate microfluidic technologies to produce a potential design of a blood preparation device that can take a single blood sample and produce serum, infected/damaged RBCs, WBCs and CTCs for ATR-FTIR spectroscopic diagnostics. A design that can be used in conjunction with the

potential adoption of ATR-FTIR spectroscopy as point-of-care (POC) diagnostic tool for remote locations and in crisis deployment,

1.1 Blood

Blood travels through the cardiovascular system maintaining an optimal internal environment. This is achieved by transporting nutrients and heat around the body, while removing waste and thus maintaining homeostasis. As the majority of cells interact with blood, disease markers from around the body gather in the cardiovascular system. With blood being relatively easy to collect, it is the main source of diagnostic material for testing. Blood, however is a complex fluid; it consists of a variety of suspended particles with different sizes, mechanical properties and biochemical responses. Descriptions of the main relevant components and functions; plasma and plasma proteins, RBCs, WBCs, immunoglobulins and complement system, and finally coagulation will be presented in this section.

1.1.1 Plasma and Plasma Proteins

The majority of blood consists of plasma (55%), which is itself composed of water (92%), plasma proteins (7%) and other solutes (1%) [Martini et al., 2015]. Considering first the solutes, which consist of organic nutrients, electrolytes and organic waste, where the polar organic nutrients, such as glucose, are dissolved in the plasma and the non-polar, such as cholesterol are carried by globular proteins. The flow of the blood therefore carries nutrients via advection from the digestive system or storage sites, such as the liver, to the cells. Electrolytes maintain the extracellular ion balance of the tissue fluid, which is vital for regulating transport across the cell membranes and a properly functioning nervous system. Organic wastes, such as urea, are products of metabolic processes and are transported to kidneys for excretion. Imbalances in any of these solutes can lead to disease and

pre-symptomatic detection would be ideal.

Returning now to plasma proteins, which make up 7% of blood, in this work they will be defined as proteins that carry out a function in the circulatory system. Messenger proteins, which allow communication between different tissues via the circulation, and proteins that leak into the circulation due to damage will be classified separately [Anderson and Anderson, 2002]. The three main categories of plasma proteins are albumins, globulins and fibrinogen. The primary role of albumins is maintaining the osmolarity (the solute concentration) of the plasma. They are also important in transporting non-polar small molecules such as steroid hormones and fatty acids. Globulins, such as apolipoproteins and metalloproteins, are proteins that form tertiary structures with non-polar residual groups at the centre and polar groups on the surface that interact with water. The general role of these proteins is the transport of molecules around the circulation without being excreted. The first type of globulins, apolipoproteins, transport lipids and triglycerides and form lipoproteins. Lipoproteins are thought to play a role in obesity related disease, such as diabetes [Mackey et al., 2015]. The second type of globulins, metalloprotein, transport metal ions, for example transferrin transports Fe^{2+}. A specialised type of globular proteins are the immunoglobulins (antibodies). Immunoglobulins are a significant part of the immune response and will be discussed in Section 1.1.4. Some of the soluble proteins are coagulation proteins, for example fibrinogen and coagulation factors such as factor IX, which will be discussed later in Section 1.1.5. A variety of conditions can affect plasma protein levels and cause proteins not normally found in plasma to be present and are used as diagnostic biomarkers for disease and infections. As an example, a decrease in albumin is an indicator of chronic liver failure [Dasgupta and Wahed, 2014]. Also, tumour cells secrete proteins (secretomes) into the extracellular space and end up in bodily fluids where they can be detected by mass spectroscopy [Patel et al., 2014]. Cell death or damage, such as a myocardial infarction, results in the

leakage of cytoplasmic proteins such as myoglobin, cardiac troponin and creatine kinase into the plasma [Anderson and Anderson, 2002]. Microbial and parasitic infections can introduce proteins, in a similar fashion to tumour cells, but these proteins are not naturally found in the host. The proteins that are not normally present in the blood are therefore diagnostically important biomarkers and are the foundation for assay-based diagnostic tests [Dasgupta and Wahed, 2014].

1.1.2 Red blood cells

Red blood cells (RBCs), also known as erythrocytes, are the most common cells found in blood, being 45% of whole blood and 99% of the non-liquid components (Martini et al. 2015). RBCs are derived from hematopoietic stem cells found in the bone marrow in a process called erythropoiesis (Figure 1.1) [Munker, 2007] and their primary role is to transport oxygen from the lungs to the cells in the rest of the body. In hypoxic conditions erythropoiesis is stimulated by erythropoietin, which is synthesised in the kidneys and this increases the rate of RBC maturation. During the final stages of development, RBCs need dietary nutrients such as iron, vitamin B12 and folic acid, and deficiency in any of these nutrients can lead to anaemia [Erber, 2011]. The final stage of a RBC life-cycle is eryptosis whereby the cell membrane expresses proteins that trigger phagocytosis of macrophages found in the spleen, liver and bone marrow. The haem proteins are broken down into Fe ions and biliverdin, with the iron transported via transferrin back to the bone marrow and the biliverdin transported to the liver via albumin where it is excreted in bile as bilirubin. In normal function the rate of erythropoiesis matches the rate of eryptosis and divergence from a balance is used in diagnostic indicator of disease.

The mature RBC is an anucleated biconcave disc, around 8 µm in diameter. The biconcave shape allows for a higher surface area to volume ratio, which improves the diffusion rate of oxygen, allowing rapid uptake of oxygen in the alveoli and

release in the tissues. The lack of nucleus increases the amount of haemoglobin contained in the cell and therefore its oxygen carrying capacity. The shape also increases the flexibility of RBCs, allowing them to deform when moving through capillaries and branching vessels. RBCs can also stack in capillaries smaller than 0.3mm, which result in the plasma forming a layer between the RBCs and the wall, effectively reducing the haematocrit level. This results in a reduction in the apparent viscosity in small capillaries and is known as the Fåhræus-Lindqvist (FL) effect [Haynes, 1960]. This effect is vital for RBCs *in vivo*. In the small arterioles and capillaries if the viscosity did not reduce the high resistance of these small vessels, then very high pressure would be required to maintain flow.

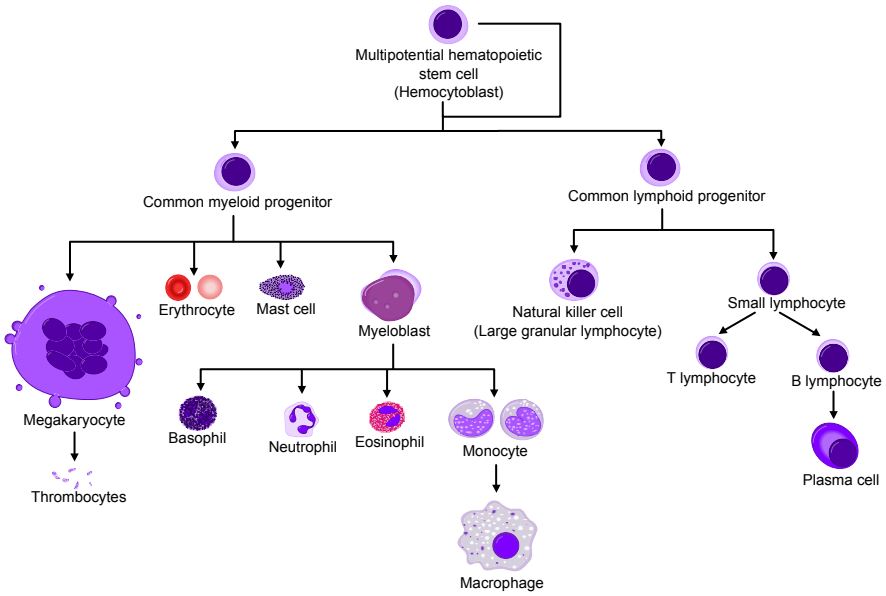

Figure 1.1: Representation of blood cells and their lineage. Reproduced from Haggstrom et al. [2014].

1.1.3 White blood cells

Another major cell type are white blood cells (WBCs) also known as leukocytes. WBCs are also derived from the hematopoietic stem cells (Figure 1.1) but exposure to different growth factors, such as interleukin 3, causes the cell to

differentiate into the various WBC types [Clark and Kamen, 1987]. WBCs can be generalised into two types; granulocytes and mononuclear leukocytes. Granulocytes are the cells that contain enzymes that target pathogens as well as release inflammatory mediators into the blood stream. Granulocytes include neutrophils, eosinophils and basophils, each of which has specific roles; the neutrophils make up the majority of all WBCs (40%-75%), and are responsible for capturing and killing microorganisms via phagocytosis, engulfing the foreign body and digesting it, as part of the innate immune system [Parham, 2005]; eosinophils respond to parasitic attacks such as helminth worms, this pathway is also responsible for the response to allergens [Martini et al., 2015]; basophils are extremely rare (1% of circulating leukocytes) and are involved with immunoglobulin mediated immune reactions [Falcone et al., 2000]. Mononuclear leukocytes consist of lymphocytes and monocytes. Lymphocytes are further categorised into B and T cells. The B cells are activated by an antigen and the response results in the secretion of immunoglobulins whereas the T cells are involved in cell destruction. Monocytes when leaving the blood stream differentiate to macrophages if located in internal tissue or dendritic cells if exposed to the external environment.

1.1.4 Immunoglobulins and complement system

Immunoglobulins are proteins that specialise in binding extracellular pathogens and toxins. There are five classes of immunoglobulins; IgA, IgD, IgE, IgG and IgM. The structure determines the class of immunoglobulin (Figure 1.2) with different classes having different heavy chain regions and different roles. IgM, IgG and IgA are the predominant immunoglobulins found in the blood, lymph and tissue fluid. IgM is the initial responding immunoglobulin for blood borne infection. It has a pentameric nature that allows the binding of multiple pathogens found in the blood. This reduces the microorganism growth rate and the new complex is too large to pass out of the blood vessels, which reduces the spread rate of the

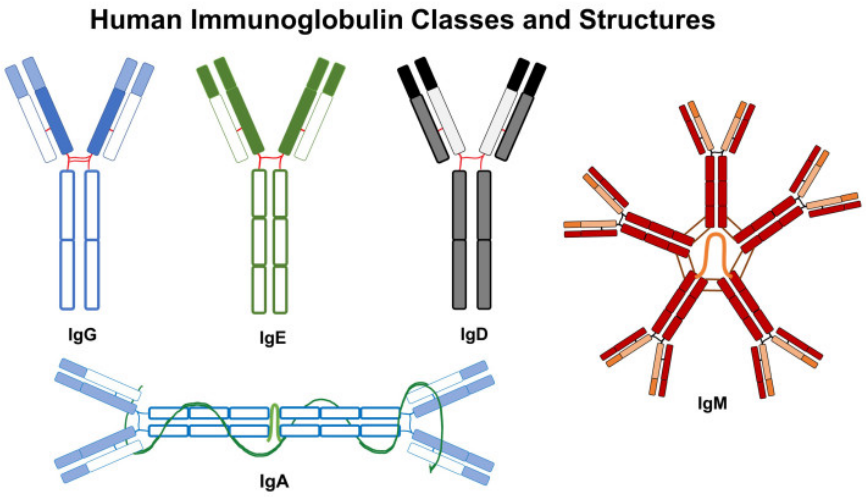

Figure 1.2: Schematic of the various classes of immunoglobulins reproduced with permission from Leehan [2018].

infection. After this initial response IgG becomes the dominant immunoglobulin. IgM and IgG are extremely important in combating septicaemia, if microorganisms have free access to the circulatory system they can spread throughout the system and impede the function of multiple organs. IgA are located on the apical surfaces of the epithelia. Both IgG and IgA have high affinity for microbial toxins and animal venom, and are used to neutralise them before cell damage. As immunoglobulins are specific for its antigen, immunoglobulin epitope design has become a big industry for detecting specific molecules in assays; such as enzyme linked immunosorbant assay (ELISA), whose market is projected to grow from USD 437.6 million in 2016 to USD 547.6 million by the end of 2022 [Anonymous, 2017]. For fluorescent labelling of specific cells, the global fluorescent in situ hybridization (FISH) probe market is expected to reach USD 1.73 billion by 2022 [Anonymous, 2016].

Complement proteins are specialised proteins that aid immune response via opsonisation, the detection and targeting of pathogens for phagocytosis. Comple-

ment proteins can also directly targeting bacterial cell membranes causing bacterial lysis. They are activated via either the classical pathway, lectin pathway or the alternative pathway. The classical pathway is the immunoglobulin, such as IgM and IgG, activated pathway. Immunoglobulins that attach to pathogens cause enzymatic reactions that activate the complement cascade. The other two pathways are not immunoglobulin mediated: the lectin pathway involves the binding of the plasma protein, mannose-binding lectin, to the pathogen surface. Finally the alternative pathway is where the local environment caused by the pathogen is conducive to complement activation [Parham, 2005].

1.1.5 Coagulation

Coagulation is a mechanism that prevents blood loss (hemostasis) when vessels are damaged. Coagulating blood forms a clot (thrombus) over the site of injury, sealing the internal environment from the external. Platelets, also known as thrombocytes, are the main cell type involved in regulating coagulation. They are formed by the megakaryocytes shedding; discoid, anuclear cells with diameters of 2-4 µm break of the main cell [Martini et al., 2015]. Their function arises from the complex signalling pathways made possible by the multitude of different receptors in the cell membrane. These cells adhere to the site of injury (primary hemostasis) and requires the presence of von Willibrand factor (vWF), which binds collagen in the exposed subendothelium to the glycoprotein Ib found in platelet cell membrane. The platelets are then activated by the bound collagen resulting in structural deformation in the form of filopodia. The filopodia then provide sites for binding the injured epithelium, other platelets and growing the fibrin network [Fasano and Sequeira, 2017]. Activated platelets also release stored proteins as part of the coagulation cascade (Figure 1.3). The coagulation cascade can occur via two pathways, extrinsic or intrinsic, followed by the common pathway, as shown in Figure 1.3, which are mediated by proteins known as factors.

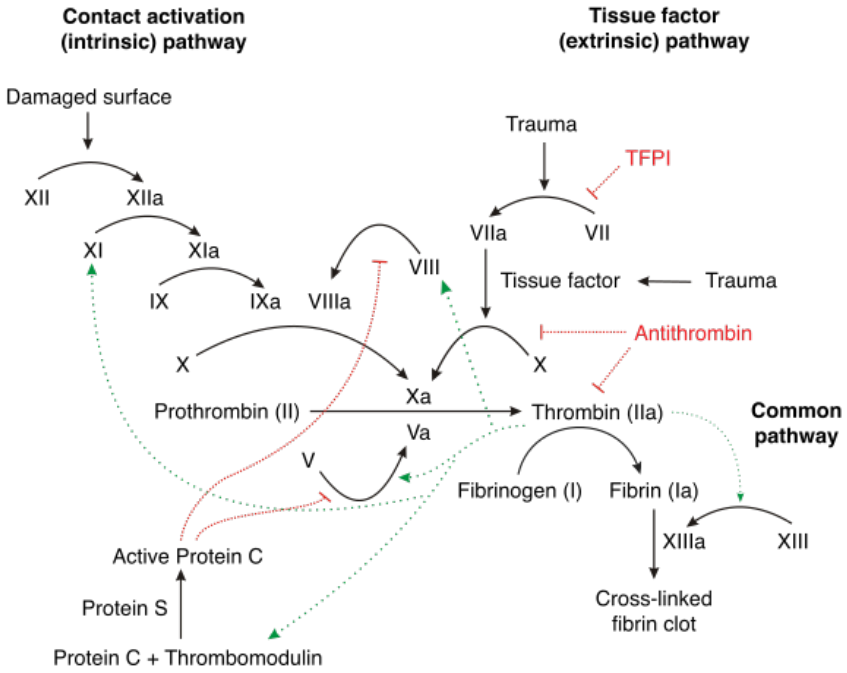

Figure 1.3: Representation of the coagulation pathways. (Reproduce from D [2007]).

The extrinsic pathway is initiated by the activation of tissue factor (TF) which indicates the presence of exposed tissue to the blood. TF is a membrane protein that binds Factor VIIa and this complex activates Factor X to Factor Xa which is then part of the common pathway. The intrinsic pathway is triggered by exposure to foreign surfaces via the generation of Factor XIIa. The common pathway starts at the activation of Factor X to Factor Xa. Factor Xa binds to Factor V which leads to the formation of thrombin (Factor IIa) from prothrombin. Thrombin cleaves fibrinogen into fibrin monomers, which are then polymerised into a vast network that cross-link and bind passive elements such as RBCs to form the clot. The cascade reaction activity is increased 1000-fold when reactions occurs on cell surfaces, the binding to which is mediated by the presence of calcium [Monroe and Hoffman, 2014]. Each activated factor can catalyse multiple reactions resulting in a rapid amplification of the response (hence cascade) to a small signal.

The response of blood to artificial surfaces via the intrinsic pathway is a problem for controlling blood flow through a potential microfluidic device. Therefore, a variety of anticoagulants can be potentially used to inhibit coagulation; such as heparin, ethylenediamine tetraacetic acid (EDTA) and sodium citrate. Heparin is a glycosominoglycan that is used as an intravenous anticoagulant. It works by activating antithrombin which inhibits thrombin activity and protamine sulphate can neutralise the effect through electrostatic binding [Bromfield et al., 2013]. EDTA and citrate are calcium chelators: they bind free calcium ions. Calcium as stated earlier is required for increasing the rate of cascade reactions, therefore removing calcium prevents the cascade progression.

1.1.6 Clinical considerations

Majority of clinics and GP surgeries in the National Health Service (NHS) do not process blood on site. Samples are taken in variety of sample tubes with different additives and sent to central haematology lab in local hospital with a request form with desired tests. The NHS recommends that samples are kept at room temperature and transfer in the next transport which occurs daily. If transport is missed, then some types of sample can be refrigerated overnight but the test results lose reliability and storage overnight is not possible for some tests. The details of which are shown in Table 1.1 [Maunsell-Browne, 2019]. But this service is unavailable in the developing world, especially in remote regions and as ATR-FTIR spectroscopy is not used in the NHS either, the current storage procedures for NHS test are not applicable.

Table 1.1: Overnight sample storage conditions for different types of blood test

Test type	Sample types	Overnight storage
Biochemistry	Lithium heparin and serum	Centrifuged and refrigerated (4-8°C)
Biochemistry	fluoride oxalate	Not centrifuged and refrigerated (4-8°C)
Haematology	EDTA and citrate	Not centrifuged and refrigerated (4-8°C)

1.2 Fourier transform infrared (FTIR) spectroscopy

In the previous section we described how the components of blood can be indicators of disease. In this section we will describe one potential method of detecting these indicators, ATR-FTIR spectroscopy.

1.2.1 Interaction of Infrared Light and Matter

This first section will introduce the fundamentals of infrared light and when samples are exposed to infrared (IR) light, how the measured absorbance is used as the mode of discrimination between samples. Finally we explain that molecular vibrations in covalent bonds cause the variation in absorbance spectra between samples.

1.2.1.1 Electromagnetic Radiation

Electromagnetic radiation (EM) is the energy transmitted as a wave passes by way of the orthogonal interaction of oscillating electric and magnetic fields. An EM wave is defined in terms of its wavelength (λ) or frequency (ν), which are related, since the speed of light (c) is constant, using

$$\nu = \frac{c}{\lambda}. \tag{1.1}$$

Quantum theory explains how electromagnetic waves can be modelled as particles called photons, which contain the discrete amount of energy (E) determined by the Planck model

$$E = h\nu = \frac{hc}{\lambda}, \tag{1.2}$$

where h is the Planck constant, 6.6×10^{-34} J s.

The infrared region of the EM spectrum is located between microwave and the visible spectrum, and Fourier transform infrared (FTIR) spectroscopy uses the mid infrared region found between 2.5 µm and 25 µm, or in wavenumbers, $v = \frac{1}{\lambda}$, between 4000 cm^{-1} and 400 cm^{-1}. Wavenumbers (number of cycles per cm) are used instead of wavelength (length of one cycle) in vibrational spectroscopy as wavenumbers are proportional to the transition energy [Barth, 2007].

1.2.1.2 Absorbance

When a sample is exposed to IR light some of the energy is absorbed by the sample, the amount of which can be calculated using the Beer-Lambert law. The intensity (I) detected of a specific wavelength is given by

$$I = I_0 e^{-\epsilon(\lambda)bC}, \tag{1.3}$$

where I_0 is the intensity of the source, $\epsilon(\lambda)$ is the molar absorption coefficient, b is the path length and C is the concentration of the analyte. Absorbance is the measure of the proportion of the source intensity that does not reach the detector and is given by

$$A = \log\left(\frac{I_0}{I}\right) = \epsilon(\lambda)bC. \tag{1.4}$$

To remove the effects of the background environment, such as CO_2 absorbance, and effects of the spectrometer, the absorbance of the sample is calculated in practice, by removing the reference intensity, which was taken without the presence

of the sample, from the intensity measured using a sample. To find the analyte concentration from an experiment, it is necessary to know the molar absorption coefficient at specific wavelengths, which can be determined by the molecular vibrations of the molecules in the sample.

1.2.1.3 Molecular Vibrations

In a molecule, certain chemical functional groups can be identified by their characteristic vibrational frequency. In complex organic molecules the vibration wavenumber of the functional groups can vary between similar molecules, and therefore these highly discriminatory wavenumbers appear in the fingerprint band (1800-1000 cm^{-1}) of wavenumbers and are used to identify biological macromolecules.

The total internal energy of molecules can be divided into electronic, vibrational, rotational and translational [Coates, 2006]. Translational energy is the kinetic energy of the molecule moving in space, rotational energy is the energy associated with rotation around a point, vibrational energy drives the movement of the atoms about the mean bond positions and electronic energy refers to the energy transitional state of the electrons.

A non-linear molecule of N atoms has 3N degrees of freedom, 3 of which are translational in the 3 global directions, 3 rotational about the global axes leaving 3N-6 degrees for the vibration modes [Griffiths and De Haseth, 2007]. For linear molecules, since the rotation along the bond axis does not change the orientation, the number of degrees of freedom is 3N-5. In order for a molecule to be IR active the vibrations have to result in an electric dipole moment as shown in Figure 1.4, which only occurs when there is a net change in charge distribution due to the vibration. As not all vibrations produce an electric dipole moment (Figure 1.4b), and some vibrations produce the same electric dipole moment (Figure 1.4c and 1.4d), the number of IR active vibrational modes is less than the number of actual

(a) Asymmetric Stretching (b) Symmetric Stretching

(c) Scissoring (in plane) (d) Scissoring (perpendicular to plane)

Figure 1.4: Vibrational modes of molecular bonds that can cause electric dipole moment.

modes. The vibrational energy can be calculated by modelling the covalent bonds as springs, using Hooke's law, and the characteristic frequency of which can be given as

$$\nu = \frac{1}{2\pi c}\sqrt{\frac{k}{m}}, \tag{1.5}$$

where k is the force constant, m is the reduced mass $(m_1 m_2/(m_1 + m_2))$, where m_1 and m_2 are the masses of the atoms at the ends of the bond and ν is the vibrating frequency [Coates, 2006]. The vibrational energy levels, $V_{i\nu}$ are discrete and can be described using a harmonic oscillator model,

$$V_{i\nu} = hv_i\Big(\nu_i + \frac{1}{2}\Big), \tag{1.6}$$

where v_i is the fundamental frequency and ν_i is the vibrational quantum number of the ith mode. Modelling bonds as a harmonic oscillator has limitations since the repulsive and attractive forces that are experienced at the extremes of the vibration are not included. An improved model of the bond vibrational energy levels use an anharmonic oscillator model, where the energy levels are given by

$$V_{i\nu} = hv_i\Big(\nu_i + \frac{1}{2}\Big) + hv_i x_i\Big(\nu_i + \frac{1}{2}\Big)^2 \tag{1.7}$$

where x_i is the anharmonicity constant, is dependent on the size of the atoms that make up the bond. The effect of anharmonicity is that transitions between

energy levels greater that ± 1, known as overtones ($\Delta\nu_i = 2, 3..$) appear in mid-infrared spectrum along with the fundamental frequency. It is the absorbance of light energy into the excitation of these modes that will be detected. A molecule will have a precise set of vibrational modes then, when excited, this will lead to a characteristic absorbance at specific frequencies of light.

1.2.2 Instrumentation

A FTIR spectrometer is composed of an IR source, an interferometer and the detector. The most common IR source for FTIR spectroscopy is known as a globar source which produces IR waves of a wide spectrum. The interferometer, which will be explained in more detail in the next section, converts the wide spectrum of IR waves into beams of discrete wavenumbers which can then be cycled over a range of wavenmubers. The discrete beam is then sent to the sample via an internal reflection element (IRE), when using ATR-FTIR spectroscopy and after interacting with the sample the returning beam is measured at a detector. Common detectors used in FTIR spectroscopy, such as deuterated triglycine sulfate (DTGS) and mercury cadmium telluride (MCT), are single element detectors that produce an average spectra across the entire sample. The DTGS crystal generates a charge when exposed to IR, which is then detected by a parallel set of electrodes. MCT is more sensitive but requires the use of liquid nitrogen to keep the detector cool and therefore, would not be suitable for a POC application. The sampling rate of the detector is in time with the interferometer, so that absorbance measurements are generated from a range of IR wavenumbers.

1.2.2.1 Michelson interferometer

The Michelson Interferometer is the fundamental part of a FTIR spectrometer, splitting the beam of radiation into two and recombining them with a path length difference. Figure 1.5 shows a schematic of the interferometer, which is composed

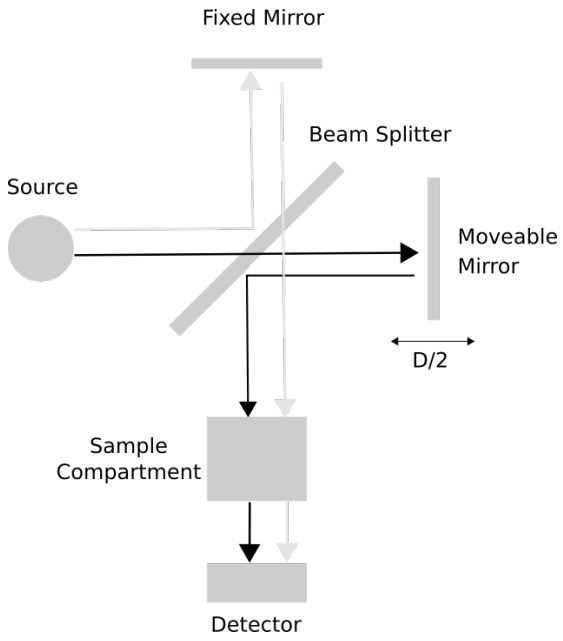

Figure 1.5: Schematic of a Michelson Interferometer

of a beamsplitter and two mirrors, one of which is fixed and the other movable. In an ideal system the beamsplitter will reflect 50% of the energy to the fixed mirror and transmit 50% to the moving mirror. The path difference, known as the retardation (δ), between the two beams then causes interference. When the movable mirror is at the same distance away from the beamsplitter as the fixed, $\delta = 0$, the waves interfere constructively (in phase) and pass to the detector. Considering a monochromatic source, and setting the retardation to half the wavelength, will result in the destructive interference, where the two beams are out of phase and the energy returns to the source. Therefore, the intensity at the detector is a function of retardation.

The retardation is controlled via a constant speed motor or a stepper motor and in either case the position is recorded in terms of time. Fourier transform infrared spectroscopy has its name as the Fourier transform is used to produce the intensities as a function of wavenumber from a time based signal. As it is impractical to record the response of a continuum, the output needs to be

sampled resulting in a discrete output and therefore the fast Fourier transform (FFT) algorithm is naturally used. The constant characteristics, such as intensity of the source, and of the signal are taken into account by taking the background reference spectrum mentioned in Section 1.2.1.2.

1.2.2.2 Attenuated total reflectance Fourier transform infrared (ATR-FTIR) Spectroscopy

The three common modes of FTIR spectroscopy are transmission, reflection and attenuated total reflectance (ATR) [Griffiths and De Haseth, 2007]. Transmission mode is where the entire beam passes through the sample to reach the detector. Reflection mode can be sub-grouped into transflectance, specular reflectance and diffuse reflectance. Transflectance requires the sample to be placed on an IR reflective substrate such as gold and the beam passes through the sample and reflects the substrate back through the sample to the detector. Specular and diffuse reflectance gather the IR radiation reflected from the surface of the sample; specular reflectance is when the surface of the sample is smooth and the reflected waves are coherent whereas with diffuse reflectance the beam is scattered by the rough surface of the sample. Unlike the other two modes, transmission and

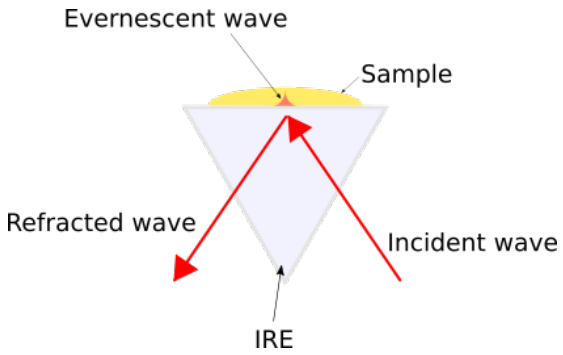

Figure 1.6: Schematic showing the beam path through the internal reflection element and the resulting evanescent wave through the sample.

reflectance, in ATR the beam partially passes through the sample (Figure 1.6). In

this case the IRE crystal, which has a high refractive index composed of diamond, diamond zinc selenide (DiZnSe) or germainum, allows the beam to undergo total internal reflection at the sample contact surface of the crystal (N_s). To achieve total reflectance the angle of incidence has to be greater than the critical angle (θ_c), given by Snell's law,

$$\theta_c = \sin^{-1}\left(\frac{n_2}{n_1}\right), \tag{1.8}$$

where n_1 is the refractive index of the IRE and n_2 is the refractive index of the sample. At the point of reflectance the electric field of the photons extend into the sample, referred to as the evanescent wave. The electric field strength decays with depth and the penetration depth (the depth at which the electric field strength has been reduced by a factor $1/e$) measures the amount of the sample that is interrogated. The penetration depth is dependent on the wavelength of the incident beam, the refractive index of the IRE, the refractive index of the sample and the angle of incidence. As there is a direct relationship between the wavelength and the penetration depth, high wavenumber intensities of a ATR spectra are smaller than at the low end, and ATR correction is needed to compensate for this. In another type of IRE the beam undergoes multiple bounces (Figure 1.7). This is beneficial as there is a superposition of the absorbance signal from the multiple bounces while the background signal strength decays.

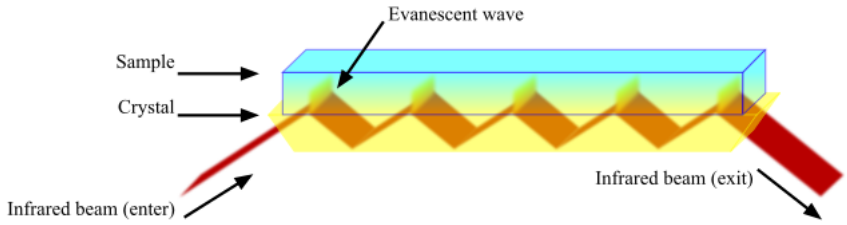

Figure 1.7: Schematic showing Multi-bounce IRE. Reproduced from Fulvio314 [2013].

The main sample requirements for ATR is that the sample has to make contact with the IRE. One problem with biological samples is the presence of water,

which has a strong dipole with vibrations at 3400 cm^{-1} and 1640 cm^{-1}. Therefore, samples are usually required to be dry (Figure 1.8), which can be easily achieved when liquid samples are dried directly on the crystal. However, since ATR probes only the near surface in contact with the crystal, at a penetration depth between 0.2 µm and 5 µm [Kazarian and Chan, 2013], there maybe problems for heterogeneous samples which do not dry uniformly, i.e. the coffee ring effect as described in Lovergne et al. [2015].

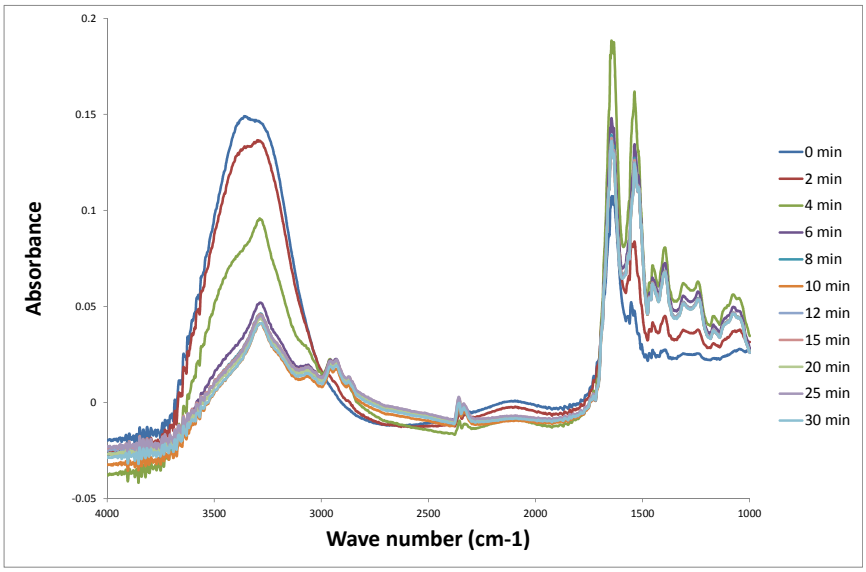

Figure 1.8: Drying pooled serum on ATR crystal and taking spectra at fixed time intervals; 0,2,4,8,10,12,15,20,25 and 30 minutes.

The common detectors stated earlier (Section 1.2.2.2) only produced a single spectrum over the entire crystal but there are alternatives that can spatially resolve the spectra over the crystal; linear arrays (LAs) and focal plane arrays (FPAs) [Kazarian and Chan, 2013]. LAs are a series of pixels in a straight line either orientated horizontally or vertically. The variation of the sample composition along the axis can then be observed. FPAs are a two dimensional matrix

of elements, which allows the resolving of two dimensional features. ATR-FTIR imaging can be used with (Micro) or without (Macro) microscope optics. Micro ATR-FTIR imaging allows for finer spatial resolution and would be required for single cell studies whereas the Macro has been used for tissue studies [Kazarian and Chan, 2013].

1.3 Thesis outline

In anticipation of a potential adoption of ATR-FTIR spectroscopy for diagnostics, in order for the technology to be used as POC tool for remote locations and in crisis deployment, a suitable method of sample preparation has to be developed. This work aims to provide a foundation for the development of a blood preparation device that produces serum, infected RBCs, WBCs and CTCs, for this particular application. The next chapter, Chapter 2, introduces microfluidic methods for particle separation, which can be used for fractionating a blood sample into relevant outputs, and also discusses methods for mixing reagents, which is required for producing serum, and manufacturing techniques are discussed as it useful to understand as part of the design process. The chapter finally presents the design consideration and a potential design concept. Chapter 3 investigates sample requirements of serum for ATR-FTIR spectroscopy. Chapter 4 presents a potential numerical model for developing the first stage of the concept design, which aims to separate diagnostically relevant material from healthy RBCs in blood. Finally chapter 5 summarises the progress and propose future steps.

1.4 References

Alam, M. K., Timlin, J. A., Martin, L. E., Williams, D., Lyons, C. R., Garrison, K. and Hjelle, B. [2004], 'Spectroscopic evaluation of living murine macrophage

cells before and after activation using attenuated total reflectance infrared spectroscopy', *Vibrational spectroscopy* **34**(1), 3–11.

Anderson, N. L. and Anderson, N. G. [2002], 'The human plasma proteome: history, character, and diagnostic prospects', *Molecular & cellular proteomics* **1**(11), 845–867.

Anonymous [2016], 'Research and markets offers fluorescent in situ hybridization probe market analysis', *Professional Services Close - Up* . Copyright - Copyright 2016 Close-Up Media, Inc. All Rights Reserved; Last updated - 2016-04-12.
URL: *https://search.proquest.com/docview/1780096745?accountid=14116*

Anonymous [2017], 'Global enzyme-linked immunosorbent assay (elisa) testing market will reach usd 547.60 million by 2022: Zion market research: According to the report, global enzyme-linked immunosorbent assay (elisa) testing market was valued at approximately usd 437.6 million in 2016 and is expected to generate revenue of around usd 547.6 million by end of 2022, growing at a cagr of around 4.6% between 2017 and 2022'. Copyright - Copyright NASDAQ OMX Corporate Solutions, Inc. Aug 1, 2017; Last updated - 2017-08-01.
URL: *https://search.proquest.com/docview/1924732886?accountid=14116*

Bagula, A., Mandava, M. and Bagula, H. [2018], 'A framework for healthcare support in the rural and low income areas of the developing world', *Journal of Network and Computer Applications* **120**, 17–29.

Baker, M. J., Hussain, S. R., Lovergne, L., Untereiner, V., Hughes, C., Lukaszewski, R. A., Thiéfin, G. and Sockalingum, G. D. [2016], 'Developing and understanding biofluid vibrational spectroscopy: a critical review', *Chemical Society Reviews* **45**(7), 1803–1818.

Barth, A. [2007], 'Infrared spectroscopy of proteins', *Biochimica et Biophysica Acta (BBA)-Bioenergetics* **1767**(9), 1073–1101.

Bromfield, S. M., Wilde, E. and Smith, D. K. [2013], 'Heparin sensing and binding–taking supramolecular chemistry towards clinical applications', *Chemical Society Reviews* **42**(23), 9184–9195.

Clark, S. C. and Kamen, R. [1987], 'The human hematopoietic colony-stimulating factors', *Science* **236**(4806), 1229–1237.

Coates, J. [2006], 'Interpretation of infrared spectra, a practical approach', *Encyclopedia of analytical chemistry: applications, theory and instrumentation* .

D, J. [2007], 'Coagulation full'.
URL: *https://commons.wikimedia.org/w/index.php?curid=1983833*

Dasgupta, A. and Wahed, A. [2014], Liver Diseases and Liver Function Tests, *in* 'Clinical chemistry, immunology and laboratory quality control: a comprehensive review for board preparation, certification and clinical practice', Elsevier, chapter 10, pp. 177–195.

Depciuch, J., Sowa-Kućma, M., Nowak, G., Dudek, D., Siwek, M., Styczeń, K. and Parlińska-Wojtan, M. [2016], 'Phospholipid-protein balance in affective disorders: Analysis of human blood serum using raman and ftir spectroscopy. a pilot study', *Journal of pharmaceutical and biomedical analysis* **131**, 287–296.

Erber, W. [2011], 'Investigation and classification of anemia', *Blood and marrow pathology. 2nd ed. Philadelphia: Lipincott, Williams, and Wilkins* p. 105.

Falcone, F. H., Haas, H. and Gibbs, B. F. [2000], 'The human basophil: a new appreciation of its role in immune responses', *Blood, The Journal of the American Society of Hematology* **96**(13), 4028–4038.

Fasano, A. and Sequeira, A. [2017], Blood coagulation, *in* 'Hemomath', Springer, pp. 79–158.

Fulvio314 [2013], 'ATR path-en'.
URL: *https://commons.wikimedia.org/w/index.php?curid=28499710*

Gajjar, K., Trevisan, J., Owens, G., Keating, P. J., Wood, N. J., Stringfellow, H. F., Martin-Hirsch, P. L. and Martin, F. L. [2013], 'Fourier-transform infrared spectroscopy coupled with a classification machine for the analysis of blood plasma or serum: a novel diagnostic approach for ovarian cancer', *Analyst* **138**(14), 3917–3926.

Griffiths, P. R. and De Haseth, J. A. [2007], *Fourier transform infrared spectrometry*, Vol. 171, John Wiley & Sons.

Haggstrom, M. et al. [2014], 'Medical gallery of mikael haggstrom 2014', *WikiJournal of Medicine* **1**(2), 1.

Hands, J. R., Dorling, K. M., Abel, P., Ashton, K. M., Brodbelt, A., Davis, C., Dawson, T., Jenkinson, M. D., Lea, R. W., Walker, C. et al. [2014], 'Attenuated total reflection fourier transform infrared (atr-ftir) spectral discrimination of brain tumour severity from serum samples', *Journal of biophotonics* **7**(3-4), 189–199.

Haynes, R. H. [1960], 'Physical basis of the dependence of blood viscosity on tube radius', *American Journal of Physiology-Legacy Content* **198**(6), 1193–1200.

Kazarian, S. G. and Chan, K. A. [2013], 'Atr-ftir spectroscopic imaging: recent advances and applications to biological systems', *Analyst* **138**(7), 1940–1951.

Khoshmanesh, A., Dixon, M. W., Kenny, S., Tilley, L., McNaughton, D. and Wood, B. R. [2014], 'Detection and quantification of early-stage malaria para-

sites in laboratory infected erythrocytes by attenuated total reflectance infrared spectroscopy and multivariate analysis', *Analytical chemistry* **86**(9), 4379–4386.

Leehan, K. M. [2018], 'The diversity of immunoglobulin'.
URL: *https://immunobites.com/2018/06/24/the-diversity-of-immunoglobulins/*

Lovergne, L., Clemens, G., Untereiner, V., Lukaszweski, R. A., Sockalingum, G. D. and Baker, M. J. [2015], 'Investigating optimum sample preparation for infrared spectroscopic serum diagnostics', *Analytical Methods* **7**(17), 7140–7149.

Mackey, R. H., Mora, S., Bertoni, A. G., Wassel, C. L., Carnethon, M. R., Sibley, C. T. and Goff, D. C. [2015], 'Lipoprotein particles and incident type 2 diabetes in the multi-ethnic study of atherosclerosis', *Diabetes care* **38**(4), 628–636.

Martini, F. H., Nath, J. L. and Bartholomew, E. F. [2015], Blood, *in* 'Fundamentals of anatomy & physiology', 10th edn, Pearson Education Limited, UK, chapter 19, pp. 678–709.

Maunsell-Browne, Z. [2019], 'Gp sample storage best practice - biochem/haem - version: 1.1', `https://www.ouh.nhs.uk/biochemistry/tests/documents/transport-and-storage.pdf`. accessed 23/10/20.

Minnes, R., Nissinmann, M., Maizels, Y., Gerlitz, G., Katzir, A. and Raichlin, Y. [2017], 'Using attenuated total reflection–fourier transform infra-red (atr-ftir) spectroscopy to distinguish between melanoma cells with a different metastatic potential', *Scientific reports* **7**(1), 1–7.

Monroe, D. M. and Hoffman, M. [2014], 'Theories of blood coagulation: basic concepts and recent updates', *Hemostasis and Thrombosis* p. 1.

Munker, R. [2007], Basic biology of hemopoiesis, *in* 'Modern Hematology', Springer, pp. 1–18.

Naicker, S., Plange-Rhule, J., Tutt, R. C. and Eastwood, J. B. [2009], 'Shortage of healthcare workers in developing countries–africa', *Ethnicity & disease* **19**(1), 60.

Öğrüç Ildız, G., Arslan, M., Ünsalan, O., Araujo-Andrade, C., Kurt, E., Karatepe, H. T., Yılmaz, A., Bölükbaşı Yalçınkaya, O. and Herken, H. [2016], 'Ft-ir spectroscopy and multivariate analysis as an auxiliary tool for diagnosis of mental disorders: Bipolar and schizophrenia cases'.

Owens, G. L., Gajjar, K., Trevisan, J., Fogarty, S. W., Taylor, S. E., Da Gama-Rose, B., Martin-Hirsch, P. L. and Martin, F. L. [2014], 'Vibrational biospectroscopy coupled with multivariate analysis extracts potentially diagnostic features in blood plasma/serum of ovarian cancer patients', *Journal of biophotonics* **7**(3-4), 200–209.

Parham, P. [2005], *The immune system*, Garland Science.

Patel, S., Wetie, A. G. N., Darie, C. C. and Clarkson, B. D. [2014], Cancer secretomes and their place in supplementing other hallmarks of cancer, *in* 'Advancements of Mass Spectrometry in Biomedical Research', Springer, pp. 409–442.

Perry, L. and Malkin, R. [2011], 'Effectiveness of medical equipment donations to improve health systems: how much medical equipment is broken in the developing world?', *Medical & biological engineering & computing* **49**(7), 719–722.

Sabbatini, S., Conti, C., Orilisi, G. and Giorgini, E. [2017], 'Infrared spectroscopy as a new tool for studying single living cells: is there a niche?', *Biomedical Spectroscopy and Imaging* **6**(3-4), 85–99.

Santos, M. C., Nascimento, Y. M., Araújo, J. M. and Lima, K. M. [2017], 'Atr-ftir spectroscopy coupled with multivariate analysis techniques for the identifica-

tion of denv-3 in different concentrations in blood and serum: a new approach', *RSC advances* **7**(41), 25640–25649.

Sitole, L., Steffens, F., Krüger, T. P. and Meyer, D. [2014], 'Mid-atr-ftir spectroscopic profiling of hiv/aids sera for novel systems diagnostics in global health', *Omics: a journal of integrative biology* **18**(8), 513–523.

Zhang, X., Thiéfin, G., Gobinet, C., Untereiner, V., Taleb, I., Bernard-Chabert, B., Heurgué, A., Truntzer, C., Ducoroy, P., Hillon, P. et al. [2013], 'Profiling serologic biomarkers in cirrhotic patients via high-throughput fourier transform infrared spectroscopy: toward a new diagnostic tool of hepatocellular carcinoma', *Translational Research* **162**(5), 279–286.

Chapter 2: Design of a Microfluidic Device

2.1 Introduction

In this chapter we explore the making of a portable blood preparation device using microfluidics that could process whole blood to produce serum, infected red blood cells (RBCs), white blood cells (WBCs) and circulating tumour cells (CTCs). Microfluidics is the study and development of devices that can manipulate small amount of fluids (10^{-18} - 10^{-9} litres) in channels with dimensions of the order tens to hundreds of microns [Whitesides, 2006]. Microfluidic devices that combine small scale fluidics with a detection method to allow for automatic processing of a sample to a result, are referred to as micro total analysis systems (μTAS). These systems are often the most advanced and easiest for an operator to use, due to only needing to add the sample and start the machine. The main difference between the proposed problem and μTAS devices is that the proposed device would be a stand-alone sample preparation device that produces samples that would then be transferred manually to an ATR-FTIR spectrometer. The benefit of using microfluidics for preparing samples is the use of small sample volumes and fast processing [Whitesides, 2006]. The miniaturisation of the preparation process allows for the possibility of creating a low-cost automated portable device that can be used in remote locations and in emergency deployments.

Blood, as explained in chapter 1, is a complex mixture of biomarkers that can be used for diagnosis. Diseases cause effects in specific blood components; for example malaria infects RBCs changing its mechanical properties [Kang et al., 2016]; infections cause an increased presence of WBCs and an increase in protein content of plasma; captured CTCs can be used to identify the type of cancer and

drug susceptibility. Therefore, analysing the separate components of blood allows for better diagnosis of patients.

An early step in the design process, for developing this microfluidic device, is to understand the main components required; flow generation, separation of particles, mixing methods of fluid and the manufacturing process, which will be discussed in the following sections. It is important to know how flow is generated as it limits the type of flow fields that can be generated and determines the type of pump needed. There are variety of separation techniques that can be used with key potential methods presented in this chapter. Every separation method has limitations and therefore combining them requires careful consideration to achieve the desired outputs. To form serum, coagulation has to be initiated which would requires the mixing of a coagulating agent to the sample. Unfortunately, flow in microfluidics is usually laminar, where mixing only occurs via diffusion, which is an issue as diffusion is very slow; however there are a variety of mixing methods that speeds up the process, making it possible to mix fluids in a microfluidic device. Designing the product with manufacturing in mind, minimises the risk of the final design not being able to be produced on a commercial scale [Kipling et al., 2015]. Failure to do so would most likely result in needing a major re-design in order to manufacture the device, which would lead to an increase in development time and cost. This unplanned extra cost may lead to the project being uneconomical, negating the products sustainability. In this chapter we will introduce the main components mentioned earlier and finally, we will present an initial design that could fractionate blood components for easier analysis using ATR-FTIR spectroscopy.

2.2 Controlling flow and Separation methods

The main challenges, in determining the best process for separating the blood components, are to decide on the method of generating flow and which separation techniques to use. These two challenges are interconnected as certain flow generation methods restrict the selection of separation technique that could be used, and specific combinations of different separation techniques may not be functional. Therefore, in this section we will briefly mention the methods of generating flow and review the main methods for separating blood components so that only viable combinations of techniques for this specific application are taken forward in the design process.

Flow generation can be separated into three categories; passive, hand powered and active. Passive generations includes gravity, capillary action and the use of a vacuum. The limitation of passive techniques is the lack of control: therefore only simple flows can be generated. Flows that have been generated by hand using syringes or balloons [Thurgood et al., 2018], micropumps [Laser and Santiago, 2004] and rotating discs Bhamla et al. [2017], tend to have inherent variation in the flow characteristics due to variation in the user input and should not be used when precise flow rates are required for a device to function. Active methods such as syringe pumps and lab-on-a-disc (LOAD) require an external power source and for portability this is usually in the form of rechargeable batteries. However, batteries provide extra weight and are an additional point of failure in the device. A more detailed review of the different methods and the power sources that could be used for self-contained microfluidic systems is provided by Boyd-Moss et al. [2016].

The second challenge is to determine the separation method, which can be categorised into passive and active separation methods. Passive methods use the geometry of the channel and/or structures in the channel to manipulate fluid flow

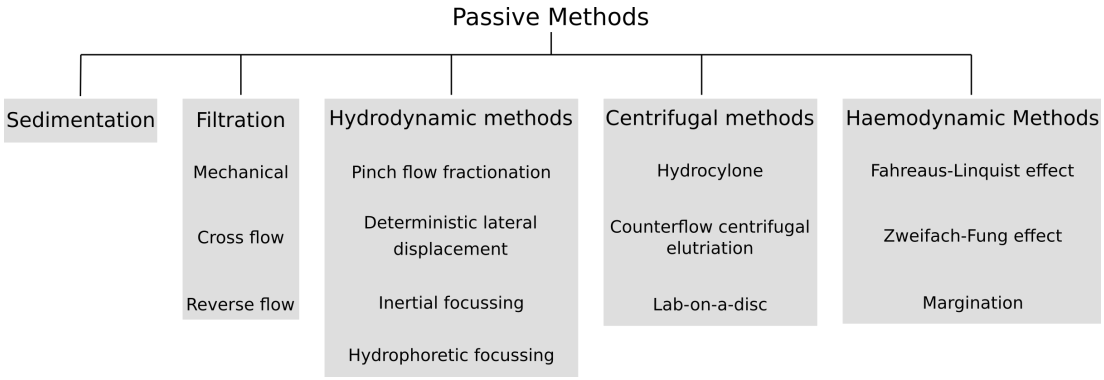

(a) Passive Methods

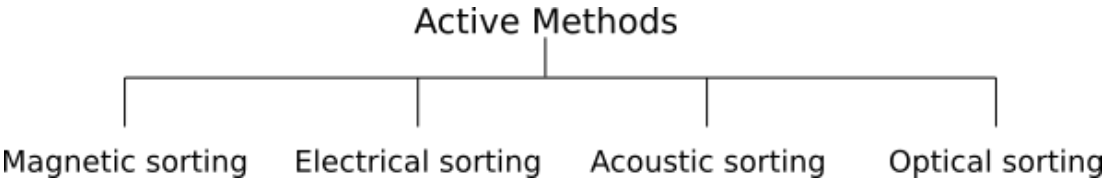

(b) Active methods

Figure 2.1: Particle separation methods in Microfluidics

to sort cells based on differences in mechanical properties (Figure 2.1a). Active devices uses an external applied force (magnetic, electrical, accoustic or optical) in addition to the flow to cause particle migration (Figure 2.1b). These forces can be triggered or their effect augmented by attaching ligands to the target particles. Many of the devices that will be introduced in Section 2.4.2 use a combination of methods to achieve the desired separation. An additional concern is the method of mixing the sample with the reagents, if needed.

2.2.1 Passive Methods

These methods rely on the fact that there are differences in mechanical properties between the different components of blood. The methods presented below include sedimentation, filtration, hydrodynamic interactions, centrifugal and haemodynamic effects.

2.2.1.1 Sedimentation

Blood is a suspension and when left, the cells will sink, under gravity, to the bottom resulting in a cell free region on top known as the supernatant. This process can be used in sedimentation separation in microfluidics devices for the collection of plasma in simple point-of-care (POC) assays [Liu et al., 2013]. In fact particles of different sizes can be separated with this method since they have different terminal velocities in a gravitational field, as determined by the Stokes' drag and buoyancy forces which scale with diameter and volume respectively [Martel and Toner, 2014]. However, this method is relatively slow compared to other methods and a high flow rate will introduce inertial effects and prevent the RBCs aggregating, as discussed later in this section. Therefore, in order for this method to have a high throughput the scale of the device would have to be large or multiplexed.

2.2.1.2 Filtration

Filtration is a simple method for separating particle using physical barriers. There are three categories of filtration techniques: mechanical, cross flow and reverse flow. Mechanical filtration is where the filter is perpendicular to the flow and the common types are membranes, sheets of material with machined pores sandwiched between two channels; microweirs, obstacles in the flow that reduces the height of the channel; and microposts, an array of obstacles where particles are forced between the posts and either get trapped or pass through (Figure 2.2a). The filter pore size determines the size of particle that can pass through. However, larger particles tend to clog the filter causing a saturation of the filter thus reducing the efficiency [Zhang et al., 2012]. Additionally, at high flow speeds cells risk being damaged due to high shear when squeezing through the filter. One way of avoiding the clogging is to use cross-flow filters (Figure 2.2b), where the flow

in the main channel is not perpendicular to the filter and the filtrate is collected in a side channel. For this technique buffer solution is used to direct the sample into the filter while carrying the larger particle away to prevent saturation of the filter. This method allows for the separation of cells based on size, with sized groups being taken for further processing. The angle of the filter to the flow direction has a significant effect on efficiency, with fully cross-flow filters being able to operate at higher flow rates due to less clogging [Catarino et al., 2019; Faustino et al., 2018].There is a range of parameters that may need to be optimised for an application; depth of the main channel and side channels, filter pore size and flow rates. The final form of filtration is reverse flow filtration (Figure 2.2c), where the flow is intermittently reversed to dislodge the larger cells that become trapped on a membrane, thus improving the lifetime of the filter. An implementation of this method uses ratchet pillar (Figure 2.2c), which have been designed to gently allow small deformable cells to pass, while big cells are too stiff and get trapped. Reversing the flow dislodges the large cells while maintaining the small cells on the other side of the filter.

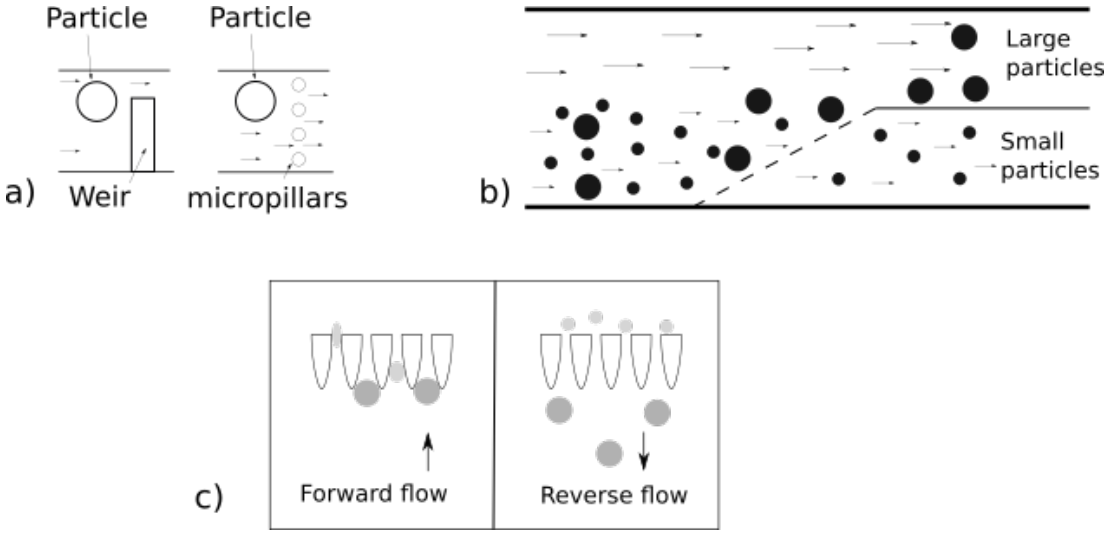

Figure 2.2: Schematics showing some types of microfluidic filters (a) mechanical filters, (b) principles of cross-flow filters (c) reverse flow filtration using ratchet pillars (adapted from Yu et al. [2014]).

2.2.1.3 Hydrodynamic interaction

Hydrodynamic methods of particle separation involves the use and control of the flow field. The standard forms of this technique, namely pinch flow fractionation (PFF), deterministic lateral displacement (DLD), inertial focusing (IF) and hydrophoretic focusing (HF), will be covered in this section.

PFF uses the property that particles travel along streamlines in laminar flow, the sample fluid containing particles can be focused using a buffer fluid [Sajeesh and Sen, 2014]. In the pinch section the particle alignment to the wall is controlled by the flow rates of the two fluids, the sample and buffer. The small particles' centre of mass (CoM) remain close to the wall whereas the large particles are forced into the centre of the channel. After the pinch section the streamlines are separated and thus the particles travel to different outlets (Figure 2.3). The main conditions that need to be adhered to is that the flow is laminar, so that particles do not cross streamlines, and the solution has to be dilute so that the presence of the particles does not disturb the flow. The range of particle sizes that can be separated is determined by the relative flow rates of the inlet solutions and the size of the pinch section. Higher relative flow rate of the buffer compared to the particle flow results in particle flow being compressed in the pinch section leading to smaller particles being transferred to the buffer flow. Narrower pinch section will be more efficient, as flow rates can be slower for the same effect, but larger particles may block the pinch section. Another point of control is the flow rate at the outlets. For instance, asymmetric PFF has one outlet that is shorter with lower resistance, and results in better separation of similar sized particles as particles distributed to all outlets. Other effects can be added to PFF, sedimentation can sort by size and density. If a curved outlet is used then inertial forces can act perpendicular to the flow and particles of similar sizes can be separated based on density. In addition, PFF devices can be tuneable by having valves connected to

the outputs, the resistance of which can be individually controlled, changing the flow field and therefore the outlet location of different particles. Another method of separating particles using the laminar flow principles of PFF is hydrodynamic filtration. Here the particles flow in a main channel, with branches accepting small amounts of flow, which collect the small cells that are close to the wall. The larger cells are in the centre of the channel and after each branch they are brought closer to the wall until they too are taken up by a branch channel. A limitation of PFF and hydrodynamic filtration is the low throughput which is a result of requiring low flow rates and dilute solutions. Using larger channels would improve throughput and reduce the risk of clogging.

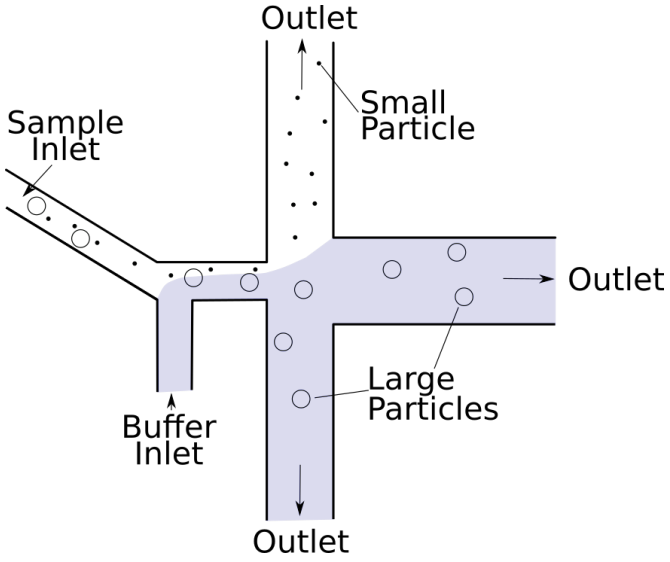

Figure 2.3: Schematic of simple PFF system, sample containing two different sized particles where the grey buffer fluid that transports the large particles to a different outlets that does not contain small particles

The next technique, DLD, also requires laminar flow conditions and can be thought of as a series of micropost filters where the subsequent row is laterally offset as shown in Figure 2.4 [McGrath et al., 2014]. The number of streamlines between two posts is equivalent to the period of the array (N_a), with wider streamlines near the microposts due to the non-slip boundary layer. When cells

flow past the microposts, if the CoM of the particles remain in the streamline, they flow round the post and through the array in a zig-zag mode. However, for larger particles, the inertia causes the CoM to get laterally displaced into the next streamline and they travel in displacement mode [Inglis et al., 2006]. The mode of travel for particles is therefore determined by the critical diameter (D_C); particles whose CoM is positioned less than D_C when flowing around a post travel in zig-zag mode and the rest in displacement mode. Pariset et al. [2017] explains the presence of an intermediary mode between zig-zag and displacement modes. This mode occurs due to assymetric flow caused by the number of microposts along the width of the channel being less than a critical value. Instead of a single D_C, particles below D_{C1} are always in zig-zag mode, particles above D_{C2} are in displacement mode and particles that fall between the limits are in the intermediate mode. Vernekar et al. [2017] found that non-circular post shape and unequal gap distance between the lateral and axial posts also leads to an anisotropic array, which gives the possibility of using a single array of separating multiple particles [Pariset et al., 2017]. Like filtration, DLD has a problem with particles clogging the array. This changes the flow field in the array and reduces the separation efficiency with time. Vernekar and Krüger [2015] also show, via numerical solution, the failure of DLD due to the presence of particle to particle interactions and the alteration of the flow pattern caused by increased particle concentration. However, improving the design of the posts can help reduce this, ie. Hyun et al. [2017] showed that their post design maintained over 90% efficiency after 30 minutes whereas the standard circular pillars were reduced to 77%. Throughput of DLD devices is also limited and Dincau et al. [2018] looked at increasing throughput by increasing the Reynolds number (Re), but it increased inertial forces by creating microvortices in the wake of the posts resulted in reduced effective D_C. One key thing to note is that as the Re increases, the separation efficiency is highly dependent on the micrometer resolution [Dincau et al., 2018], meaning

that higher *Re* operating DLD devices will be harder to manufacture.

Separating particles of similar sizes can be achieved by using multiple arrays in series but to prevent clogging the largest particle cannot be greater than the smallest gap distance. This could be avoided by designing cascade arrays with separate outflows, which will collect the large particles and prevent them reaching the smaller arrays. The resistance of the outflows have to be set to prevent alteration in the flow, which may result in asymmetric flow as mentioned earlier [McGrath et al., 2014].

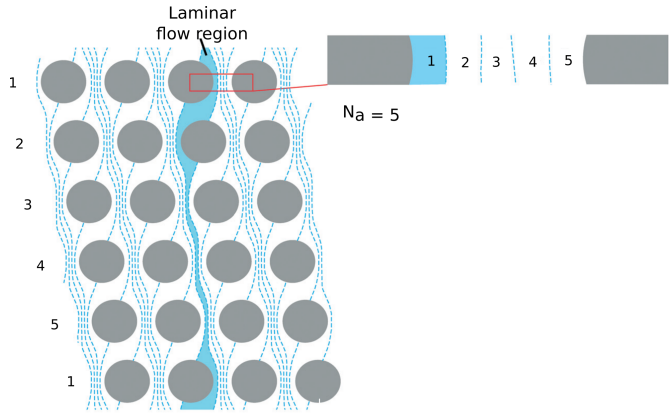

Figure 2.4: Schematic showing DLD array, with the number of streamlines between the post equivalent to the period of the array (adapted from McGrath et al. [2014]).

inertial focusing (IF) is the particle migration caused by the presence of a velocity gradient across the particle, perpendicular to the direction of the flow. The two dominant forces in IF are the wall induced lift force, which moves particles away from the wall and the shear gradient induced force, which drives particles from the centre of the channel, with a weaker inertial lift force due to the difference between the particle and fluid velocities and whether the particle has rotation. This force becomes significant when combined with an additional external force, such as electrical, gravitational or magnetic [Amini et al., 2014]. The balance of the three inertial lift forces determines the location of the particle

in the channel. For instance, particles can be seen in four locations in square micro microchannels but only in two in rectangular microchannels (Figure 2.5a). To explain the positioning of particles, Zhou and Papautsky [2013] proposed a two stage migration process, where first the particles reach the wall due to the balance between shear gradient and wall induced forces and then a slower rotation induced lift force drives the particles to the centre line. Numerical simulations have supported this explanation by showing that the stability of the particle at the centres of the two smaller faces are saddle points [Liu et al., 2015]. Increasing the Re increases the number of stable equilibrium positions in both square (to 8) and rectangular (to 4) with the particles closer to the walls [Chun and Ladd, 2006](Figure 2.5b). Kim et al. [2016a] looked at IF in microchannels with non-rectangular cross-sections; half circle and two triangles, with the semi-circle particles focused in two locations and three for the triangles. Kim et al. [2016a] constructed a single channel with a cross-section changing from rectangular to triangular and finally semi-circle, showing that they can reduce the number of focal streams to one, based on particles entering the catchment area of the focal position of the next cross section. In all of theses situations IF is dependent on the particle properties. The particles focus at different lengths based on the particle diameter, where by larger particles focus in a shorter focal length, L_f, than smaller particles, as described by the by equation

$$L_f = \frac{\pi \mu H^2}{\rho U_m a^2 f_L}, \tag{2.1}$$

where μ and ρ is the fluid viscosity and density, H is the channel width in the direction of migration, U_m maximum channel velocity, a is the particle diameter and f_L being the lift force [Di Carlo, 2009]. Therefore, increasing the size of the particle causes the equilibrium point to shift to the centre.

Many biological particles are not spherical, for example bacteria and RBCs,

and undergo rotation about an axis known as Jeffrey orbits [Hur et al., 2011], which can cause secondary flows and mixing. The position of cells within a channel is also affected by their change in shape due to shear force, and the location and number of equilibrium points is influenced by the particle concentration via the length fraction, which is the fraction of the diameter of the particles per channel length. Increasing fraction length increases hydrodynamic particle to particle interaction, resulting in particles being pushed into new streamlines, which reduces the focusing [Kahkeshani et al., 2016]. An alternative to using straight channels is to use curved channels, where there is inherent velocity difference across the channel cross section resulting in fluid recirculation known as Dean's flow [Martel and Toner, 2013]. The two major types of curved channels used are asymmetric sinusoidal channels and spiral channels [Martel and Toner, 2012] (Figure 2.5c). These channels are used as an alternative to straight channels as the length to focussing is much shorter and therefore the footprint of the channel can be smaller [Amini et al., 2014]. The final type of channel that uses IF is the expansion contraction channels (Figure 2.5d), where the wall induced lift force is suddenly removed in the expanded section. Even though large particles are further away from the wall they are affected more by the lift force than smaller particles therefore they migrate into the regions of recirculations present in the expanded section and remain trapped [Che et al., 2016]. IF, unlike previous methods, can operate at relatively high flow rates, meaning high throughput but still requires dilute solutions in order to separate particles efficiently.

HF is a relatively simple system based on the migration of particles caused by presence of slanted obstacles on the bottom and top walls of the channel (Figure 2.6). As the fluid along one side of the wall hits the obstacle first, the cross-sectional area decreases resulting in an increase in the resistance which generates a transverse pressure gradient that sets up helical secondary flow; the flow is forced upwards, focusing, downward, and deviation flows [Choi and Park, 2007].

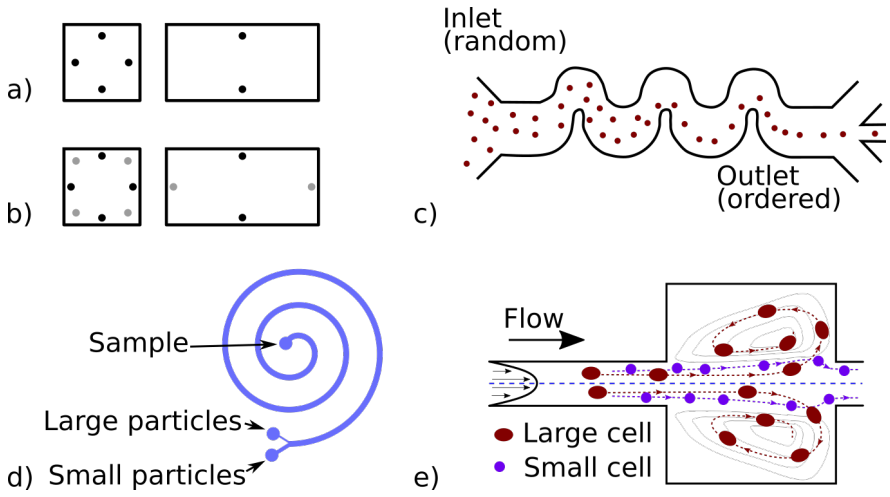

Figure 2.5: Aspects of IF: Schematic showing particle positions in square and rectangular microchannels in (a) low *Re* condition and (b) high *Re*; Schematics for two types of curved channels, (c) asymmetric sinusoidal channel (adapted from Di Carlo et al. [2007]) and (d) an example of a spiral channel; (d) Schematic of contraction-expansion section of channel (adapted from Che et al. [2016]).

The effect of this pressure differences is dependent on the size of the particle with larger particles being deviated more (Figure 2.6).

2.2.1.4 Centrifugal

The next type of passive methods is centrifugal, which involve the rotation of the fluid generating separation. The centrifugal methods based on hydrocyclones, counterflow centrifugal elutriation (CCE) and LOAD are covered in this section. Hydrocylcones separate particles from liquids based on centrifugal force generated by having the inlet flow tangential to a cylindrical chamber (Figure 2.7a) [Bhardwaj et al., 2011]. There are these three forces affecting particles, the centrifugal, drag and buoyancy forces, which result in particles that are denser than the fluid migrating to the periphery then to the bottom outlet, whereas the less dense particles will migrate to the axis of rotation and to the top outlet. This method provides continuous separation and as the dimensions are larger than the particle there is a lower risk of clogging. However, fabrication of these devices on

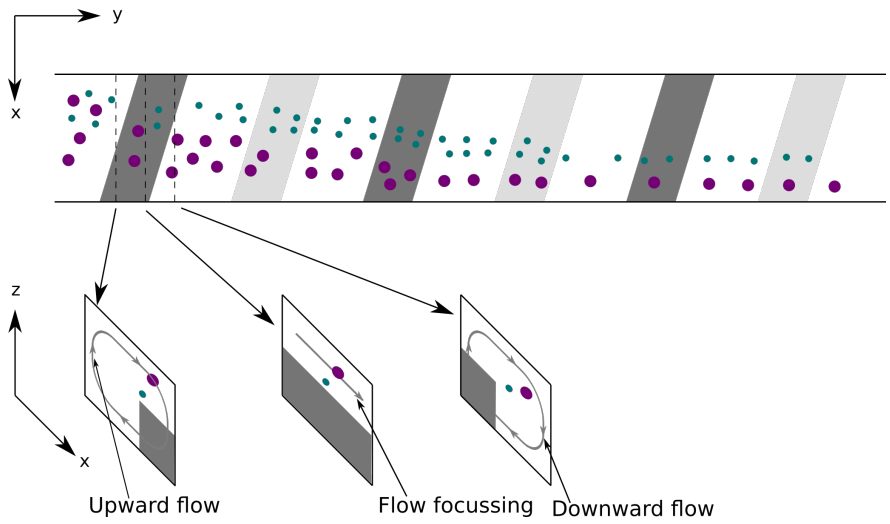

Figure 2.6: Principles of HF in channel with slanted obstacles on the bottom wall (dark grey) and on the top wall (light grey)(adapted from Choi and Park [2007]).

small scale is still challenging. The main limitation is the required density difference between the fluid and particles [Warkiani et al., 2015], which is problematic for biological cells as the density of carrying fluid is usually similar to that of the cells. Therefore, a special carrier fluid would need to be created depending on the cells that need to be collected.

CCE uses a balance of centrifugal and counter flow forces to separate particles based on differential sedimentation properties (Figure 2.7b). Particles enter near the boundary and are subject to centrifugal forces. A buffer is then introduced in the opposite direction to the centrifugal force causing drag. When the drag force is greater than the centrifugal the particles exit the chamber with the smaller particles exiting before larger ones [Warkiani et al., 2015]. Unlike the conventional 3D cone shaped CCE, Morijiri et al. [2013] developed a 2D planar chamber for use in LOAD application. Rotation provides the driving force for the fluid and the particle position is dependent on the particle size, shape and density, with smaller and less dense particles compared to fluid density leaving through the outlet. Increasing the fluid density reduces the centrifugal force on the particle

and therefore larger particles will then start leaving the chamber. This method requires particles to be dilute in order to prevent aggregation and requires storage of the different buffers.

LOAD is a μTAS in the form of a rotating disc. The three forces important in the LOAD application are centrifugal, Euler and Coriolis forces [Ducrée et al., 2007]. As LOAD is a unique system, the special method of controlling the flow will be discussed here. One of the main ways of controlling flows is the surface treatment of the channels; hydrophilic channels attract the sample fluid whereas hydrophobic surface restrict flow. Narrow hydrophilic channels can be used to transport fluid back into the centre of rotation from the edge so that more processing can occur, a process known as capillary priming, and narrow hydrophobic contractions act as valves requiring a burst frequency to be reached in order for the meniscus to pass through. Sacrificial valves retain liquids and ,when externally triggered, the stored liquid is released into the system. Centrifugal platforms are self contained systems and the fluid control is provided by the rotation so there is no need for external connection to a syringe pump which means bubbles are less likely to form and interfere with the flow fields.

2.2.1.5 Haemodynamics effects

The last category of the passive methods is haemodynamics. These methods exploit phenomena that are found in microvasculature; Fåhræus-Lindqvist (FL) effect, Zweifach-Fung (ZF) effect and margination. These methods operate using undiluted blood, unlike previously mentioned passive methods, simplifying the processing and improving cell processing rates [Warkiani et al., 2015]. RBCs under physiological shear gradients found in the microvessels tend to migrate to the axial centre of channel creating the cell-free layer (CFL) (Figure 2.8a), which reduces the wall shear stress and therefore the resistance of the channel and is known as the FL effect [Fahraeus and Lindqvist, 1931]. In microcirculation there

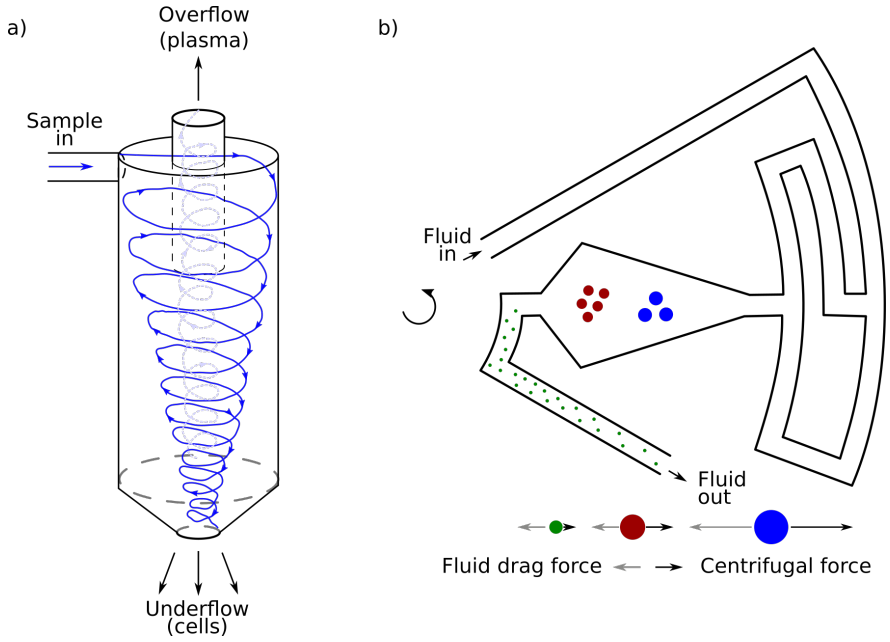

Figure 2.7: Centrifugal methods: (a) Schematic showing the fluid flow directions inside a Hydrocyclone (adapted from Bhardwaj et al. [2011]) and (b)Schematic showing particle separation using a CCE, large particles (blue) and medium particles (red) remains inside while the lighter particles (green) are flow out of device (adapted from Morijiri et al. [2013]).

are lot of branching vessels and it was noticed that the cells tend to travel in the branch with the higher flow rate, this is known as ZF effect (Figure 2.8b). These two effects can be used to separate plasma from whole blood without the need for dilution. Due to the way RBCs can conform to the flow due to their flexibility, cells that are stiffer such as the infected RBCs, WBCs and CTCs, are forced to the channel walls, a process known as margination [Hou et al., 2016], where these cells can be skimmed off (Figure 2.8c).

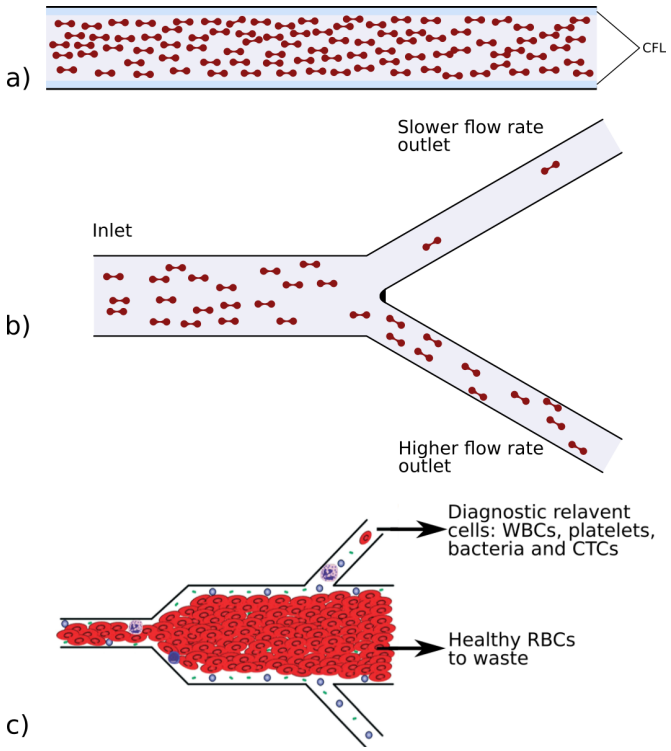

Figure 2.8: Haemodynamic phenomenons; (a) Schematic explaining the FL effect, (b) the ZF effect and (c) margination (adapted from Hou et al. [2016]).

2.2.2 Active methods

Active methods, as stated earlier, use the addition of an external force on top of the effect of the flow. We will start by introducing affinity ligands which can augment many of the other techniques, magnetic, electrical or acoustic sorting,

with optical sorting being discussed last.

2.2.2.1 Affinity ligands

Biological cells have a complex cell membrane with a variety of molecules available for affinity based techniques. Three types of affinity ligands, antibodies, aptamers and peptides, can be designed to target specific cell types allowing for their detection and/or localisation [Zhang et al., 2018a]. Antibodies have been a long standing option in targeting cells and come in two forms: polyclonal, which detects multiple epitopes on the target cell, and monoclonal, which targets only one but offers higher specificity. The tail end on the antibody can be attached to a response enzyme, for detection, or bound to channel walls, for localisation. Aptamers are single stranded oligoneucleotides folded into secondary or teriary structures that uniquely bind molecules on the target cell membrane [Chang et al., 2013]. Chen et al. [2017] has shown the effectiveness of using aptamer coated microposts in capture of CTCs. Aptamers have high affnity and specificity that are comparable with antibodies [Chang et al., 2013; Zhang et al., 2017]. Peptides can identify specific cell markers via phage, mRNA or ribosomes and is an option as they are small, stable and easy to synthesise. The main limitation is that their selectivity is low due to the reversible, weak interaction between the peptide and its epitope. A common use of ligands in cell separation is fluorescent activated cell sorting (FACS), where by ligands labelled with fluorophores binds to the target cell. When the cell is illuminated by a laser, the fluorescence is detected and activates an active sorting method such as magnetic, electric, acoustic or optical, which will be discussed later in this section. The main limitations of affinity based techniques is firstly the additional cost of developing the affinity ligands, the fact that they can still bind incorrect cells and are impractical to use for targeting multiple cell types. Also, the flow of the cells in the channel has to be designed so that there is a high probability of the target cells coming into

contact with the ligand; otherwise rare cells can be missed. The binding of the labels to the cells can also affect the cell viability and function, thereby limiting further analysis options.

2.2.2.2 Magnetic sorting

Magnetic activated cell sorting (MACS), also known as magnetopheresis, is another use for affinity ligands but here the ligands are conjugated with magnetic nanoparticles. The target cell can then be trapped using a magnetic field, while the undesired material can be washed away. Then a clean buffer can be used with the field turned off to collect the cells. MACS is usually used in laminar flow devices where the magnetic force causes a lateral migration of the targeted cells across the streamlines. MACS is cheaper than FACS due to not needing a laser or detector but there are multiple steps in MACS that makes the protocol longer [Yu et al., 2014]. Magnetophoresis without using affinity ligands is limited to separating out paramagnetic cells, such as RBCs, while having no affect on the carrier fluid and other cells. Magnets can be built into the microfluidic chip, causing localised magnetic fields giving more control of the movement of cells of interest due to the small distances involved. The main limitation of magnets is the damage to the sample caused by Joule heating, the heat generated by moving current in a material.

2.2.2.3 Electrical sorting

Electrical sorting, also known as electrophoresis, is similar to magnetopheresis but instead of a magnetic field, a uniform electric field is set up, where particles are attracted to the electrode depending on their charge. For separating cells, dielectrophoresis (DEP) is commonly used where, unlike electrophoresis, there is a non-uniform electric field leading to an induced electric dipole across the cell. This separation of charge then results in the cells being attracted to the electrode.

There are two main modes of DEP; positive dielectrophoresis (pDEP), where cells possessing a higher electrical permeability than the surrounding media move towards regions of strong field intensity, and negative dielectrophoresis (nDEP), which is the reverse and is more common in biological applications. One feature of electrical fields is their ability to be turned on and off using light, by way of photoelectric elements, and allows for complex field patterns and dynamic separation of particles [Chiou et al., 2005]. However, there are concerns that electrophoresis can generate hydrogen and oxygen gases and other undesired chemicals, via electrolysis, which are harmful to mammalian cells, as well as generating elevated temperature due to Joule heating [Yu et al., 2014].

2.2.2.4 Acoustic sorting

Acoustic force sorting, also known as acoustophoresis, can be used without the use of ligands and physical interaction with the cells, and therefore minimises the biochemical damage, while allowing for precise spatial control [Shields IV et al., 2015; Warkiani et al., 2015]. There are three categories of acoustic waves used; bulk accoustic standing waves (BASW), surface standing acoustic waves (SSAW) and travelling waves [Shields IV et al., 2015]. Standing waves are the superposition of two waves that have equal magnitude and frequency but are travelling in opposite directions, which produce important pressure points; nodes are where the pressure is constant and the anti-nodes are where the pressure varies between the maximum and minimum pressure. A more detailed explanation of standing waves can be found in Luo et al. [2018]. BASW uses ultrasonic wavelengths that matches the channel dimensions; the magnitude of the force is then dependent on the volume of the cell and the direction is dependent on the acoustic contrast factor, which depends on the relative compressibility and densities of the fluid and cells. Particles with higher densities than the fluid have a positive contrast factor and will migrate to the node whereas particles with a negative value will migrate

to the anti-node. Therefore, cells can be separated based on size. SSAW are standing waves produced by mechanical disturbances in the floor of the channel caused by interdigital transducers. A special arrangement of the transducer, such as in slanted finger interdigital transducers, allows the acoustic field to be tunable [Sajeesh and Sen, 2014], where the wavelengths between the pairs of fingers are different with different radio frequency input setting the wavelengths. Travelling waves are used to deflect particles or the flow in response to a specific trigger such as FACS. Acoustic microstreaming is another use of acoustic force but is different from the previous methods as it requires an oscillating liquid interface [Garg et al., 2018]. Finally, lateral cavity acoustic transducers are trapped bubbles in cavities that are at an angle to the main channel. Vibration of the interface causes vortices to form and particles of different sizes have different orbits. These transducers can be used to generate flow by way of simultaneous activation of multiple cavities.

2.2.2.5 Optical Sorting

The final active method to be presented is optical sorting, which can be used to manipulate single cells. In this case, light beams generate two pressure forces, a gradient force, which attracts the cell to the most intense part of the beam on the axis perpendicular to the direction of the beam, and the scattering force, which moves particle to the most intense part of the beam in the direction of the beam [Atajanov et al., 2018]. Cells are driven to the centre of the trap by restorative forces to the region of highest intensity with the trap size defined as the size of the area within which the cells experience the maximum restorative force. This optical force is affected by wavelength and the particle size and can be modelled by three approximations: ray optics, Rayleigh scattering and Mie scattering. The ray optics approximation is used for particles much larger than wavelength of light and used for large biological cells. For cells that are smaller

than the wavelength of light, Rayleigh scattering is used and Mie scattering for cells of a similar size to wavelength. Microlens arrays and diffraction optics can be used to create multi-trap arrays. Instead of static elements, it is also possible to create dynamic multi-trap arrays using spatial light modulators (SLM), which are found in two categories of phase modulation, using liquid crystal spatial light modulators (LC-SLM) and amplitude modulation using digital micromirror device (DMD). LC-SLM uses liquid crystal on silicon, metal oxide technology, where the liquid crystal can modulate the polarisation or phase of the light. A DMD is an array of mirrors (optomechanical elements) on a static random access memory chips so that individual mirrors can be accessed independently. In DMD the mirrors can be in two states, on, where the light is guided to the projection lens, and off, when it is not, this means an array of on and off traps can be dynamically controlled. The advantage is that it provides high spatial resolution and therefore high purity. The main restrictions of such a system is that it limited to single cell manipulation, slow flow rates 120 $\mu m\,s^{-1}$and processes 1-5 particle per second. The complexity of the set up, light, light guides and the equipment required for imaging, would also make it impossible to use in POC application when maintenance and portability are necessary considerations.

2.2.3 Mixing

Mixing in microfluidic devices is an issue as flow regimes are usually laminar ($Re < 1$) and therefore mixing only occurs via diffusion [Cai et al., 2017]. This section will introduce the concepts of micromixing and more detailed review can be found in the literature [Cai et al., 2017; Lee et al., 2011; Nguyen and Wu, 2004]. As for separation methods, mixers can also be categorised as passive or active based on the addition of an external energy source in addition to the flow. Active micromixers can be driven by pressure, electric field, sound, magnetic field, thermal field and centrifugal. Pressure-driven refers to the sudden change

of the pressure field, which results in a perturbation of the flow, and occurs via pulsatile flow micropumps or braille pin actuators. The purpose of this system is to increase the contact area between the fluids. Fluids with different flow characteristics form hydrodynamic instabilities which result in turbulence and therefore mixing. Electric fields can be used in electrically charged fluids to cause electrohydrodynamic instabilities. For instance DEP, mentioned in Section 2.2.2.3, can be used to migrate particles from one fluid to another causing mixing [Lee et al., 2011]. During sound-driven mixing, acoustic resonance of bubbles causes disturbances in the flow; although this can increase the fluid temperature [Lee et al., 2011]. Another way to manipulate bubbles is to change their sizes using temperature and therefore, rapidly changing the thermal field using microheaters can also cause perturbations in the flow. Another mixing method is to use surface acoustic waves, as mentioned in Section 2.2.2.4, which allows continuous mixing without disrupting the flow. Magnetic fields are best used for magnetic fluids and for this application an external rotating field can drive magnetic stirrers such as magnetic microbeads, resulting in secondary flow for mixing. The last active method is centrifugal, as mentioned in Section 2.2.1.4, where the Coriolis force can cause transverse flows and leads to mixing.

Passive (also known as static) micromixers are similar the passive separation method, and use the geometry of the channel to control the flow field, for example using 2D or 3D structures. 2D mixers such as obstacle-based, spiral channels, unbalanced collisions and convergence-divergence mixers will be covered. Obstacle-based mixers can be of the form of the groves or barriers used in HF (Section 2.2.1.3), where the secondary flow induced will induce mixing. Separation and recombination (SAR) obstacles are full channel height barriers that separate the flow and force them back together. Obstacles can also be placed in curved channels, reducing the flow rate needed for mixing. Spiral channels used in IF (Section 2.2.1.3) induces Dean's flow which also induces mixing, and

double spirals, where the curvature is reversed in the second half of the channel, improves the mixing. Unbalance collisions occur when the flow is unequally split and forced back together, which can be done using asymmetric channel structures and/or different flow rates. Asymmetric structures can be combined with cavities creating convergent-divergent structures, which generate vortices in the expansion section. These structures can then be coupled with pulsatile flow, sinusoidal walls and include SAR obstacles which can perturb the lamina flow. 3D structures are more complicated to fabricate, with one example being flow lamination, the splitting and redirecting of the fluids so that the two fluids occupy alternate laminar layers in the main channel, which increases contact area between the fluids improving diffusion. Spiral channels can also be made using the third dimension, this allows more complex flows and better mixing. One final method uses overbridge channels which are based on SAR principle but in the third dimension.

In this section, we have covered methods of generating flow, passive and active methods of separating particles, and how to mix fluids at such small scales. All these concepts need to be considered when designing a device as certain methods are incompatible with others.

2.3 Manufacturing

There is a wide variety of possible manufacturing techniques that are applicable for microfluidics fabrication. This section will not present an exhaustive list but good reviews can be found in papers [Catarino et al., 2019; Gale et al., 2018] and books [Kipling et al., 2015]. A summary of these techniques is presented in Table 2.1, and in this section we focus on photolithography, soft lithography and 3D printing technologies. Photolithography combined with soft lithography are common techniques used in research as they provide accuracy of features,

smooth vertical walls, which are suitable for comparing with numerical models, and fabrication of multiple devices is affordable. For these reasons these methods are used later in Chapter 4. 3D printing technologies have been included due to its relative novelty, the ability to rapidly iterate designs and as the market in hardware design is competitive, there is potential for rapid innovation which could be translated into microfluidic device design.

Table 2.1: Summary of Microfluidic manufacturing methods showing advantages and disadvantages

Method	Description	Materials	Advantages	Disadvantages	Ref
Photolithography	Light is used to pattern a substrate via a photosensitive polymer mask. The exposed substrate surface is etched creating the channels.	Glass, Silicon, SU-8	• Established technology for manufacturing at scale	• High set up cost	[Prakash and Yeom, 2014]
Soft lithography	A polymer is cured in a mould and bonded to a surface glass, plastic or epoxy to seal channel	PDMS, Epoxy	• Cheap material • PDMS is biocompatible • High precision • Layers can be stacked to make 3D structures	• Manually intensive • Difficult to mass produce	[Cheng et al., 2017]

Continued on next page

Table 2.1 – *Continued from previous page*

Method	Description	Materials	Advantages	Disadvantages	Ref
Print and Peel	Printing masters using standard office equipment for casting polymers	Toner polymer; polyester, polystyrene and epoxy resin	• Cheap and easily available equipment • Can make mould with different shaped cross section	• Moulds are not durable • Resolution limited by printer • Manually intensive casting step	[Dixon et al., 2017]
Xurography	Using cutting plotter and vinyl films to make moulds, masks and even channels	Vinyl films	• Cheap material and equipment • Rapid fabrication	• Poor resolution • Limited to channel sizes greater than 500 µm • Manually intensive to line up layers	[Speller et al., 2019]

Continued on next page

Table 2.1 – *Continued from previous page*

Method	Description	Materials	Advantages	Disadvantages	Ref
Laser direct plotting	Laser is used to cut channel out of rigid plastic and is laminated with polymer to seal channel	PVC for channels, PET film with thermal sensitive ethylene vinyl acetate co- polymer for adhesive. Can be used for making moulds	• Cheap material • CNC controlled cutting	• Adhesive strength limits the pressure (45kPa) in the channels • Too costly to use femtosecond laser for 3D structured in manufacturing	[Wang et al., 2012; Zhang et al., 2016]
Micromilling	High precision computer numerical controlled drill bit cuts shape in hard plastic	Hard thermoplastics; PMMA, COC	• Direct to device fabrication • Produce 5 µm structures without clean room	• High capital investment on equipment • Tool breakage • Difficult tool alignment	[Guckenberger et al., 2015; Owens and Hart, 2018]

Continued on next page

Table 2.1 – *Continued from previous page*

Method	Description	Materials	Advantages	Disadvantages	Ref
Hot Embossing	Using high temperature and pressure thermoplastic is pressed into a mould made of metal or epoxy	Thermoplastics; COC, PMMA, polycarbonate, PET	• High production rate • Less stress in plastic than injection moulding	• Limited to planar structure	[Jeon et al., 2011]
Fused deposition modelling (FDM)	A motorised nozzle deposits a heated thermoplastic onto a build plate. Plastic is applied layer by layer and cooling binds the plastic together	ABS, PLA, polycarbonate, PET, poly amide and polystyrene	• Multi-material objects • Cheap printers • Simple to use, Wide choice of commercial thermoplastics	• Low resolution • Rough walls • Not possible to have optically clear material • Risk of leaks due to print quality	[Dixit et al., 2018]

Continued on next page

Table 2.1 – *Continued from previous page*

Method	Description	Materials	Advantages	Disadvantages	Ref
Multijet modelling (MJM)	3D printing using inkjet heads delivering a UV curable polymer	Proprietary polymer	• Good for rapid prototyping • Can use multiple materials	• Proprietary material • Sacrificial material used to make complex structures can get trapped in channels	[Bhattacharjee et al., 2016]
Stereolithography (SLA)	Resin in a vat is photopolymerised using a light source. Subsequent layers are photopolymerised onto or underneath the layer depending on configuration forming 3D structure	ABR	• Rapid • Inexpensive equipment and resin • Can get biocompatible resin • Straight to part	• Single material • Some manual processing steps • Resolution less than photolithography	[Dixit et al., 2018]

Continued on next page

Table 2.1 – *Continued from previous page*

Method	Description	Materials	Advantages	Disadvantages	Ref
Injection Moulding	Liquid plastic is injected into a multi part mould and form the finished device	Thermoplastics; COC,	• Cheap part manufacturing • High volume production	• High set up cost • Time needed to fabricate mould therefore not suitable for rapid prototyping	[Attia et al., 2009; Tosello, 2018]

2.3.1 Photolithography

Photolithography is the process of transferring a pattern onto a photosensitive film via exposure to light. It is widely used in the microelectronics and micro-electromechanical systems (MEMS) industry as it is scalable and therefore also used widely in the fabrication of microfluidic devices. The process is summarised in Figure 2.9a. It begins with the fabrication of a photomask; a design is created using computer aided design (CAD) software and printed onto, typically, a glass plate using an emulsion of chromium and iron oxide. A substrate such as silicon is first cleaned to remove dust particles, metal ions and organic residues. The cleaning process is dependent on the substrate and the type of film used [Prakash and Yeom, 2014]. It is then covered in a photoresist polymer (PR) via spin or spray coating and prebaked for the PR to adhere better to the substrate. The photomask is aligned with the wafer and then ultraviolet (UV) light is transmitted through the photomask onto the PR. There are two types of PR, positive and negative. UV exposure on a positive PR results in the exposed area dissolving in the development stage, whereas on a negative PR the exposed surfaces remain intact. Positive PR are generally better for smaller features ($<$0.5 µm) but is more expensive than negative PR [Prakash and Yeom, 2014]. However, positive PR has low adherence to the substrate than negative PR, so is applied on top of the thin film, and then the exposed thin film is etched. For negative PR, a metal such as silver can be deposited on top of the PR. The PR is then removed exposing the underlying substrate, which is then etched and the deposited metal layer is removed. After the channels are etched, the PR/ thin film or metal are removed then the substrate is bonded with glass to seal the device [Le et al., 2017]. This method can be used to mass produce POC devices, as it can be fully automated resulting in low cost when manufactured on a large scale but is not suitable for prototyping due to the process having a high cost as it needs a clean

room; the use of substrates, such as glass and silicon; and trained staff. It takes a long time for staff to go from design to prototype which prevents its use in testing of iterative designs. Photolithography can also be used for creating moulds for soft lithography, which is presented in next section. The exposed PR or thin film acts as the mould representing the channels (Figure 2.9b).

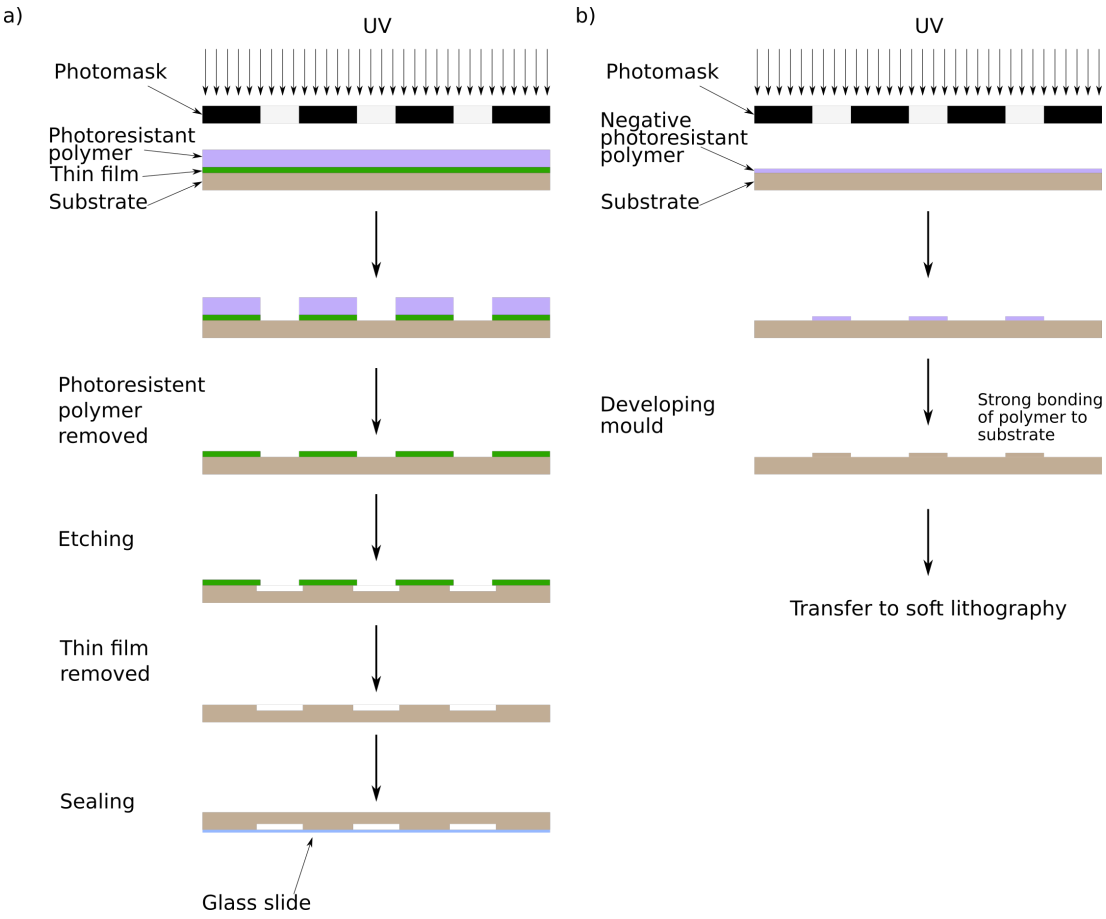

Figure 2.9: Schematic showing the photolithography process for making (a) channels and (b) moulds [Prakash and Yeom, 2014]

2.3.2 Soft lithography

Soft lithography is a popular alternative photolithography technique for microfluidic devices in biomedical applications. Channels are created by curing poly-

dimethylsiloxane (PDMS) on top of a master mould, the steps are shown in Figure 2.10. The master mould is usually made using photolithography and SU-8 a negative PR (Figure 2.9b) but other manufacturing processes shown in Table 2.1 can also be used. The mould is cleaned and two components; a base and a curing agent are mixed and then poured over the master mould (Figure 2.10b). The vinyl groups in base cross-link with the silicon hydride groups found in the curing agent forming an elastomeric solid [McDonald and Whitesides, 2002]. This process is sped up by baking the mould and, once fully cured, the PDMS can be peeled off the mould (Figure 2.10c). The PDMS is then cut and holes for the inlet and outlet are punched (Figure 2.10d). The PDMS can then be bound reversibly or irreversibly with glass or itself [McDonald and Whitesides, 2002]. Reversible binding relies on Van de Waal's forces but is weak and for devices to withstand greater pressures irreversible bonding using oxygen plasma is required (Figure 2.10e). Oxygen plasma activates the surface of the PDMS and the other material allowing them to form covalent bonds (Figure 2.10f). A more advanced form of soft lithography, 3D soft lithography, can be used to make multilayer and 3D structures [Faustino et al., 2016], with grey scale technology allowing the creation of structures of different thickness based on different grey scale values. 3D soft lithography is often needed to make complex 3D parts that contain internal structures such as valves and network of channels. In this method layers are normally aligned manually, and therefore devices have large spaces between feature giving high tolerance to misalignment errors. Kipper et al. [2017] developed an automated device to carry out sealing, which reduces the misalignment error, and therefore allows smaller features to be used. The benefits of soft lithography is that PDMS is cheap, biocompatible and its flexibility allows integration of other components into the devices [McDonald and Whitesides, 2002]. Even though the cost of the mould can be high, the repeated casting of the mould using PDMS to produce many devices making soft lithography suitable technique for producing

devices for repeated testing during research. Unfortunately new designs would need new moulds which comes at a cost and are not quick to produce, thereby limiting it as a tool for an iterative design process. The main limitation for the manufacturing of POC devices is the lack of scalability as fabricating is still a manually intensive process [Walsh III et al., 2017].

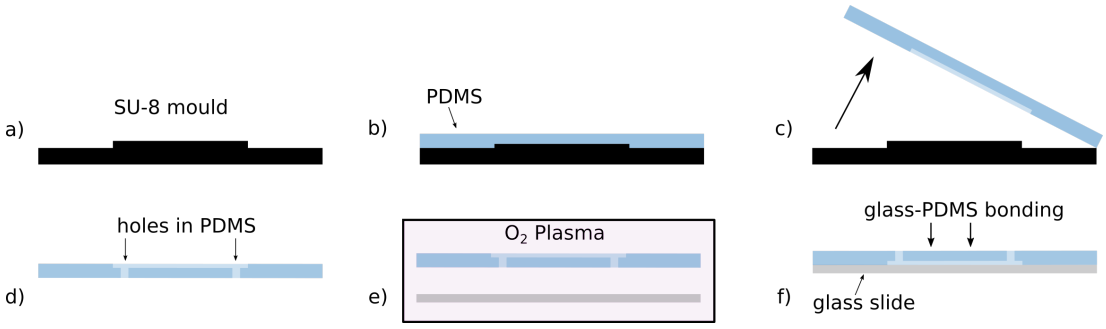

Figure 2.10: Steps of Soft lithography (a) SU-8 mould (b) Curing PDMS on mould, (c) Peeling PDMS from mould, (d) Punching holes into PDMS, (e)oxygen plasma activation of surfaces of PDMS and glass slide, (f) sealing of PDMS with glass slide.

2.3.3 3D printing technologies

3D printers are able to go from CAD drawing straight to prototype allowing for quick iterative designing, unlike soft lithography which uses a mould made by photolithography. The three main types of 3D printing methods for microfluidic channel fabrication are FDM, MJM and SLA and will be discussed below; Weisgrab et al. [2019] and Sochol et al. [2018] provide a more thorough review of 3D printing for microfluidic applications.

2.3.3.1 Fused deposition modelling (FDM)

In FDM (Figure 2.11), a hot thermoplastic filament is extruded through a heated nozzle, cools onto a plate and then the next layer is printed on top. Fusion between the layers is due to cooling and hardening of the polymer, which is not

structurally strong and not properly sealed. The polymers used, acrylonitrile butadiene styrene / minimum absorbance value (ABS), poly-lactic acid (PLA), poly-carbonate, polyethelene terephthalate (PET) polyamide and polystyrene are cheap and bio-compatible [Bhattacharjee et al., 2016] but the size of filament extruded (0.2-0.5 mm) is larger than typical channel size [Bishop et al., 2016]. FDM can be used to make a 3D microfluidic mould with sacrificial material that gets dissolved after bulk material is cured. For example ABS can be dissolved by acetone after printing, although this would be a slow process in small channels as it is limited by diffusion. Channels made this way have circular cross sections and orthogonal junctions which make observation using a microscope difficult. FDM made channels need to improve in terms of transparency, leaking and pressure, for FDM to be viable for fabrication [Morgan et al., 2016].

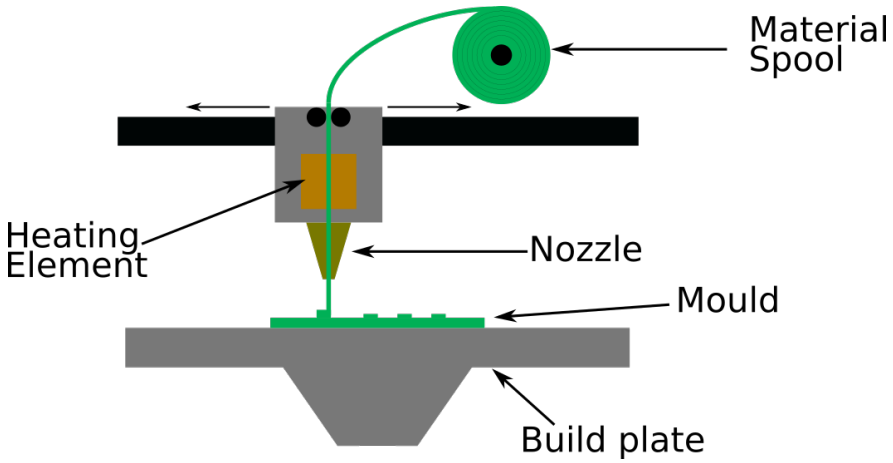

Figure 2.11: Schematic showing FDM printing technique in two dimensions; a filament is heated and extruded through the nozzle and cools onto the build plate. Either the nozzle moves up or the build plate moves down to make next layer depending on the model of 3D printer used.

2.3.3.2 Multijet modelling (MJM)

MJM prints a photopolymer via injection heads onto a tray and is rapidly cured using UV light [Bhattacharjee et al., 2016]. When overhanging structures are

needed a gel like sacrificial material is applied for support and then dissolved after the build is complete. MJM can deliver multiple materials to build an object with multiple material properties, but the main limitations are that materials are proprietary and biocompatability has not been assessed. MJM has high resolution and allows multiple printing material, but the fact that sacrificial material needs to be reliably removed from the enclosed channel is a limiting factor, and which like FDM is limited by diffusion.

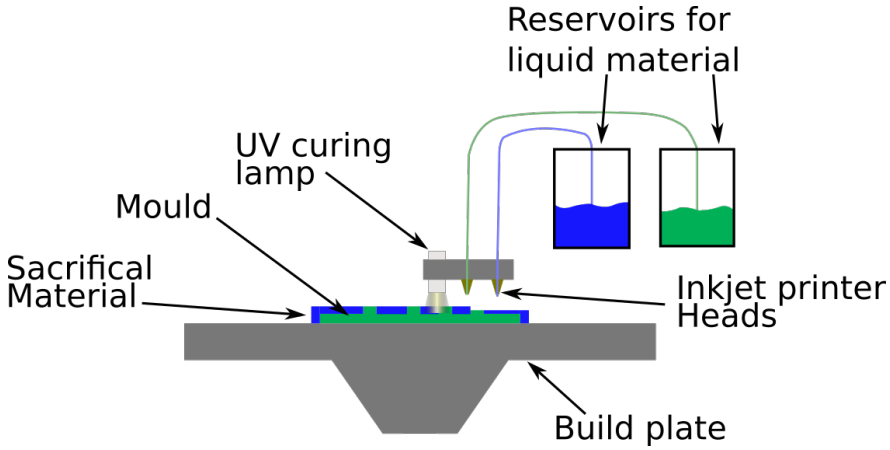

Figure 2.12: Schematic showing MJM printing technique; sacrificial material (blue) and photopolymer (green) is applied before UV lamp cures the polymers (adapted from Bhattacharjee et al. [2016]).

2.3.3.3 Stereolithography (SLA)

SLA involves a focused light source such as a laser to cure a photocurable resin layer by layer. There are two orientations for SLA, free surface (Figure 2.13a), where the resin is cured at the top surface exposed to the air and the base submerges for the next layer, and the constrained surface (Figure 2.13b), where the metal base is suspended upside down and resin curing on the bottom surface of the vat. After each layer is printed the resin is detached from the vat and the metal base is raised. The free surface technique has better structural strength, as the detaching in the constrained form can produce stress fractures, bend delicate

features and increases the roughness between the layers [Bhattacharjee et al., 2016]. The advantage of the constrained method is that each layer cures quicker, since it is not exposed to oxygen, which inhibits curing. A method of improving the speed of SLA printing is to use a DMD or digital light processing (DLP) projector, which allows the whole layer of the resin to be exposed and cured at once [Sochol et al., 2018]. Continuous liquid interface production (CLIP) is a recent development that also increases print speed, removing the need to detach the print form the bottom surface (Figure 2.13c) by having an oxygen permeable window on the vat base. As oxygen inhibits the curing process, this creates a layer of uncured resin between the printing surface and the base, which constantly fills the gap when the base is raised. Microchannels can be created directly using SLA, whereas the channel walls are cured the uncured resin is drained. The size of the channel is dependent on the size of the laser spot-size or pixel resolution but also the type and viscosity of the resin which has to be removed. SLA also requires time consuming post processing to remove uncured resin and it is restricted to one material per print since only one resin can be stored per vat.

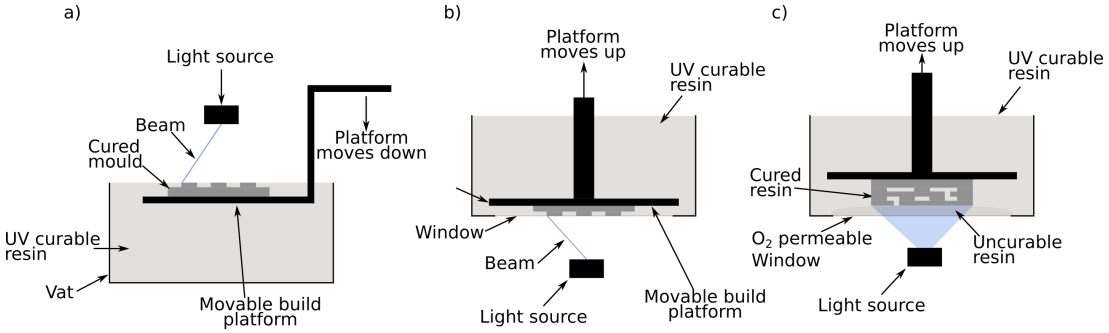

Figure 2.13: Schematics showing (a) SLA in free surface configuration, resin cured from above as build platform is lowered into vat; (b) SLA in constrained configuration, resin cured from below as the build platform is raised; and (c) CLIP printing technique,resin continuously enters curing region.

2.4 Device design

In this section, the design requirements for ATR-FTIR spectroscopy will be presented in order to justify design decisions. A number of existing devices that separate blood components are presented, as they are a good source of inspiration for any designer, and finally the proposed design is then presented.

2.4.1 Considerations

For ATR-FTIR spectroscopic diagnostics to be possible in the field, in remote locations and for emergency deployment, a sample preparation method has to be on site. The proposed device would ideally need to process a single 10 ml blood sample into serum, infected and damaged RBCs, WBCs and CTCs. The outputs must be of a quality that can then be used for analysis. As ATR-FTIR diagnostics is still a developing technique so there is no standard method for the process, which has made placing hard design limits for the outputs impossible. As mentioned in Section 2.2.2.1, affinity ligands are used for isolating components of interest but due to its interference with the ATR-FTIR spectra cannot be used in preparation of samples for ATR-FTIR spectroscopy. Therefore, devices that prepare samples for techniques, such as enzyme linked immunosorbant assay (ELISA) and Raman spectroscopy, that uses affinity ligands for preparations were ignored. As ATR-FTIR absorbance spectra can be influenced by reagents, the device is required to minimise the addition of infrared (IR) active material to process the sample, as well as compensating for its effect on the IR spectra. For this POC use, the effect of refrigeration and freezing on the sample was not considered in the design process as there is no need to refrigerate of freeze the samples during processing. Portability is one of the key requirements for devices used in remote locations and for emergency deployment, with the size of a complete device would be established after consultation with potential users. This requirement will also

limit the amount of power required for the device, as it would limit the size of the battery. As taking a spectra using ATR-FTIR takes minutes and analysis not much longer, the sample processing time should also be of a similar time scale to ensure high throughput, especially in disaster situations. Centrifugal microfluidics is a promising area for sample preparation but was rejected due to the perceived difficulty of potentially combining into a portable ATR-FTIR diagnostic unit; it is hard to control the final position of a spinning LOAD and therefore, aligning the external ports required for transferring products to the analysis unit would be difficult to design. The final consideration is that the individual chips have to be disposable through existing clinical waste routes, which means a low unit cost for the consumable chip.

2.4.2 Existing work

As has already been discussed in this Chapter, microfluidics is a large field with many potential solutions for preparing blood samples available in the literature. In this section we will introduce some relevant examples of devices for blood preparation, where multiple methods, presented in section 2.2, are combined in chips to achieve the desired outputs. There are many ways to achieve plasma separation, and Maria et al. [2015] and Tripathi et al. [2015] provide good reviews of the existing work in this area. Filtering is the easiest to use for extracting plasma and Ulum et al. [2016] developed a technique using a cotton thread that extracted plasma within three minutes. In this case plasma is driven by capillary action and the cells are trapped in the thread due to partial coagulation. This simple method requires no reagents and can be easily deployed to remote regions. Another low cost unpowered system was developed by Liu et al. [2013], where they created two compartments out of poly-methylmethacrylate (PMMA) separated by a plasma filtering membrane. Blood settles in the input compartment and plasma filters through the vertical filter and is collected in the second com-

partment. This simple design can process 1.8 ml of blood to produce around 270 µl of plasma within seven minutes. An equally simple system, developed by Kim et al. [2017], is an adaptation of a standard pipette tip that aspirates whole blood and deposits plasma while retaining the RBCs. The adaptor uses hydropheretic microchannel to guide the RBCs to a storage chamber. The limitation of this device is the low yield, 8.0% for 41% haematocrit. Other passive techniques such as IF have been used for plasma separation but requires the sample to be diluted. For instance, Rafeie et al. [2016] created 16 spiral channels in parallel that can process 540 $\mu l\,min^{-1}$. As stated earlier, this method requires the blood to be diluted and results in dilute plasma, which would either need to be concentrated, or the detection method used would need to be very sensitive. Kim et al. [2016] developed a disposable chip, using a serpentine channel and an alternating magnetic field to trap RBCs for collecting cell free plasma, which, like IF, is only suitable for dilute samples and therefore would produce dilute plasma. Another device that uses magnetic fields is HERMES, which is a low-cost functional device that rapidly separates plasma from blood in less than 2 minutes and can be used by an untrained operator [Vemulapati and Erickson, 2018]. This device uses functionalised magnetic beads to capture RBCs which are trapped due to a magnetic field. This method works well since the blood sample is from a finger prick and therefore will not contain significant other cells such WBC or CTC. This device still requires a number of user steps to produce a plasma sample for down stream analysis for less than $2 a test.

Cancer detection can be based on isolating the cancer cell from the blood sample and ignoring the other fractions. The CTC-i chip developed by Fachin et al. [2017] combines multiple microfluidic techniques to isolate CTCs; DLD to remove RBC and platelets followed by inertial focusing and MACS sequentially. Inertial focusing then align the nucleic cells and MACS removes magnetically labelled WBC. The cells go through the IF and MACS twice to ensure higher purity of

the captured CTC. The negative selection of CTCs allows for less interference for downstream analysis of the cells. Zhang et al. [2018b] developed an automatic CTC separating device using two stages of four spiral channels for IF separation. It is label free and has high throughput but operates on diluted blood. The chips were made by xurography in multiple parts, inlet, outlet, separation and flow autoregulation, which resulted in the final chip being compact; 51x53 mm^2 and a thickness of 2.7 mm. One thing to note is that this method of manufacturing has a limitation if production has to be scaled up, as identified by Zhang et al. [2018b].

Even though there are a lot of technologies presented, very few have been commercially produced [Shields IV et al., 2017]. The devices presented in Shields IV et al. [2017], and Jackson et al. [2017] are specifically for diagnosis of cancers and are designed to produce single outputs, CTC and WBC. An example of which is the VTX-I system [Lemaire et al., 2018], which uses vortex technology; inertial focussing with microscale vortices, which disrupts the path of the RBCs and WBCs as well as the larger CTCs. The chips are made from PMMA and are able to be manufactured on a large scale, with validation for research use making it a commercially viable product. These examples show the challenge involved in preparing samples for high purity and yield. Therefore, to ensure the same quality for preparing multiple blood fractions from a single sample would require a multiple stage chip and an equally complex instrument to control the fluidics.

2.4.3 Proposed device

In this section we will describe and justify a potential microfluidic device. A schematic of the four stage concept, presenting the sample processing steps, is shown in Figure 2.14, with the inputs and outputs of each stage designed to minimise dilution and contamination of the diagnostic outputs. As healthy RBCs provide no diagnostic evidence using ATR-FTIR spectroscopy and they make up

the majority of the blood composition, in Stage 1 of the design concept removes them first from blood. This leaves a fluid containing the diagnostically relevant material, the infected RBCs, WBCs, CTCs and proteins, referred to as the diagnostic fluid. The next step (Stage 2) would be to separate the relevant cells from the diagnostic fluid leaving a plasma-like fluid. From this stage onwards, the cells and plasma-like fluid would be processed separately, with the plasma-like fluid travelling to Stage 3 to be processed into serum, which as stated earlier is commonly used in ATR-FTIR spectroscopy. In Stage 4 the diagnostically relevant cells would be separated from each other and collected in individual wells. This could be achieved with either active or passive separation methods and would require the addition of a carrier fluid. As long as the carrier fluid does not contain IR active components, the cells can easily be concentrated and dried without affecting the quality of the analysis.

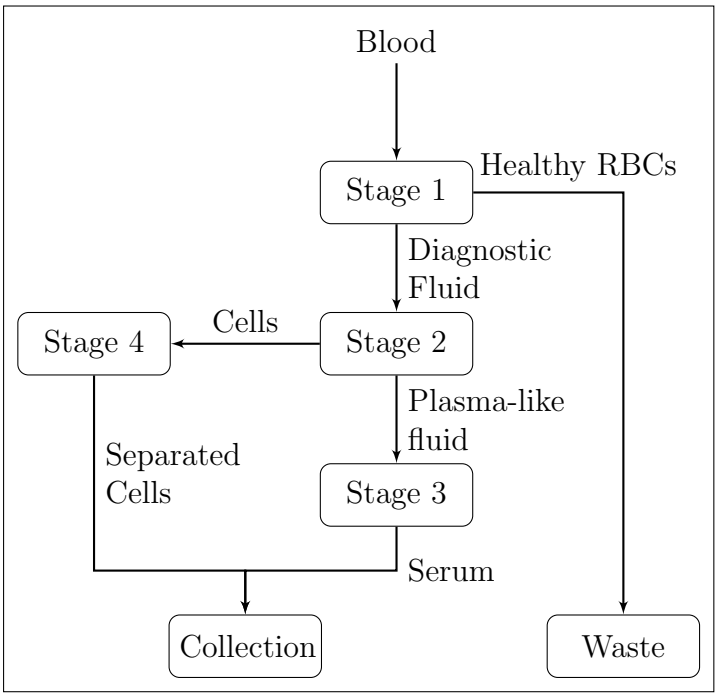

Figure 2.14: Schematic of proposed device

2.4.3.1 Stage 1

Hemodynamic (Section 2.2.1.5) and filtration (Section 2.2.1.2) methods are the only ones that can be used on undiluted blood. However, the problem with filtration is that the diagnostically relevant cells are larger than the RBCs and therefore would need at least a 2 different sized filters to retain the fluid component and diagnostically relevant cells. As infected RBCs have similar dimensions to healthy RBCs, an extremely precise filter, based on deformability, would be needed to separate them, which is not practical. Due to the issue of saturation, a large area membrane filter would be needed. A cross flow filter arrangement involving two filters would be technically challenging due to controlling multiple flows, the diagnostically relevant cells, the RBCs and plasma. Hemodynamic methods do not suffer from these issues; ie. the FL effect allows for the collection of the fluid component and margination allows for the collection of the diagnostically relevant cells [Shatova et al., 2016]. Additionally,Hou et al. [2016] has shown that their continuous device can separate pathogens, leukocytes and cytokines from blood for treatment of sepsis using margination. The healthy blood could then be returned back into the patient. However, designing the channel geometry to collect the diagnostic relevant cells, the plasma-like fluid, while minimising the contamination caused by healthy RBC will require a lot of optimisation.

2.4.3.2 Stage 2

At this point, the concentration of cells in the diagnostic fluid will be lower compared to whole blood. The simplest way to separate sparse cells from fluid is to use filtration, with cross-flow filtration being the preferred method as it will maintain good throughput by minimising saturation. The buffer required can be used in transferring the cells to Stage 3 without diluting the plasma-like fluid, as mixing does not occur in laminar flow.

2.4.3.3 Stage 3

To achieve serum as an output, the plasma-like fluid will have to be coagulated. Therefore, the aim in this stage is to neutralise the anticoagulant thus triggering clotting in a chamber, from which the fluid can be filtered out. To enable this, the chamber will need to be designed to allow complete mixing of the neutralising reagent and for the clotted components to be trapped within the chamber. Mixing, as stated in Section 2.2.3, is achieved by creating turbulent flow and passive mixing techniques would be considered first since active mixers require additional components, and control of bubbles will be more difficult in POC applications. Using affinity ligands (see Section 2.2.2.1) to bind the clotted material to posts was considered but the additional cost and extra consideration for fabrication made it unappealing. As a small amount of serum is required for ATR-FTIR spectroscopy saturation of a filter was not of concern so that, standard plasma filters could be used.

2.4.3.4 Stage 4

The separation of the cells by type can be achieved by multiple methods both active and passive and therefore all should be considered. The only exception is methods that incorporate affinity ligands, as stated earlier (see section 2.4.1), interferes with the infrared spectra. Active methods are not the first option due to the need for the additional components; magnets, electrodes accoustic and optical systems, which would have additional costs associated with fabrication. These methods would be suitable if more precise separation was needed. Passive techniques would only need an additional flow controller to set the correct flow rate for the chosen method. IF, HF and DLD are suitable methods for separating the different cells but IF is preferable due to operating at higher flow rate than DLD; fabrication is simpler than HF, as it is a single level design compared to two.

PFF would require an additional carrier fluid whereas the three previous methods can be controlled by the single buffer introduced at Stage 2 and by controlling channel geometry. A series of posts in a spiral channel, demonstrated by Geng et al. [2013], could be used to continuously separate different sizes of cells. Here larger cells could be collected at the end of the main channel, with smaller cells passing through the posts and collected in secondary channels while keeping a high flow rate. The transfer of these outputs to the ATR-FTIR spectroscopy crystal would still need be looked at and this can be addressed later.

2.5 Conclusion

Due to the complexity of the presented design, the number of stages and the number of additional buffers required, a multi-layered device is needed. This would restrict fabrication methods to soft lithography, 3D printing technologies such as SLA and CLIP and injection moulding. Different manufacturing methods are suitable for different quantities of production. At this stage, due to the lack of market penetration of clinical ATR-FTIR spectroscopy, designs should be prepared for the possibility of being mass produced via injection moulding but priority should be for cost effective batch production. Some techniques are suitable for rapid prototyping but cannot be scaled up, such as soft lithography. Even with reducing the cost of making the master mould either via reducing the cost of photolithography by using transparencies; by using print and peel (PAP) or 3D printing technologies to make the master moulds; soft lithography is still manually intensive and therefore can only produce small batches of chips. Designing for SLA and CLIP would allow more complicated single part devices, decent batch sizes and the design can be transferred more easily for injection moulding if there is higher demand.

The intended outputs of this device are serum, infected/damaged RBCs,

WBCs and CTCs. The design is an initial concept and feasibility will need to be established for each stage as well as flow parameters between the stages. Different stages or the whole design might need to be multiplexed in order to process the sample within an appropriate time.

There are many parameters that still need to be investigated and the next chapter will explore creating serum in Stage 3 for use in ATR-FTIR spectroscopy.

2.6 References

Amini, H., Lee, W. and Di Carlo, D. [2014], 'Inertial microfluidic physics', *Lab on a Chip* **14**(15), 2739–2761.

Atajanov, A., Zhbanov, A. and Yang, S. [2018], 'Sorting and manipulation of biological cells and the prospects for using optical forces', *Micro and Nano Systems Letters* **6**(1), 1–16.

Attia, U. M., Marson, S. and Alcock, J. R. [2009], 'Micro-injection moulding of polymer microfluidic devices', *Microfluidics and nanofluidics* **7**(1), 1.

Bhamla, M. S., Benson, B., Chai, C., Katsikis, G., Johri, A. and Prakash, M. [2017], 'Hand-powered ultralow-cost paper centrifuge', *Nature Biomedical Engineering* **1**(1), 1–7.

Bhardwaj, P., Bagdi, P. and Sen, A. [2011], 'Microfluidic device based on a micro-hydrocyclone for particle–liquid separation', *Lab on a Chip* **11**(23), 4012–4021.

Bhattacharjee, N., Urrios, A., Kang, S. and Folch, A. [2016], 'The upcoming 3d-printing revolution in microfluidics', *Lab on a Chip* **16**(10), 1720–1742.

Bishop, G. W., Satterwhite-Warden, J. E., Kadimisetty, K. and Rusling, J. F. [2016], '3d-printed bioanalytical devices', *Nanotechnology* **27**(28), 284002.

Boyd-Moss, M., Baratchi, S., Di Venere, M. and Khoshmanesh, K. [2016], 'Self-contained microfluidic systems: a review', *Lab on a Chip* **16**(17), 3177–3192.

Cai, G., Xue, L., Zhang, H. and Lin, J. [2017], 'A review on micromixers', *Micromachines* **8**(9), 274.

Catarino, S. O., Rodrigues, R. O., Pinho, D., Miranda, J. M., Minas, G. and Lima, R. [2019], 'Blood cells separation and sorting techniques of passive microfluidic devices: From fabrication to applications', *Micromachines* **10**(9), 593.

Chang, Y. M., Donovan, M. J. and Tan, W. [2013], 'Using aptamers for cancer biomarker discovery', *Journal of nucleic acids* **2013**.

Che, J., Yu, V., Dhar, M., Renier, C., Matsumoto, M., Heirich, K., Garon, E. B., Goldman, J., Rao, J., Sledge, G. W. et al. [2016], 'Classification of large circulating tumor cells isolated with ultra-high throughput microfluidic vortex technology', *Oncotarget* **7**(11), 12748.

Chen, L., Bode, A. M. and Dong, Z. [2017], 'Circulating tumor cells: moving biological insights into detection', *Theranostics* **7**(10), 2606.

Cheng, Z., Gu, Y., Li, S., Wang, Y., Chen, H., Cheng, J. and Liu, P. [2017], 'Enclosed casting of epoxy resin for rapid fabrication of rigid microfluidic chips', *Sensors and Actuators B: Chemical* **252**, 785–793.

Chiou, P. Y., Ohta, A. T. and Wu, M. C. [2005], 'Massively parallel manipulation of single cells and microparticles using optical images', *Nature* **436**(7049), 370–372.

Choi, S. and Park, J.-K. [2007], 'Continuous hydrophoretic separation and sizing of microparticles using slanted obstacles in a microchannel', *Lab on a Chip* **7**(7), 890–897.

Chun, B. and Ladd, A. [2006], 'Inertial migration of neutrally buoyant particles in a square duct: An investigation of multiple equilibrium positions', *Physics of Fluids* **18**(3), 031704.

Di Carlo, D. [2009], 'Inertial microfluidics', *Lab on a Chip* **9**(21), 3038–3046.

Di Carlo, D., Irimia, D., Tompkins, R. G. and Toner, M. [2007], 'Continuous inertial focusing, ordering, and separation of particles in microchannels', *Proceedings of the National Academy of Sciences* **104**(48), 18892–18897.

Dincau, B. M., Aghilinejad, A., Hammersley, T., Chen, X. and Kim, J.-H. [2018], 'Deterministic lateral displacement (dld) in the high reynolds number regime: high-throughput and dynamic separation characteristics', *Microfluidics and Nanofluidics* **22**(6), 59.

Dixit, C., Kadimisetty, K. and Rusling, J. [2018], '3d-printed miniaturized fluidic tools in chemistry and biology', *TrAC Trends in Analytical Chemistry* **106**, 37–52.

Dixon, C., Lamanna, J. and Wheeler, A. R. [2017], 'Printed microfluidics', *Advanced Functional Materials* **27**(11), 1604824.

Ducrée, J., Haeberle, S., Lutz, S., Pausch, S., Von Stetten, F. and Zengerle, R. [2007], 'The centrifugal microfluidic bio-disk platform', *Journal of Micromechanics and Microengineering* **17**(7), S103.

Fachin, F., Spuhler, P., Martel-Foley, J. M., Edd, J. F., Barber, T. A., Walsh, J., Karabacak, M., Pai, V., Yu, M., Smith, K. et al. [2017], 'Monolithic chip for high-throughput blood cell depletion to sort rare circulating tumor cells', *Scientific reports* **7**(1), 1–11.

Fahraeus, R. and Lindqvist, T. [1931], 'The viscosity of the blood in narrow

capillary tubes', *American Journal of Physiology-Legacy Content* **96**(3), 562–568.

Faustino, V., Catarino, S. O., Lima, R. and Minas, G. [2016], 'Biomedical microfluidic devices by using low-cost fabrication techniques: A review', *Journal of biomechanics* **49**(11), 2280–2292.

Faustino, V., Catarino, S. O., Pinho, D., Lima, R. A. and Minas, G. [2018], 'A passive microfluidic device based on crossflow filtration for cell separation measurements: A spectrophotometric characterization', *Biosensors* **8**(4), 125.

Gale, B. K., Jafek, A. R., Lambert, C. J., Goenner, B. L., Moghimifam, H., Nze, U. C. and Kamarapu, S. K. [2018], 'A review of current methods in microfluidic device fabrication and future commercialization prospects', *Inventions* **3**(3), 60.

Garg, N., Westerhof, T. M., Liu, V., Liu, R., Nelson, E. L. and Lee, A. P. [2018], 'Whole-blood sorting, enrichment and in situ immunolabeling of cellular subsets using acoustic microstreaming', *Microsystems & Nanoengineering* **4**(1), 1–9.

Geng, Z., Ju, Y., Wang, W. and Li, Z. [2013], 'Continuous blood separation utilizing spiral filtration microchannel with gradually varied width and micropillar array', *Sensors and Actuators B: Chemical* **180**, 122–129.

Guckenberger, D. J., de Groot, T. E., Wan, A. M., Beebe, D. J. and Young, E. W. [2015], 'Micromilling: a method for ultra-rapid prototyping of plastic microfluidic devices', *Lab on a Chip* **15**(11), 2364–2378.

Hou, H. W., Wu, L., Amador-Munoz, D. P., Vera, M. P., Coronata, A., Englert, J. A., Levy, B. D., Baron, R. M. and Han, J. [2016], 'Broad spectrum immunomodulation using biomimetic blood cell margination for sepsis therapy', *Lab on a Chip* **16**(4), 688–699.

Hur, S. C., Choi, S.-E., Kwon, S. and Carlo, D. D. [2011], 'Inertial focusing of non-spherical microparticles', *Applied Physics Letters* **99**(4), 044101.

Hyun, J.-c., Hyun, J., Wang, S. and Yang, S. [2017], 'Improved pillar shape for deterministic lateral displacement separation method to maintain separation efficiency over a long period of time', *Separation and Purification Technology* **172**, 258–267.

Inglis, D. W., Davis, J. A., Austin, R. H. and Sturm, J. C. [2006], 'Critical particle size for fractionation by deterministic lateral displacement', *Lab on a Chip* **6**(5), 655–658.

Jackson, J. M., Witek, M. A., Kamande, J. W. and Soper, S. A. [2017], 'Materials and microfluidics: enabling the efficient isolation and analysis of circulating tumour cells', *Chemical Society Reviews* **46**(14), 4245–4280.

Jeon, J. S., Chung, S., Kamm, R. D. and Charest, J. L. [2011], 'Hot embossing for fabrication of a microfluidic 3d cell culture platform', *Biomedical microdevices* **13**(2), 325–333.

Kahkeshani, S., Haddadi, H. and Di Carlo, D. [2016], 'Preferred interparticle spacings in trains of particles in inertial microchannel flows', *J. Fluid Mech* **786**, R3.

Kang, Y. J., Ha, Y.-R. and Lee, S.-J. [2016], 'High-throughput and label-free blood-on-a-chip for malaria diagnosis', *Analytical chemistry* **88**(5), 2912–2922.

Kim, B., Oh, S., You, D. and Choi, S. [2017], 'Microfluidic pipette tip for high-purity and high-throughput blood plasma separation from whole blood', *Analytical chemistry* **89**(3), 1439–1444.

Kim, J.-A., Lee, J., Wu, C., Nam, S., Di Carlo, D. and Lee, W. [2016a], 'Inertial

focusing in non-rectangular cross-section microchannels and manipulation of accessible focusing positions', *Lab on a Chip* **16**(6), 992–1001.

Kim, P., Ong, E. H., Li, K. H. H., Yoon, Y.-J., Ng, S. H. G. and Puttachat, K. [2016], 'Low-cost, disposable microfluidics device for blood plasma extraction using continuously alternating paramagnetic and diamagnetic capture modes', *Biomicrofluidics* **10**(2), 024110.

Kipling, G., Haswell, S. and Brown, N. [2015], A considered approach to lab-on-a-chip fabrication, *in* 'Lab-on-a-Chip Devices and Micro-Total Analysis Systems', Springer, pp. 53–82.

Kipper, S., Frolov, L., Guy, O., Pellach, M., Glick, Y., Malichi, A., Knisbacher, B. A., Barbiro-Michaely, E., Avrahami, D., Yavets-Chen, Y. et al. [2017], 'Control and automation of multilayered integrated microfluidic device fabrication', *Lab on a Chip* **17**(3), 557–566.

Laser, D. J. and Santiago, J. G. [2004], 'A review of micropumps', *Journal of micromechanics and microengineering* **14**(6), R35.

Le, N. N., Huynh, K. K., Phan, T. C. H., Dang, T. M. D. and Dang, M. C. [2017], 'Fabrication of 25 μm-filter microfluidic chip on silicon substrate', *Advances in Natural Sciences: Nanoscience and Nanotechnology* **8**(1), 015003.

Lee, C.-Y., Chang, C.-L., Wang, Y.-N. and Fu, L.-M. [2011], 'Microfluidic mixing: a review', *International journal of molecular sciences* **12**(5), 3263–3287.

Lemaire, C. A., Liu, S. Z., Wilkerson, C. L., Ramani, V. C., Barzanian, N. A., Huang, K.-W., Che, J., Chiu, M. W., Vuppalapaty, M., Dimmick, A. M. et al. [2018], 'Fast and label-free isolation of circulating tumor cells from blood: From a research microfluidic platform to an automated fluidic instrument, vtx-1 liq-

uid biopsy system', *SLAS TECHNOLOGY: Translating Life Sciences Innovation* **23**(1), 16–29.

Liu, C., Hu, G., Jiang, X. and Sun, J. [2015], 'Inertial focusing of spherical particles in rectangular microchannels over a wide range of reynolds numbers', *Lab on a Chip* **15**(4), 1168–1177.

Liu, C., Mauk, M., Gross, R., Bushman, F. D., Edelstein, P. H., Collman, R. G. and Bau, H. H. [2013], 'Membrane-based, sedimentation-assisted plasma separator for point-of-care applications', *Analytical chemistry* **85**(21), 10463–10470.

Luo, X., Cao, J., Gong, H., Yan, H. and He, L. [2018], 'Phase separation technology based on ultrasonic standing waves: A review', *Ultrasonics sonochemistry* **48**, 287–298.

Maria, M. S., Kumar, B., Chandra, T. and Sen, A. [2015], 'Development of a microfluidic device for cell concentration and blood cell-plasma separation', *Biomedical microdevices* **17**(6), 115.

Martel, J. M. and Toner, M. [2012], 'Inertial focusing dynamics in spiral microchannels', *physics of fluids* **24**(3), 032001.

Martel, J. M. and Toner, M. [2013], 'Particle focusing in curved microfluidic channels', *Scientific Reports* **3**(1), 1–8.

Martel, J. M. and Toner, M. [2014], 'Inertial focusing in microfluidics', *Annual review of biomedical engineering* **16**, 371–396.

McDonald, J. C. and Whitesides, G. M. [2002], 'Poly (dimethylsiloxane) as a material for fabricating microfluidic devices', *Accounts of chemical research* **35**(7), 491–499.

McGrath, J., Jimenez, M. and Bridle, H. [2014], 'Deterministic lateral displacement for particle separation: a review', *Lab on a Chip* **14**(21), 4139–4158.

Morgan, A. J., Hidalgo San Jose, L., Jamieson, W. D., Wymant, J. M., Song, B., Stephens, P., Barrow, D. A. and Castell, O. K. [2016], 'Simple and versatile 3d printed microfluidics using fused filament fabrication', *PloS one* **11**(4), e0152023.

Morijiri, T., Yamada, M., Hikida, T. and Seki, M. [2013], 'Microfluidic counterflow centrifugal elutriation system for sedimentation-based cell separation', *Microfluidics and nanofluidics* **14**(6), 1049–1057.

Nguyen, N.-T. and Wu, Z. [2004], 'Micromixers—a review', *Journal of micromechanics and microengineering* **15**(2), R1.

Owens, C. E. and Hart, A. J. [2018], 'High-precision modular microfluidics by micromilling of interlocking injection-molded blocks', *Lab on a Chip* **18**(6), 890–901.

Pariset, E., Pudda, C., Boizot, F., Verplanck, N., Berthier, J., Thuaire, A. and Agache, V. [2017], 'Anticipating cutoff diameters in deterministic lateral displacement (dld) microfluidic devices for an optimized particle separation', *Small* **13**(37), 1701901.

Prakash, S. and Yeom, J. [2014], Advanced fabrication methods and techniques, *in* 'Nanofluidics and Microfluidics: Systems and Applications', William Andrew, pp. 87–170.

Rafeie, M., Zhang, J., Asadnia, M., Li, W. and Warkiani, M. E. [2016], 'Multiplexing slanted spiral microchannels for ultra-fast blood plasma separation', *Lab on a Chip* **16**(15), 2791–2802.

Sajeesh, P. and Sen, A. K. [2014], 'Particle separation and sorting in microfluidic devices: a review', *Microfluidics and nanofluidics* **17**(1), 1–52.

Shatova, T. A., Lathwal, S., Engle, M. R., Sikes, H. D. and Jensen, K. F. [2016], 'Portable, constriction–expansion blood plasma separation and polymerization-based malaria detection', *Analytical chemistry* **88**(15), 7627–7632.

Shields IV, C. W., Ohiri, K. A., Szott, L. M. and López, G. P. [2017], 'Translating microfluidics: Cell separation technologies and their barriers to commercialization', *Cytometry Part B: Clinical Cytometry* **92**(2), 115–125.

Shields IV, C. W., Reyes, C. D. and López, G. P. [2015], 'Microfluidic cell sorting: a review of the advances in the separation of cells from debulking to rare cell isolation', *Lab on a Chip* **15**(5), 1230–1249.

Sochol, R. D., Sweet, E., Glick, C. C., Wu, S.-Y., Yang, C., Restaino, M. and Lin, L. [2018], '3d printed microfluidics and microelectronics', *Microelectronic Engineering* **189**, 52–68.

Speller, N. C., Morbioli, G. G., Cato, M. E., Cantrell, T. P., Leydon, E. M., Schmidt, B. E. and Stockton, A. M. [2019], 'Cutting edge microfluidics: Xurography and a microwave', *Sensors and Actuators B: Chemical* **291**, 250–256.

Thurgood, P., Zhu, J. Y., Nguyen, N., Nahavandi, S., Jex, A. R., Pirogova, E., Baratchi, S. and Khoshmanesh, K. [2018], 'A self-sufficient pressure pump using latex balloons for microfluidic applications', *Lab on a Chip* **18**(18), 2730–2740.

Tosello, G. [2018], *Micro injection molding*, Carl Hanser Verlag GmbH Co KG.

Tripathi, S., Kumar, Y. B. V., Prabhakar, A., Joshi, S. S. and Agrawal, A. [2015], 'Passive blood plasma separation at the microscale: a review of design principles and microdevices', *Journal of Micromechanics and Microengineering* **25**(8), 083001.

Ulum, M. F., Maylina, L., Noviana, D. and Wicaksono, D. H. B. [2016], 'Edta-treated cotton-thread microfluidic device used for one-step whole blood plasma separation and assay', *Lab on a Chip* **16**(8), 1492–1504.

Vemulapati, S. and Erickson, D. [2018], 'Hermes: rapid blood-plasma separation at the point-of-need', *Lab on a Chip* **18**(21), 3285–3292.

Vernekar, R. and Krüger, T. [2015], 'Breakdown of deterministic lateral displacement efficiency for non-dilute suspensions: A numerical study', *Medical engineering & physics* **37**(9), 845–854.

Vernekar, R., Krüger, T., Loutherback, K., Morton, K. and Inglis, D. W. [2017], 'Anisotropic permeability in deterministic lateral displacement arrays', *Lab on a Chip* **17**(19), 3318–3330.

Walsh III, D. I., Kong, D. S., Murthy, S. K. and Carr, P. A. [2017], 'Enabling microfluidics: from clean rooms to makerspaces', *Trends in biotechnology* **35**(5), 383–392.

Wang, L., Kodzius, R., Yi, X., Li, S., Hui, Y. S. and Wen, W. [2012], 'Prototyping chips in minutes: Direct laser plotting (dlp) of functional microfluidic structures', *Sensors and Actuators B: Chemical* **168**, 214–222.

Warkiani, M. E., Wu, L., Tay, A. K. P. and Han, J. [2015], 'Large-volume microfluidic cell sorting for biomedical applications', *Annual Review of Biomedical Engineering* **17**, 1–34.

Weisgrab, G., Ovsianikov, A. and Costa, P. F. [2019], 'Functional 3d printing for microfluidic chips', *Advanced Materials Technologies* **4**(10), 1900275.

Whitesides, G. M. [2006], 'The origins and the future of microfluidics', *Nature* **442**(7101), 368–373.

Yu, Z. T. F., Aw Yong, K. M. and Fu, J. [2014], 'Microfluidic blood cell sorting: now and beyond', *Small* **10**(9), 1687–1703.

Zhang, X.-B., Wu, Z.-Q., Wang, K., Zhu, J., Xu, J.-J., Xia, X.-H. and Chen, H.-Y. [2012], 'Gravitational sedimentation induced blood delamination for continuous plasma separation on a microfluidics chip', *Analytical chemistry* **84**(8), 3780–3786.

Zhang, X., Huang, D., Tang, W., Jiang, D., Chen, K., Yi, H., Xiang, N. and Ni, Z. [2016], 'A low cost and quasi-commercial polymer film chip for high-throughput inertial cell isolation', *RSC advances* **6**(12), 9734–9742.

Zhang, X., Terstappen, L. W. and Beck, M. [2017], On-chip sample preparations for point-of-care cellular analysis of blood, *in* 'Point-of-Care Diagnostics-New Progresses and Perspectives', IAPC, pp. 115–139.

Zhang, X., Zhu, Z., Xiang, N., Long, F. and Ni, Z. [2018b], 'Automated microfluidic instrument for label-free and high-throughput cell separation', *Analytical chemistry* **90**(6), 4212–4220.

Zhang, Y., Lyons, V. and Pappas, D. [2018a], 'Fundamentals of affinity cell separations', *Electrophoresis* **39**(5-6), 732–741.

Zhou, J. and Papautsky, I. [2013], 'Fundamentals of inertial focusing in microchannels', *Lab on a Chip* **13**(6), 1121–1132.

Chapter 3: Producing Serum for ATR-FTIR spectroscopy

3.1 Introduction

Before developing a microfluidic device for preparing blood samples for ATR-FTIR diagnostics, it is necessary to investigate the required characteristics of the device outputs. Serum, as stated in Chapter 1, is the main sample type used in ATR-FTIR diagnostics but currently there are no reported assessments of the characteristics of serum for the robust classification of disease. In this chapter we first investigate whether necessary specifications on the quality of serum could be established, via an investigation of the effect of dilution and contamination of serum:

- Dilution: A sample that is too diluted may not be effectively classified by the diagnostic algorithm; therefore, a dilution limit needs to be set for the microfluidic device.
- Contamination: Other components may contaminate the desired output and need to be controlled as the diagnostic algorithms are currently designed for traditionally processed samples. The contamination level that stops the diagnostic algorithm detecting disease is a hard limit for the output of the proposed device.

The standard method of checking whether acquired spectra are suitable is to perform a quality test (QT), which checks parameters upon acquisition, in order to indicate whether the spectra can be used for analysis. For point-of-care (POC) application, it will also be beneficial to know if a sample is covering the internal

reflection element (IRE) and dried uniformly, before assessing the results of the test.

The coagulation cascade, introduced in Section 1.1.5, is responsible for the creation of serum but anticoagulants are needed to prevent blood from clotting in the sample tube or in the microfluidic device. In this chapter the possibility of reversing the effect of anticoagulants in order to trigger the conversion of the plasma-like fluid to serum as envisioned in Section 2.4.3 was investigated. The usage of ATR-FTIR spectroscopy to monitor the coagulation of plasma to serum equivalent fluid, as a tool for designing Stage 3, was not shown to be possible. Looking further into the inconclusive result, by investigating fundamental differences between plasma and serum spectra, lead to the conclusion that plasma was more suitable as an output sample for POC applications of the proposed device. Therefore it was concluded that Stage 3 of the proposed design is not needed.

3.2 Methodology: attenuated total reflectance (ATR)

The fundamentals of ATR-FTIR spectroscopy has already been explained in Section 1.2.2.2 and therefore will not be repeated.

3.2.1 Instrumentation

For the following experiments, one of two FTIR spectrometers were used; either the Cary 660 FTIR spectrometer (Agilent, U.S.A) or the Spectrum 2 (Perkin Elmer, U.S.A). Figure 3.1 shows the Cary 660 FTIR spectrometer with the miracle ATR accessory (Pike,U.S.A.) with Pro-resolutions (Agilent, U.S.A) software used for data acquisition using the following settings: the resolution was set to 4 cm^{-1}, in the range of 4000-1000 cm^{-1} and the spectra was averaged over 32

co-added scans. The Spectrum 2 is a bench top spectrometer and it comes with its Universal ATR accessory (Perkin Elmer, U.S.A), and is controlled via the Spectrum 10^{TM} software (Perkin Elmer, U.S.A). For this system all the spectra, the resolution was set to 4 cm^{-1}, in the range of 4000-600 cm^{-1} and the spectra was averaged over 16 co-added scans. The Spectrum 2 was used with silicon internal reflection elements (SIREs)(ClinspecDx, U.K) and Quest ATR accessory (Specac, U.K.)(Figure 3.2) for taking measurements form fresh (unfrozen) samples as it was a higher throughput method that is described in more detail in Section 3.2.2.2.

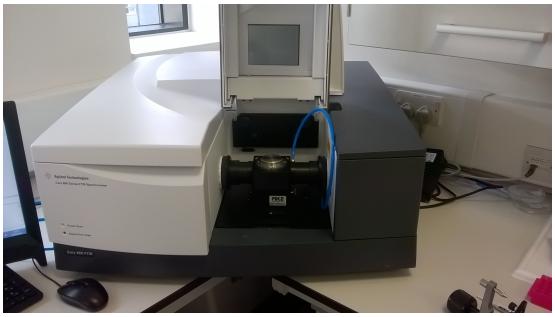

Figure 3.1: Cary 660 FTIR spectrometer

Figure 3.2: The Spectrum 2 FTIR spectrometer with Quest accessory and SIREs

3.2.2 Standard Methodology

3.2.2.1 Single internal reflection element (IRE)

The methodology for using the single diamond zinc selenide (DiZnSe) IRE was the same for both spectrometers [Hands et al., 2014]. The IRE was first cleaned with Virkon®, wiped dry before a second clean with ethanol before being wiped dry again. Background spectra were taken of the empty IRE. A 1 µl spot of the sample was pippetted onto the IRE and left to dry for 8 minutes before 3 spectra were taken. For each sample this process was repeated 3 times, which equates to 3 biological replicates and 3 machine replicates for each sample (9 spectra in total).

3.2.2.2 Silicon internal reflection element (SIRE)

The SIREs are composed of 4 wells with a silicon internal reflection element base, as shown in Figure 3.2, the first well is kept empty to use as the background and the remaining wells are spots for a single sample. 3 µl of sample is pippetted into each well and spread to cover the crystal. Once all the samples are pippetted onto the SIREs they are placed into a drying rack for 1 h at 30 °C. The increased time compared to single IRE method is due to larger sample volume and lack of air circulation within the rack. Once samples are dried, the samples are analysed slide by slide. Each slide is placed on the Quest ATR accessory (Specac, U.K.), with the empty well positioned in the beam path so that the background scan can be taken. The slide is repositioned for the next well, then another 3 spectra are taken. This process is repeated for the remaining wells, which results in 3 biological repeats and 3 machine replicates for each sample.

3.2.3 Data analysis

3.2.3.1 Preprocessing of Spectra

Regardless of the instrument used the collected spectra were exported as .csv files and imported into MATLAB (Mathworks, U.S.A). I created a code to carry out the preprocessing and data analysis using various functions from toolbox created by Biospec [2018]. Preprocessing consisted of taking the mean spectra for each machine replicate then the spectra underwent rubber band baseline correction, noise reduction, vector normalisation and the second derivative spectra were calculated using the Savitzky-Golay algorithm. The carbon dioxide spectral bands, found between 2403-2272 cm^{-1} and 682-655 cm^{-1}, were then removed, which reduces the effect of atmospheric variation in the spectra. The preprocessing workflow is shown in Figure 3.3 with example spectra.

3.2.3.2 Multivariate analysis: principle component analysis (PCA) and principle component discriminant functional analysis (PC-DFA)

After preprocessing, the spectra underwent multivariate analysis: principle component analysis (PCA) and some spectra also underwent principle component discriminant functional analysis (PC-DFA) (function codes acquired from Biospec [2018]). PCA is an unsupervised technique designed to reduce a dataset with a large number of variables, to one with a smaller set of variables, while keeping a large part of the spectral information. The original data set is transformed so that all the dimensions have a mean at the origin. From the data set about the origin, a covariance matrix is calculated. Covariance is a measure of how much the dimensions vary about the mean with respect to each other namely,

$$cov(X,Y) = \frac{\sum_{i=1}^{n}(X_i - \bar{X})(Y_i - \bar{Y})}{n-1}, \tag{3.1}$$

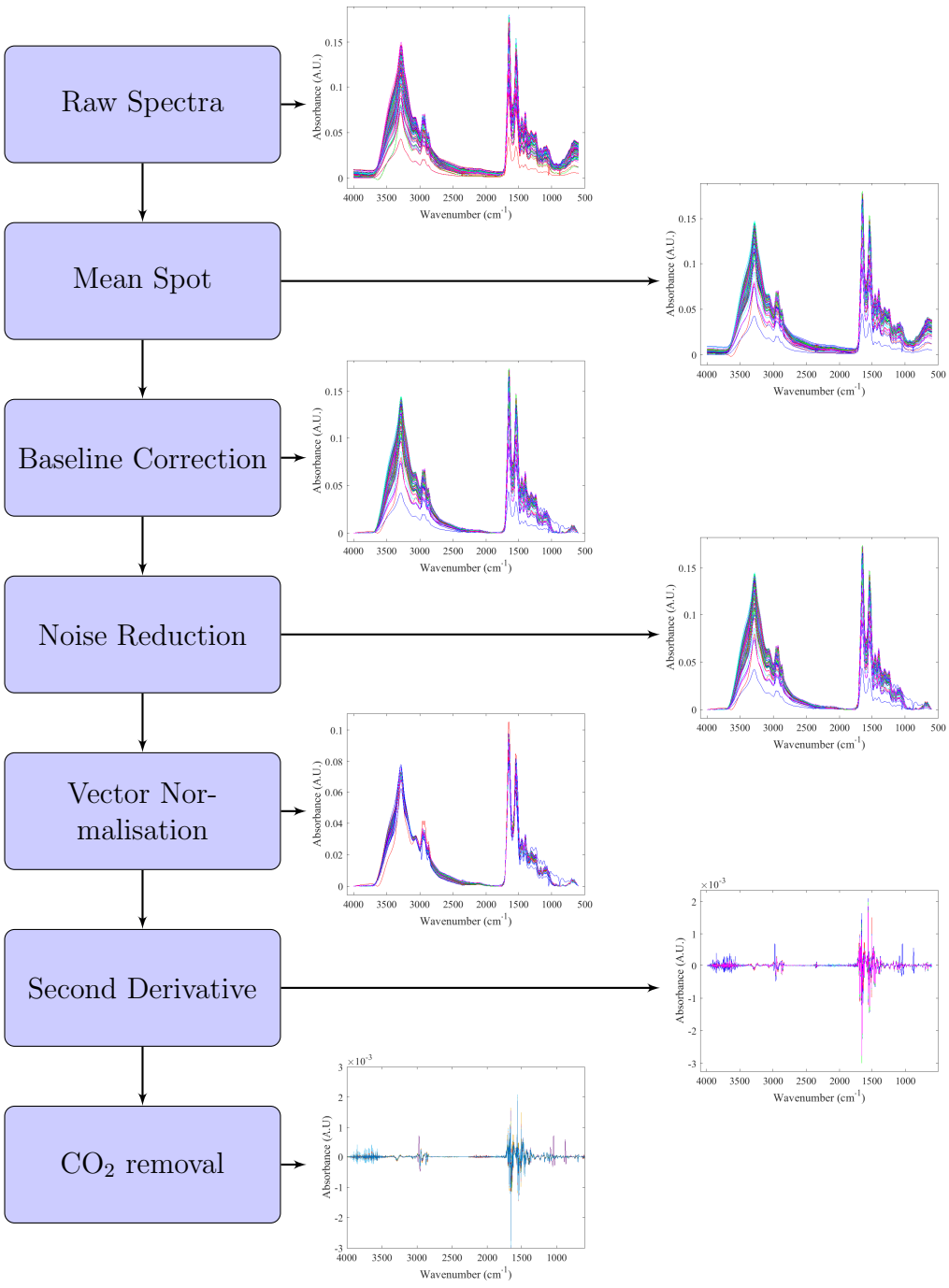

Figure 3.3: Standard preprocessing work flow showing how an example raw spectra changes with the preprocessing method. Mean of the machine repeats is carried out first followed by a rubberband baseline correction. PCA noise reduction and vector normalisation. The second derivative calculated via the Savisky-Golay algorithm and ending with the removal of the carbon dioxide bands.

where n is the number of observations, X and Y are independent variables. This is done on a pairwise basis so that

$$C_x^{m\times m} = cov(X_i, X_j), \tag{3.2}$$

for an m dimensioned data set, resulting in a square covariant matrix $C_x^{m\times m}$. From the covariance matrix the eigenvectors and corresponding eignevalues are calculated. Eigenvectors are vectors whose direction remains unchanged after undergoing a transformation, and the eigenvalues are the scalar multipliers of the eigenvector caused by the transformation. The covariance matrix can then be decomposed into a linear combination of independent components, where since eigenvalues are a measure of the degree of variation, the larger the eigenvalue the more significant the associated eigenvector is. Therefore, the eigenvectors can be ranked by decreasing significance, starting with the most significant, which are defined as PC1, PC2, PC3 etc.. The least significant components can then be ignored, thereby reducing the complexity of the data. The sorted reduced eignevector matrix, P, is then used to project the original dataset, X, into the new coordinates system, Y, thus

$$Y = PX. \tag{3.3}$$

In this new coordinate system, using the eignevector matrix makes the covariance matrix of Y diagonal, so that the covariance of the new system is zero. We may then construct a loading plot, which shows the value of each wavenumber when projected onto a specific principal component. The scores plot is then the sum of the components of the wavenumbers from each sample of X that are in the direction of each principal component. Percentage explained (PE) is the percentage of the total variation attributed to the specific principal component.

PC-DFA is a supervised cluster analysis technique and therefore requires in-

formation of the sample groups present in the data set in addition to the principle components. The principle components from the PCA are used to reduce the dimensionality of the data set and a new projection, DF1, is carried out whereby the intra-group variation is reduced and the inter-group variation is maximised [Gromski et al., 2015].

3.3 Determining device performance measurements for serum output

3.3.1 Quality test (QT)

As mentioned before, a quality test is used by spectrometers to indicate whether a taken spectrum contains reliable information. Failing the quality test indicates that there is a problem with either the sample application or the spectrometer settings. A bespoke QT code was created, specific for ATR-FTIR spectroscopy of biological samples, using five criteria: a minimum absorbance value (ABS), two signal to noise ratios (SNR1 and SNR2), and two water vapour ratios (WVR1 and WVR2). The minimum absorbance value was set to ten times the noise of the spectrometer and the remaining quality test criteria were taken from Zhang et al. [2013], which had been created for high throughput FTIR spectroscopy. The noise level was established by recording the maximum absorbance value of an air spectrum with an air background. The signal to noise ratio is calculated by dividing the maximum absorbance of the signal regions, the amide 1 peak between 1600 cm^{-1} and 1700 cm^{-1} in the case of SNR1, or between 1170 cm^{-1} and 1260 cm^{-1} for SNR2 by the noise region, found between 1900 cm^{-1} and 2000 cm^{-1}. WVR1 and WVR2 are the same signal regions as for SNRs ratios but instead of the noise region, the maximum absorbance of the water region; 1837 cm^{-1} - 1847 cm^{-1} is used. The work flow for the QT is given in Figure 3.4. Spectra that pass

all the criteria are considered valid and are then passed onto pre-processing and data analysis, which was carried out by the a bespoke integrated code.

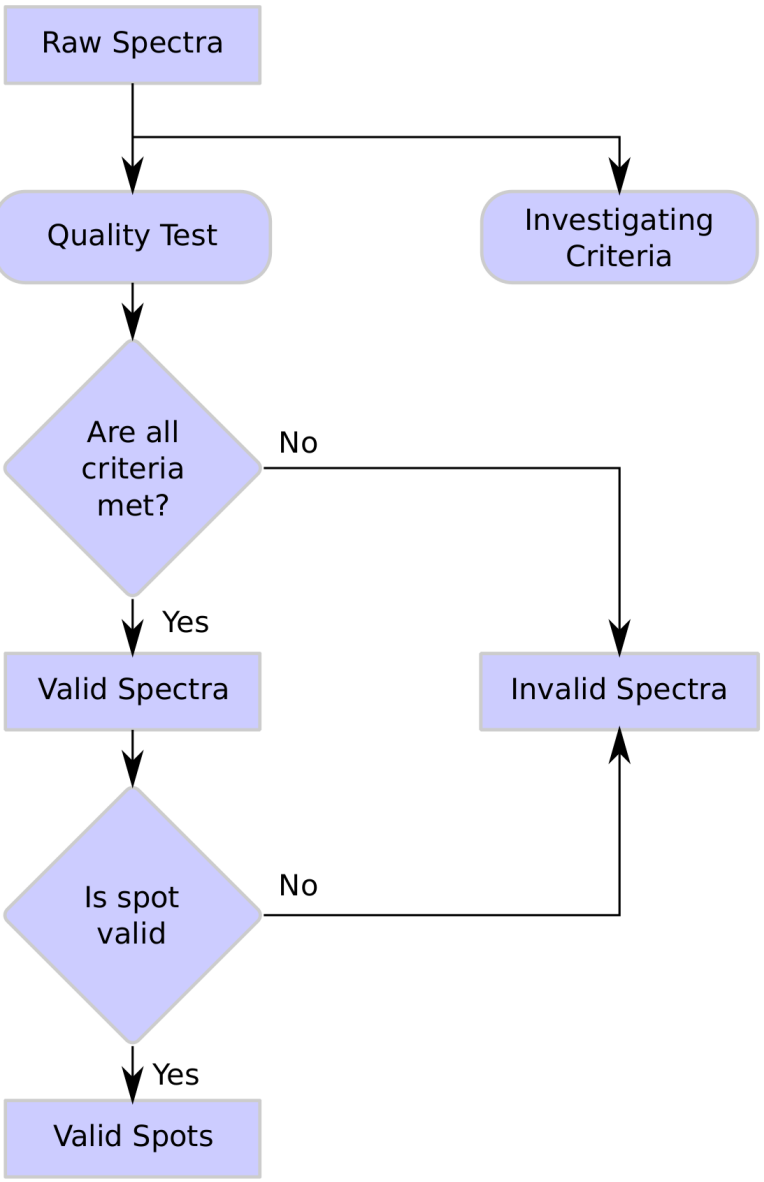

Figure 3.4: Flow chart showing the function of the created QT code.

3.3.2 Effect of buffer and red blood cells (RBCs) contamination in serum

As no system can be perfect, it would be valuable to know the tolerances of ATR-FTIR spectroscopy of serum to the effects of dilution and contamination, which could then be incorporated into the design process.

3.3.2.1 Materials and methods

Aliquots of phosphate buffered saline (PBS) were acquired from a stock solution made by dissolving PBS tablet (Sigma-Aldrich Co. LLC., Dorset, UK) in 200 ml of distilled water which contained 0.01 M phosphate buffer, 0.0027 M potassium chloride and 0.137 M sodium chloride, pH 7.4, at 25 °C. Human 0.2 µm sterile filtered mixed pooled serum (TCS Biosciences Ltd, Buckingham, UK) was defrosted overnight and was diluted with the PBS solution to form solutions containing 0%, 25%, 50%, 75% and 100% proportion of PBS in serum. Five aliquots of 1 ml stock were created for each solution then refrozen. Spectral collection was carried out using a Cary 660 FTIR spectrometer (Agilent, U.S.A) shown in Section 3.2.2.1. For each solution, 5 stock aliquots were defrosted to be tested within the day. The only change from the method stated in Section 3.2.2.1 was that 5 spots were used per aliquot, which resulted in 15 spectra per aliquot stock solution and 75 spectra per concentration.

3.3.2.2 Contamination of serum with red blood cells (RBCs)

Packed red blood cells (RBCs) (West of Scotland Blood Transfusion Centre, Glasgow, UK), from a single donor, were added to the pooled serum to make 5 storage tubes of 1 ml samples for each contamination proportions (by volume); 0%, 4%, 8%, 12%, 16%, 20%, 40% and 50% of RBC in serum. The samples were stored in a fridge to prevent haemolysis. Spectra were taken using the same method as the

dilution study but with three spots instead of five to reduce collection time. After taking the spectra, the samples were placed into a -80°C freezer to haemolyse the RBCs. Spectra were taken again in the same manner as the samples with the intact cells. The collected spectra was then processed using the integrated code mentioned in Section 3.3.1.

3.3.2.3 Results and Discussion

The quality test criteria were set as ABS > 0.04, SNR1 > 30, SNR2 > 10, WVR1 > 20, WVR2 > 4 according to Section 3.3.1.

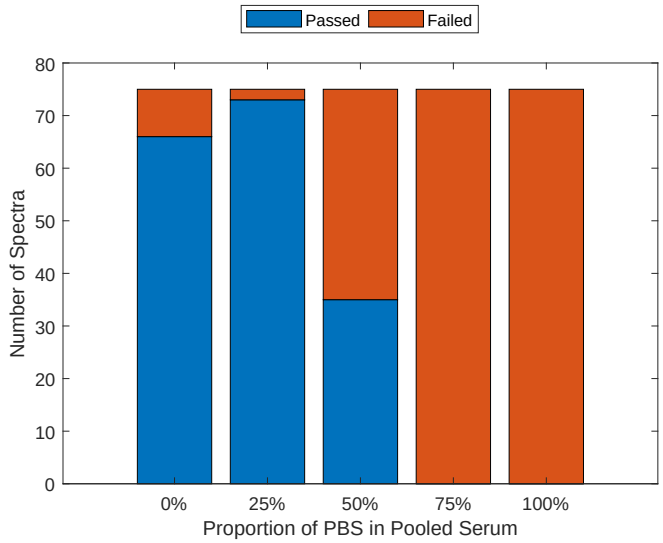

Figure 3.5: Results of quality test in dilution study.

The dilution study (see Figure 3.5) shows that increasing the amount of PBS, i.e. increasing dilution, prevents the spectrum from passing the quality test. It must be noted that all pure serum spectra were expected to pass the quality test but did not. This indicates that there was a problem with application of the sample to the IRE or the samples themselves. Figure 3.6 shows the PCA scores plot for the diluted serum samples. There is a clear separation between pure PBS and the serum solutions in PC1 as expected (Figure 3.6a and b). PC2 and

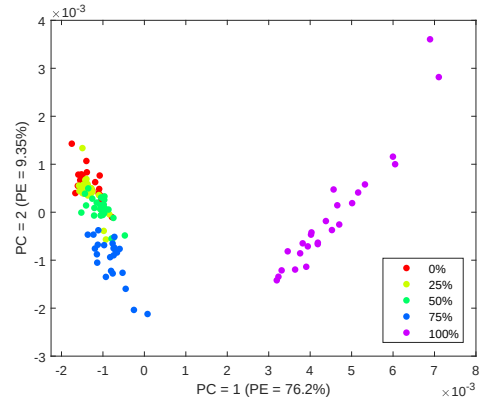

(a)

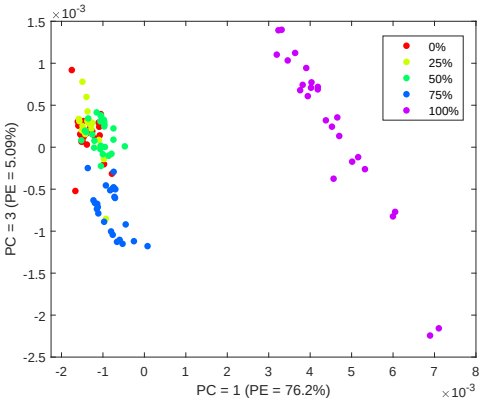

(b)

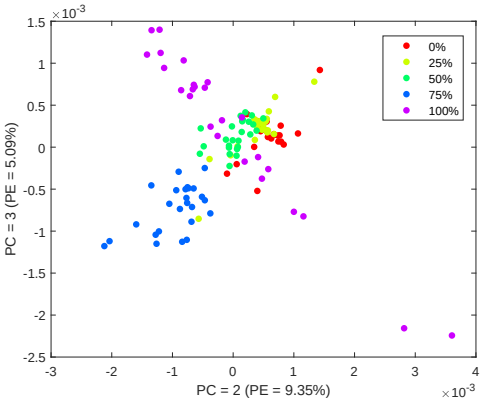

(c)

Figure 3.6: PCA scores plot of different proportions of buffer (0 % buffer to 100 % buffer) in pooled serum (a) PC1 vs PC2, (b) PC1 vs PC3 and (c) PC2 vs PC3.

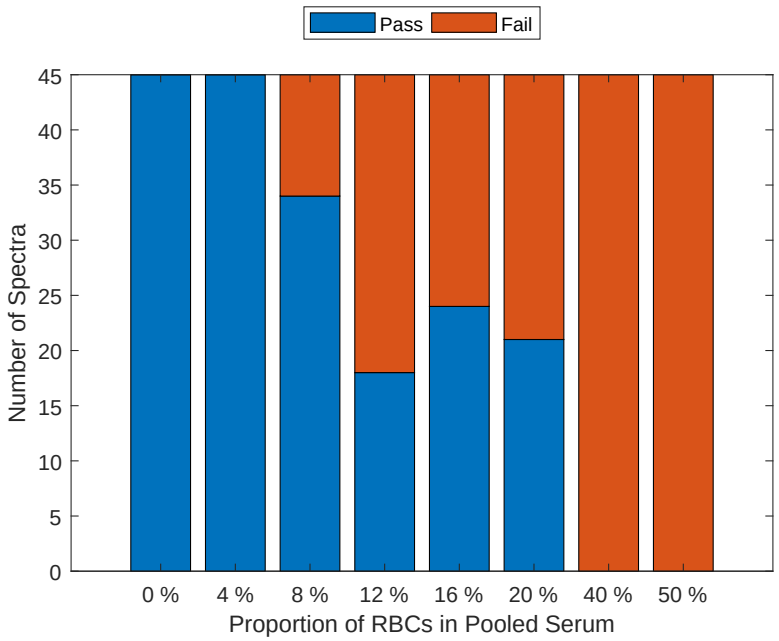

Figure 3.7: Results of quality test on fresh red blood cells

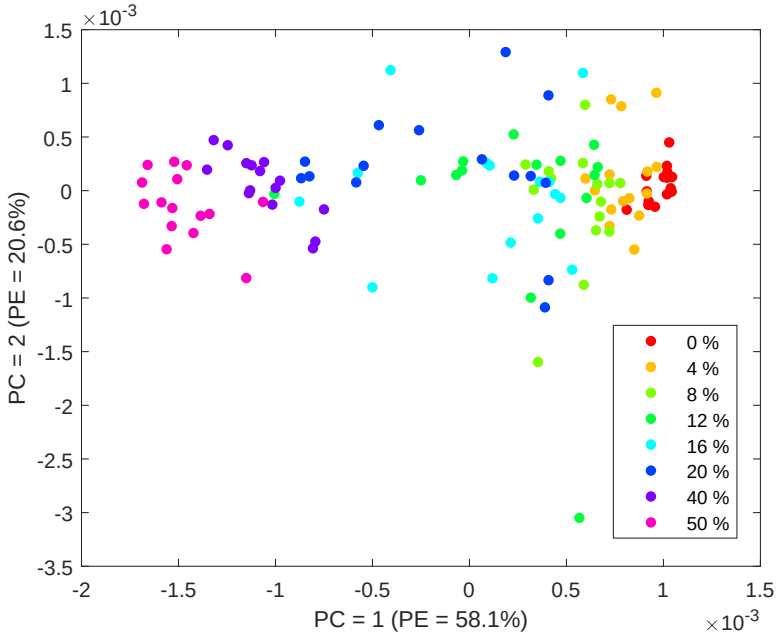

Figure 3.8: PCA scores plot of different proportions of intact RBCs (0% RBCs to 50 % RBCs) in pooled serum PC1 vs PC2.

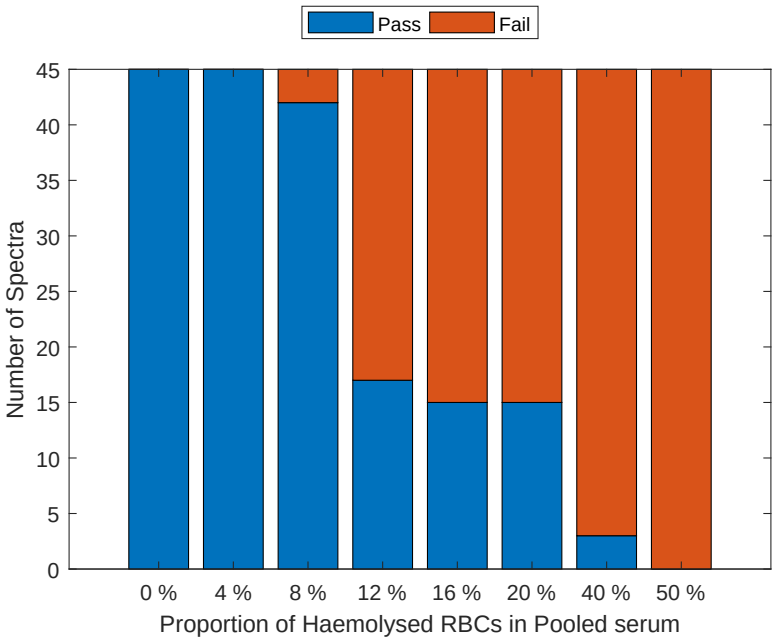

Figure 3.9: Results of quality test on haemolysed RBCs

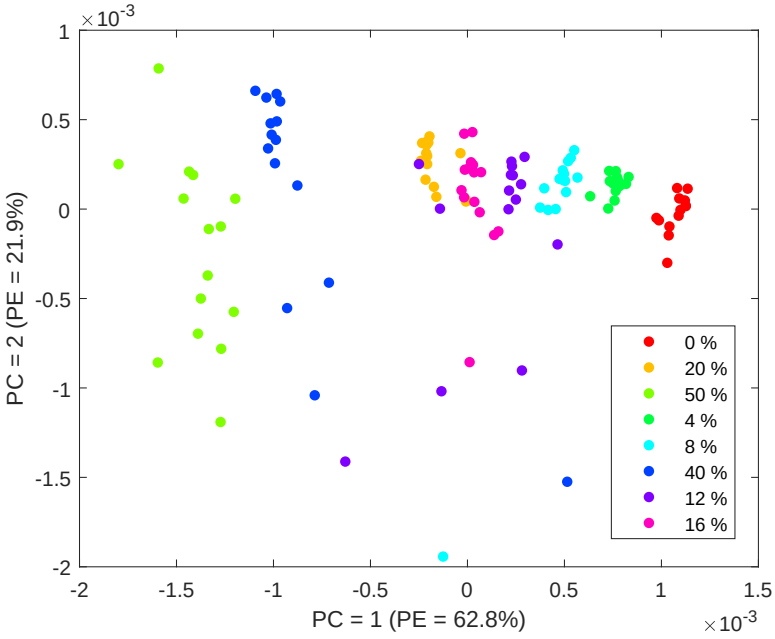

Figure 3.10: PCA scores plot of different proportions of haemolysed RBCs in pooled serum showing PC1 vs PC2

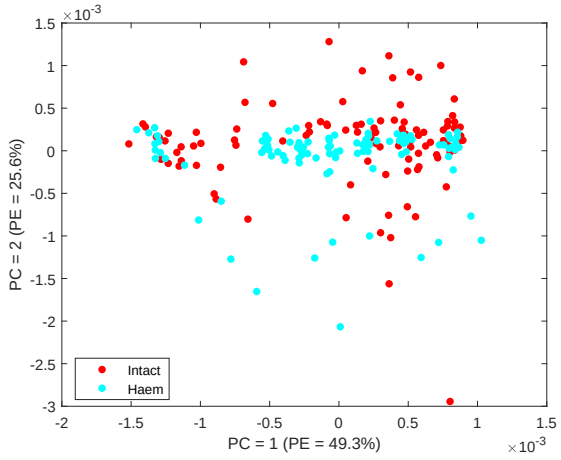

(a)

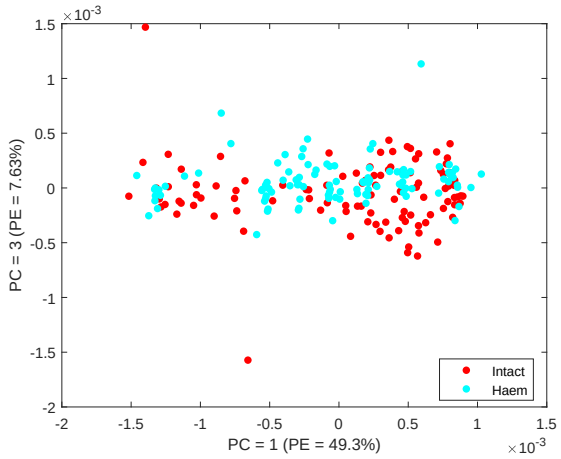

(b)

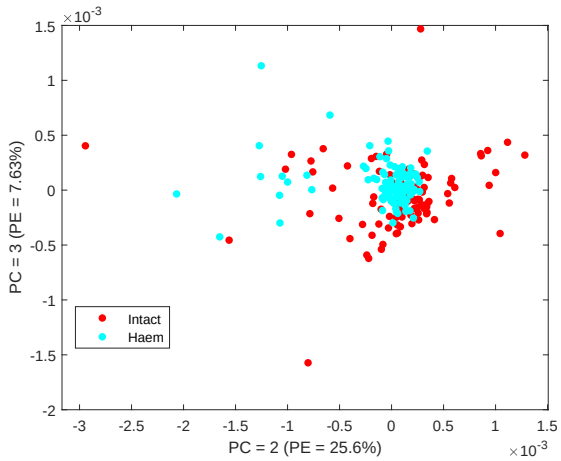

(c)

Figure 3.11: PCA scores plot of intact and haemolysed RBCs in pooled serum (a) PC1 vs PC2, (b) PC1 vs PC3 and (c) PC2 vs PC3.

to some extent PC3 can separate 75% buffer from the remaining (Figure 3.6c). The contamination study of intact RBC (see Figure 3.7) shows the same trend as the dilution study, i.e. reducing the proportion of serum in the sample results in more of the spectra failing the quality test. The PCA scores plot (Figure 3.8) indicates that PC1 indicates well the amount of contamination of the sample, as 0% contamination has the largest PC1 value and increasing contamination systematically reduces the PC1 value. However, there is a lot of overlap between groups, which could be due to the variation in the amount of RBC taken from the packed cell solution. After haemolysis (Figure 3.9) the samples separated in a similar way to intact cells. The PCA scores plot (Figure 3.10) showed the concentrations are found in more defined regions for haemolysed cells compared to intact cells. This may be explained by samples drying more homogeneously as the heterogeneity of the cell structures is lost. Figure 3.11 shows that ATR-FTIR cannot differentiate intact RBC in serum and haemolysed RBC in serum and so the primary separating factor is the percentage concentration of RBCs added.

From these experiments, limits can be established: more than 25% proportion of PBS or 8% cellular contamination in serum results in failure of the quality test. These results can be used as requirements for the serum output; however, a limitation is that there is no justification that this quality test would improve the performance of diagnostic algorithms in detecting disease. Samples used for testing the quality test were not diagnostically relevant, pooled serum and healthy RBCs from a single donor, and therefore the arbitrary quality test criteria values, which were taken from Zhang et al. [2013], will need to be tuned subsequently, using diagnostically relevant samples and diagnostic models.

3.4 Development of a technique to monitor coagulation to form serum

Stage 3 requires the mixing of a reagent with the plasma-like fluid to neutralise the anticoagulants to form serum. In order to validate a numerical model, which would be used as a design tool for developing Stage 3, a method for monitoring the real system was needed. As shown in Section 1.2.2.2, ATR-FTIR spectroscopy has been used to provide 2D images of chemical flows in microfluidic channels and therefore, could possibly be used in this case to monitor the conversion of plasma to serum. This section presents an investigation into the validity of using ATR-FTIR spectroscopy as a tool for monitoring this process.

3.4.1 Horse frozen plasma and serum

Frozen samples of horse plasma and serum were chosen for initial testing as it is cheaper, with no risk of infection, and the traditional method of producing plasma and serum is the same for horses and humans.

3.4.1.1 Material and methods

Pooled horse plasma and pooled horse serum (TCS Biosciences Ltd, Buckingham, UK) were aliquoted into 3 samples each and were stored at -80 °C. Individual samples were defrosted when needed. The Spectrum 2 ATR-FTIR spectrometer (Perkin Elmer, U.S.A) was used in accordance with the method stated in Section 3.2.2.1, and pre-processing and data analysis of the spectra was carried out in accordance with Section 3.2.3.

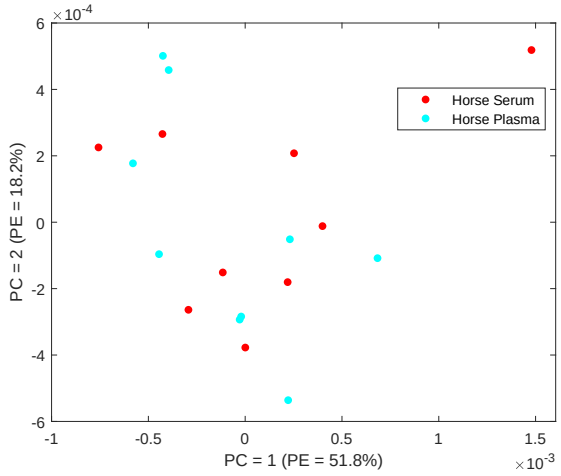

(a)

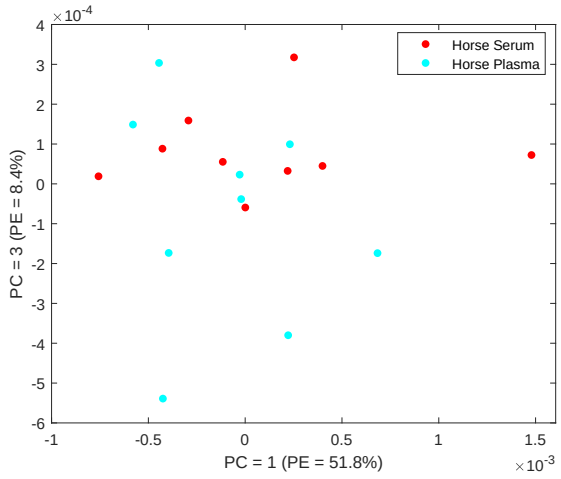

(b)

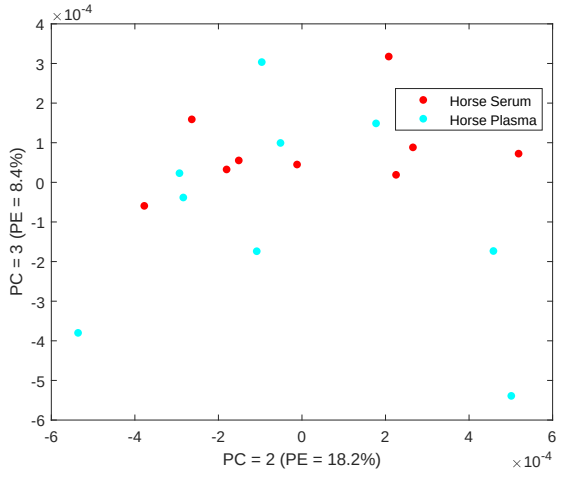

(c)

Figure 3.12: PCA scores plot of horse plasma against horse serum (a)PC1 vs PC2 (b) PC1 vs PC3 and (c) PC2 vs PC3.

3.4.1.2 Results

Figure 3.12 shows that the spectra of horse plasma and serum were indistinguishable when using PCA. On visual inspection, the plasma sample contained a formation of gel like fibers that had formed due to the freezing process [Pieters et al., 2002]. Only the liquid component was analysed: therefore, there was a need to see if the difference between plasma and serum was trapped in the gel. To look into the composition of this gel, 3 samples were collected of the gel and it was analysed according to Section 3.2.2.1.

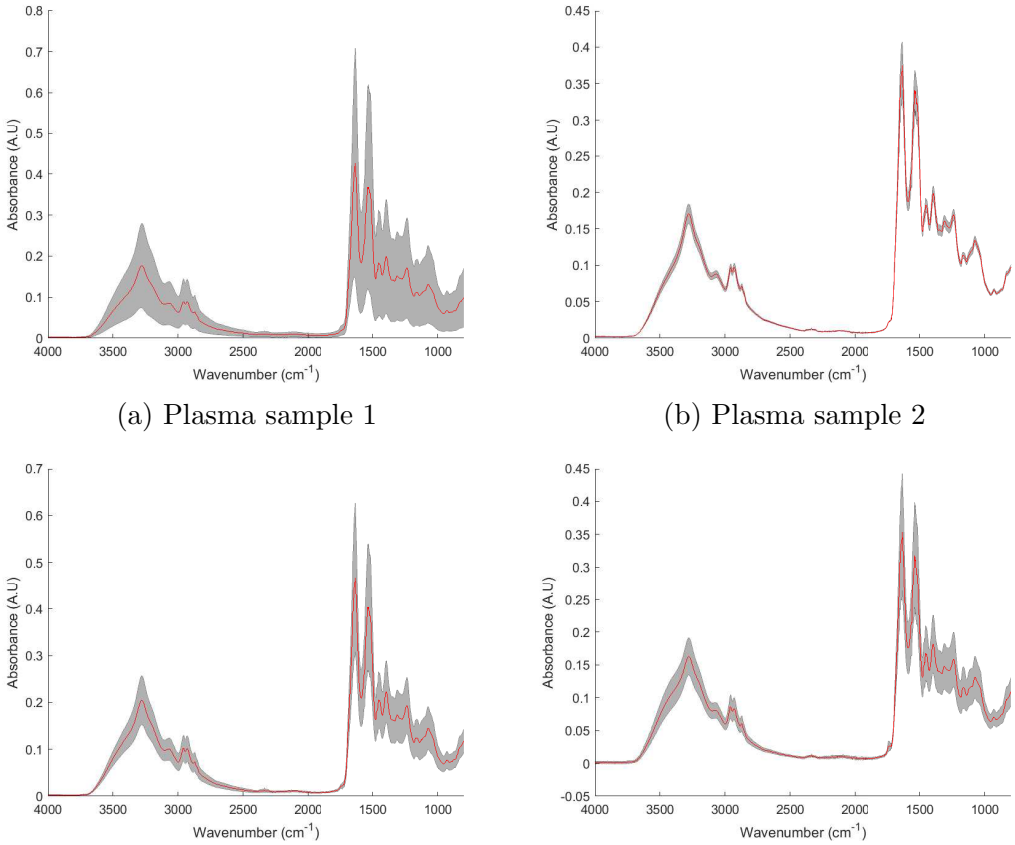

(a) Plasma sample 1

(b) Plasma sample 2

(c) Plasma sample 3

(d) Serum sample

Figure 3.13: Mean spectra (red line) and one standard deviation (SD)(grey band) of horse plasma gel samples (a,b,c) and reference horse serum sample (d).

From the mean sample spectra (Figure 3.13) there is a lot of variation in sam-

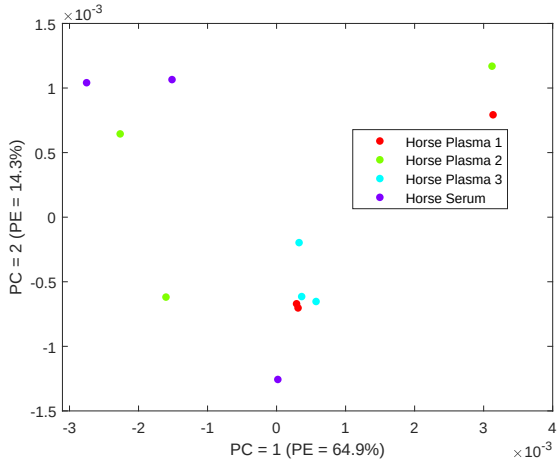

(a)

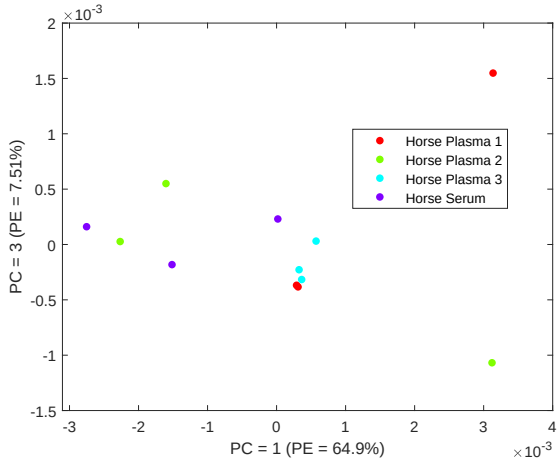

(b)

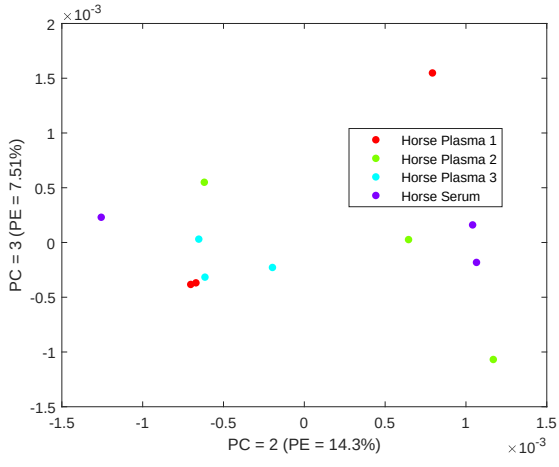

(c)

Figure 3.14: PCA scores plot of the three samples of horse plasma gel and reference horse serum.

ple 1, indicated by the size of the SD band, compared to the other two samples. From the PCA scores plot (Figure 3.14), the composition of the three samples is indistinguishable from the reference horse serum. The gel could be cryoperpitate containing clotting factors, fibrinogen and fibronectin [Droubatchevskaia et al., 2007]. This would prevent coagulation occurring in the bulk material. It was therefore suspected that the variation in the scores plot was attributed to the plasma and serum originating from multiple sources, rather than the difference between plasma and serum. Another factor that needs to be further investigated is the effect of freezing the samples, in order to determine if using frozen samples is suitable analogue for fresh samples.

3.4.2 Coagulation of Horse Plasma

As the differentiation of the samples was achieved in previous experiments, horse blood was acquired with the intention of converting it to plasma and serum and then looking at the difference. The effect of freezing of plasma was first investigated in this section followed by reversing the effect of ethylenediamine tetraacetic acid (EDTA) to trigger coagulation. To reduce biological variation in the samples and attempt to isolate differences due only to freezing, the samples were aliquoted from one source.

3.4.2.1 Material and methods

Horse blood in EDTA (TCS Biosciences Ltd, Buckingham, UK) was introduced into 4 centrifuge tubes, each containing 12 ml. The tubes were centrifuged for 20 minutes at 2250 rpm. Once finished, the plasma was extracted and dispensed into 3 storage tubes (Eppendorphs) per centrifuge tube. Storage tubes from tubes 1 and 3 were placed in the fridge and the remaining tubes placed in the -80 °C freezer overnight. Samples were then left out till they reached room temperature after which spectra were collected according to Section 3.2.2.1. The spectra were

Component	C1	C2	C3	C4	C5	Control
Conc of EDTA testing for (mg/ml)	1.8	1.5	1.4	1.2	1	0
Conc of $CaCl_2$ (mg/ml)	7.2	6	5.6	4.8	4	0

Table 3.1: Preparation of $CaCl_2$ solution.

preprocessed according to Section 3.2.3.

As stated in Section 1.1.5, EDTA is a chelator that scavenges calcium ions: therefore adding an excess of these ions should bind all the EDTA and trigger the coagulation cascade (Figure 1.3).

The horse blood is expected to contain 1.5-1.8 $\mathrm{mg\,ml^{-1}}$ of EDTA, this was assumed to remain consistent in the plasma after the blood underwent centrifugation for calculating amount of calcium ions needed. The effect of adding calcium to the plasma 5 concentrations of EDTA with a control was considered (Table 3.1). Blood was centrifuged and 800 µl of plasma was extracted into storage tubes for the 6 samples. To induce coagulation 200 µl of solution of $CaCl_2$ in distilled water, 4 times the concentration of predicted EDTA concentration, was added to the storage tubes to achieve 1 ml sample (Table 3.1). For the control, only distilled water was added.

3.4.2.2 Results

Figure 3.15 shows that PCA cannot be used to separate ATR-FTIR spectra between plasma stored in the fridge or freezer. Figure 3.16(a),(c) and (e) shows that increasing amounts of $CaCl_2$ has no effect on the spectra as the variation cannot be distinguished by PCA. Figure 3.16 (b), (d) and (f) shows that there is also no difference in the spectra before and after adding the $CaCl_2$.

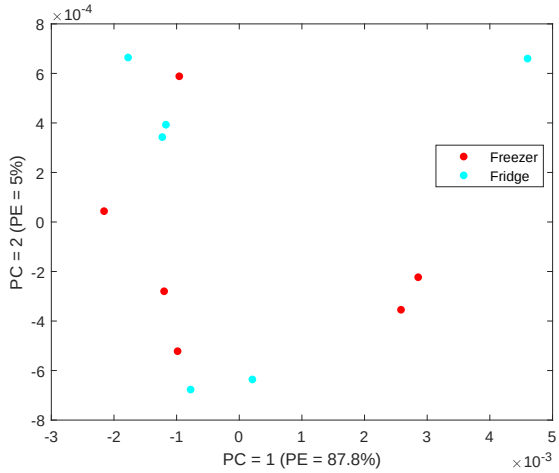

(a)

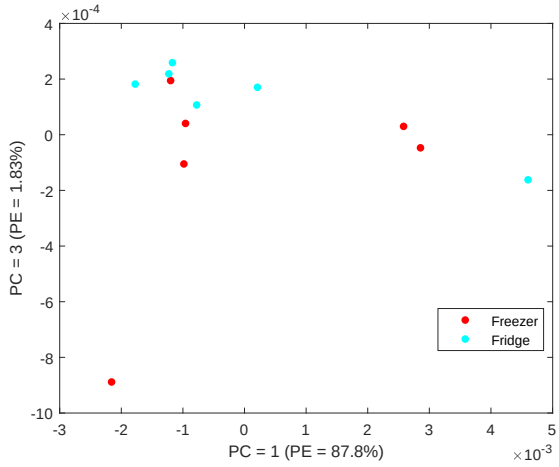

(b)

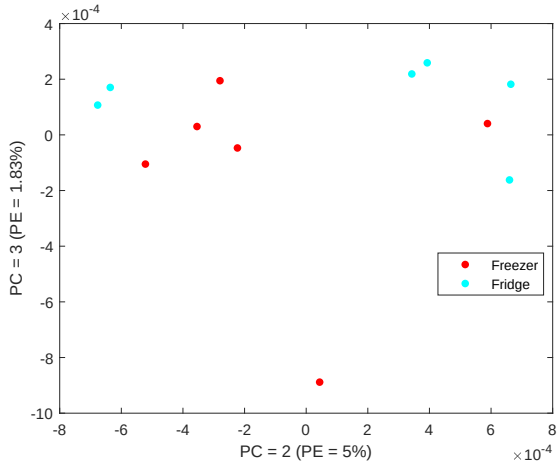

(c)

Figure 3.15: PCA scores plot of horse plasma kept in fridge vs freezer (a) PC1 vs PC2 (b) PC1 vs PC3 and (c)PC2 vs PC3.

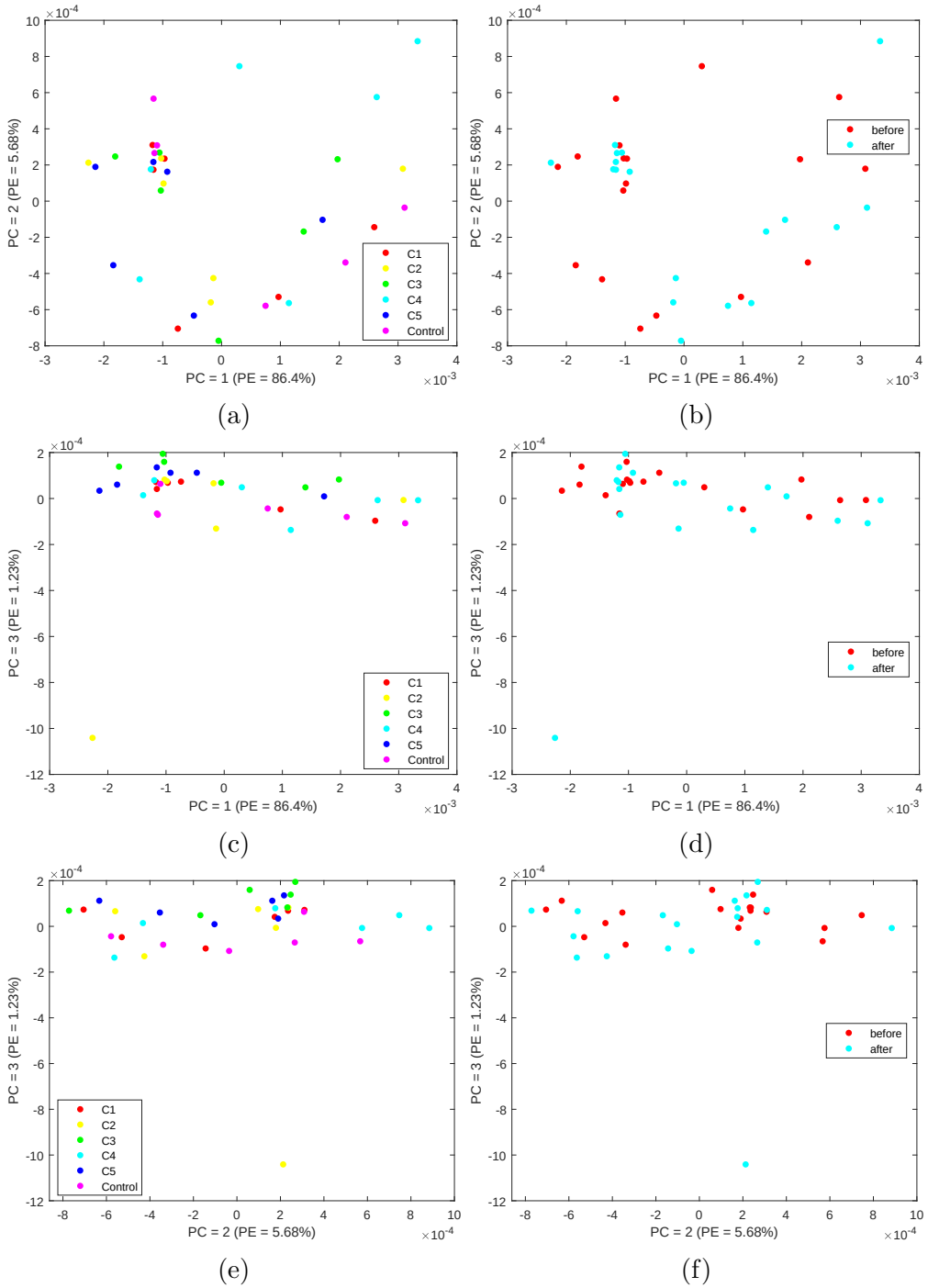

Figure 3.16: PCA scores plot of treating plasma with $CaCl_2$: Showing different concentrations (a) PC1 vs PC2 (c) PC1 vs PC3 (e) PC2 vs PC3. Before and after treatment (b) PC1 vs PC2 (d) PC1 vs PC3 (f) PC2 vs PC3.

3.4.2.3 Discussion

As none of the PCA scores plot in Figure 3.15 show any separation between the samples stored in the fridge and freezer, which suggests that freezing plasma doesn't noticeably affect the spectra. Visually there was no coagulation present after adding $CaCl_2$. Figure 3.16 shows that there is no separation of the spectra of the different concentrations of $CaCl_2$ before and after treatment. It can therefore be said that no reaction occurred and the varying amounts of $CaCl_2$ cannot be detected by ATR-FTIR spectroscopy. However, long term presence of EDTA can damage the coagulation cascade, thereby preventing coagulation in the presence of calcium ions [Colace et al., 2013] and so, if EDTA is used as the anticoagulant for a POC application, the sample will needed to be processed quickly and cannot be stored.

3.5 Testing assumption that ATR-FTIR spectroscopy requires serum for diagnostics

It has been shown by the previous experiments that there are many challenges that need to be overcome in order achieve coagulation for Stage 3 of the design and therefore, it seemed appropriate to question the assumption that ATR-FTIR spectroscopy requires serum to diagnose disease and plasma would not be sufficient. Using plasma would simplify the design and therefore looking at the differences between plasma and serum with respect to ATR-FTIR spectroscopy was investigated.

3.5.1 Human frozen Plasma and Serum

As mentioned in Chapter 1, Biobanks store patient samples for research, with plasma and serum samples from the same patients, so it was decided to use frozen

human samples with disease material to investigate whether serum is required output for the sample preparation device.

3.5.1.1 Material and methods

Paired samples of frozen plasma and serum from 15 cancer and 15 non-cancer donors (Brain Tumour North West Biobank, Royal Preston Hospital NHS Foundation Trust) were stored at -80 °C and individual samples were defrosted when needed. The Spectrum 2 (Perkin Elmer, U.S.A) was used in accordance with the method stated in Section 3.2.2.1. Preprocessing of the spectra was carried out in accordance with Section 3.2.3. Data analysis consisted of individual paired tests between the classes, as shown in Table 3.2, with each combination undergoing PC-DFA.

Table 3.2: Combination of samples for each paired test.

Test	Sample 1	Sample 2
1	Cancer Serum	Cancer Plasma
2	Non-Cancer Serum	Non-Cancer Plasma
3	Cancer Serum	Non-Cancer Serum
4	Cancer Plasma	Non-Cancer Plasma

3.5.1.2 Results: principle component discriminant functional analysis (PC-DFA) analysis on patient plasma and serum samples

Figure 3.17 shows that plasma and serum sample spectra can be separated using PC-DFA in cancer patients but not in non-cancer patients. PC-DFA was not able to separate spectra from cancer and non-cancer samples using either plasma or serum.

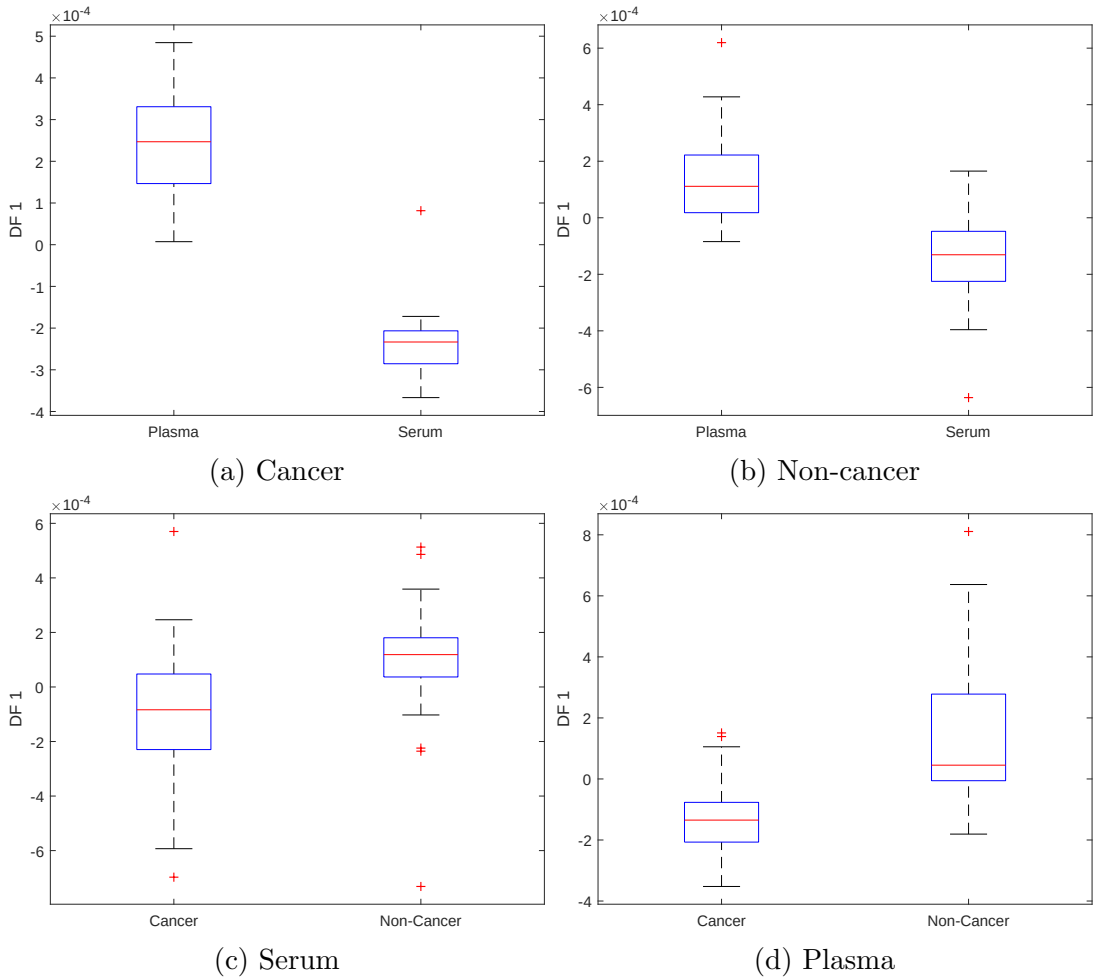

(a) Cancer

(b) Non-cancer

(c) Serum

(d) Plasma

Figure 3.17: PC-DFA scores plot of patient samples: (a) Cancer serum vs cancer plasma (b) Non-cancer serum vs non-cancer plasma, (c) Cancer serum vs non-cancer serum and (d) Cancer plasma vs non-cancer plasma.

3.5.1.3 Discussion

Figure 3.17 shows that serum and plasma can only be separated from cancer patients, as there is no overlap in Figure 3.17(a) compared to Figure 3.17(b,c) and (d). In the PC-DFA plots there are indications of separation but as the ranges in DF1 overlap it is not clear. Due to the sudden availability of the samples, it was not possible to match the demographics between the two groups; cancer and non cancer samples. The mean age and male:female ratio for cancer group are 66.4 and 9:6 compared to 36.2 and 2:13 for non cancer group. This variation in the demographics reduces the robustness of the experiment, and so the findings cannot be used for the development of the microfluidic device. In future a matched patient cohort could be used to improve this experiment's robustness.

3.5.2 Volunteer Human Plasma and Serum Samples

From the previous experiment, the freezing of samples is suspected to damage some proteins in the plasma. Fresh plasma and serum from individuals were collected and analysed on the same day; then the samples were tested after being frozen. This was done to investigate the difference between plasma and serum when fresh and the effect of freezing on the samples.

3.5.2.1 Materials and Method

Four volunteers were recruited to provide blood samples on separate days. Collection was arranged for 9:30am and two blood samples were acquired, one in a serum tube and one in a plasma tube. The tubes were processed by a colleague using the standard method. By noon the samples, 3 aliquots of 500 µl, were ready to be pipetted onto the SIREs and analysed according to method presented in Section 3.2.2.2. Data analysis was carried out according to the method stated in section 3.2.3. The remaining samples were placed in -80 °C freezer and tested

after 1 week.

Table 3.3: Combination of samples for each paired test.

Test	Sample 1	Sample 2
1	Fresh Plasma	Fresh Serum
2	Frozen Plasma	Frozen Serum
3	Fresh Plasma	Frozen Plasma
4	Fresh Serum	Frozen Serum

3.5.2.2 Results: principle component discriminant functional analysis (PC-DFA) analysis on volunteer plasma and serum samples

Figure 3.18 shows the PC-DFA comparison spectra from plasma and serum that were either fresh or frozen. There was no separation between any of the combinations tested.

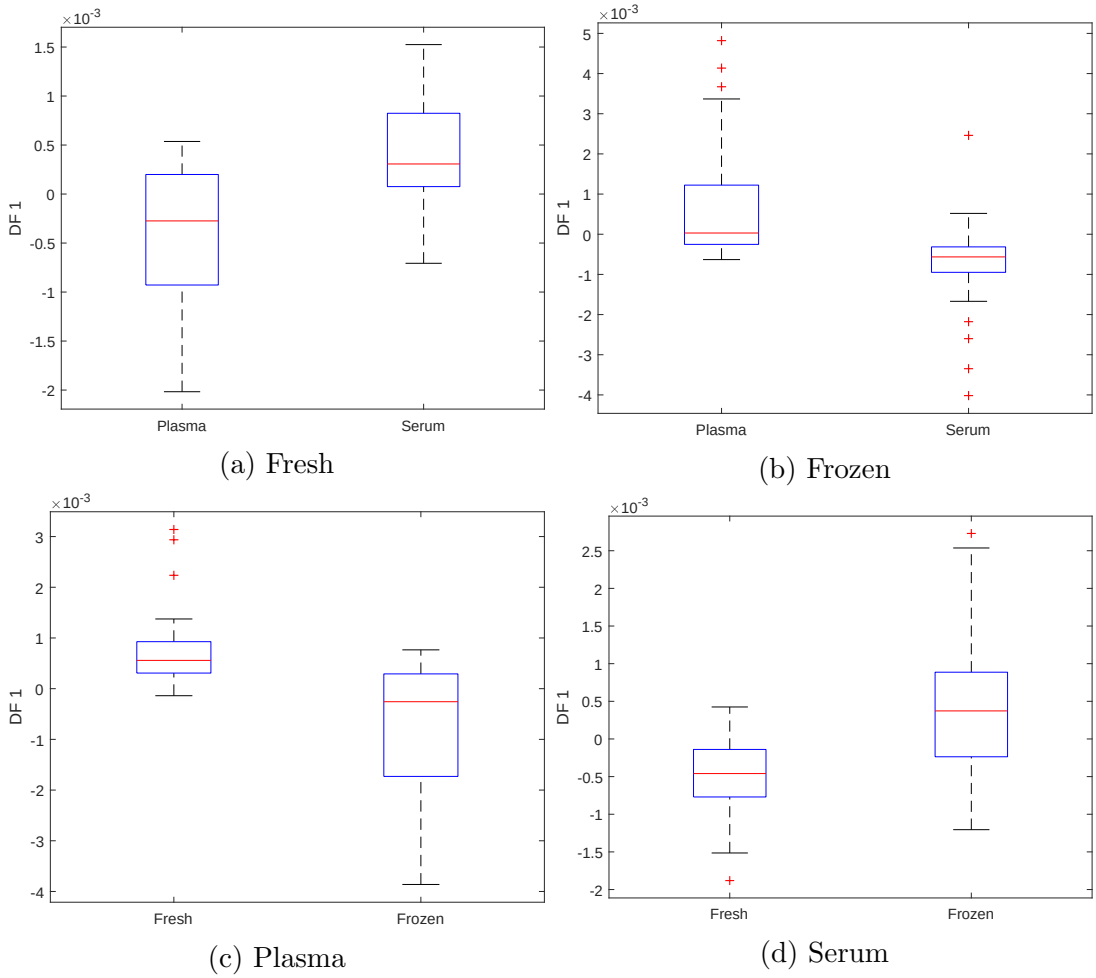

(a) Fresh

(b) Frozen

(c) Plasma

(d) Serum

Figure 3.18: PC-DFA scores plot on volunteer samples: (a) Fresh plasma vs fresh serum (b) Frozen plasma vs frozen serum (c) Fresh plasma vs frozen plasma and (d) Fresh serum vs frozen serum.

3.5.2.3 Discussion

SIREs were adopted for this experiment, as using the method in Section 3.2.2.1 would take a long time to collect fresh samples and this may result in the later samples degrading with time. Using the SIREs results in the batch drying of the samples which stabilises the proteins onto the IRE. The results in Figure 3.18 show that PC-DFA cannot separate any of the paired test categories. This indicates that there is more variation between the volunteers than between the categories, although this can possibly be alleviated with greater volunteer numbers. From the PC-DFA plots, it can be shown that freezing of plasma makes it more variable, as shown by the greater spread in the DF1 in Figure 3.18(c). Figure 3.18(b) shows that frozen serum is more consistent than frozen plasma. It can be concluded that, as there is no difference detected by ATR-FTIR spectroscopy between fresh serum and fresh plasma and that freezing plasma causes more variation. Therefore, in a POC application of ATR-FTIR spectroscopy, using fresh plasma should be sufficient.

3.6 Conclusion

A QT code was successfully developed to indicate sufficiently good quality spectra using 5 criteria; minimum absorbance, 2 signal to noise ratios and 2 signal to water vapour ratios. The criteria values are arbitrarily set and further work has to be carried out to combine the QT code with existing diagnostic models. This is required to prevent the models that are currently developed being limited to the data sets they were developed on. Quality testing allows the monitoring of whether the samples are prepared consistently by different users and therefore, produce valid test results.

EDTA is known to cause permanent damage to coagulation pathways. Therefore, if serum is needed citrate should be used as the anticoagulant as it has been

shown to be reversible in the short term [Lehmann et al., 2015]. The effect of the anticoagulant citrate on serum spectra should also be investigated. As ATR-FTIR spectroscopy is not able to identify individual components in a mixture, it cannot be used as a way of monitoring coagulation in a microfluidic device.

ATR-FTIR spectroscopy also cannot differentiate between plasma and serum in pooled samples as well as non-diseased volunteers. It has been shown that serum is more stable for freezing than plasma. Therefore, it should be taken to central labs for testing. For a POC device there is no evidence to suggest that serum is needed and therefore plasma can be used for quick testing but cannot be used after long term storage. Learning that serum is not a requirement for ATR-FTIR spectroscopy, significantly simplifies the device as Stage 3 is not required, thereby reducing the need to investigate further the coagulation process to form serum at the microfluidic scale. Consequently, the next chapter, Chapter 4, will investigate how to prepare plasma from whole blood while collecting the diagnostically important cells as stated in Stage 1 of the design (see Section 2.4.3.1).

3.7 References

Biospec [2018], 'Cluster-Toolbox-v2.0'.
URL: *https://github.com/Biospec/cluster-toolbox-v2.0*

Colace, T. V., Tormoen, G. W., McCarty, O. J. and Diamond, S. L. [2013], 'Microfluidics and coagulation biology', *Annual review of biomedical engineering* **15**, 283–303.

Droubatchevskaia, N., Wong, M. P., Chipperfield, K. M., Wadsworth, L. D. and Ferguson, D. J. [2007], 'Guidelines for cryoprecipitate transfusion', *British Columbia Medical Journal* **49**(8), 441.

Gromski, P. S., Muhamadali, H., Ellis, D. I., Xu, Y., Correa, E., Turner, M. L. and Goodacre, R. [2015], 'A tutorial review: Metabolomics and partial least squares-discriminant analysis–a marriage of convenience or a shotgun wedding', *Analytica chimica acta* **879**, 10–23.

Hands, J. R., Dorling, K. M., Abel, P., Ashton, K. M., Brodbelt, A., Davis, C., Dawson, T., Jenkinson, M. D., Lea, R. W., Walker, C. et al. [2014], 'Attenuated total reflection fourier transform infrared (atr-ftir) spectral discrimination of brain tumour severity from serum samples', *Journal of biophotonics* **7**(3-4), 189–199.

Lehmann, M., Wallbank, A. M., Dennis, K. A., Wufsus, A. R., Davis, K. M., Rana, K. and Neeves, K. B. [2015], 'On-chip recalcification of citrated whole blood using a microfluidic herringbone mixer', *Biomicrofluidics* **9**(6), 064106.

Pieters, M., Jerling, J. C. and Weisel, J. W. [2002], 'Effect of freeze-drying, freezing and frozen storage of blood plasma on fibrin network characteristics', *Thrombosis research* **107**(5), 263–269.

Zhang, X., Thiéfin, G., Gobinet, C., Untereiner, V., Taleb, I., Bernard-Chabert, B., Heurgué, A., Truntzer, C., Ducoroy, P., Hillon, P. et al. [2013], 'Profiling serologic biomarkers in cirrhotic patients via high-throughput fourier transform infrared spectroscopy: toward a new diagnostic tool of hepatocellular carcinoma', *Translational Research* **162**(5), 279–286.

Chapter 4: Developing a numerical model for designing Stage 1

4.1 Introduction

Numerical modelling is a useful tool in the design process, as it is can be used to test design changes virtually rather than needing to build prototype devices for each change, which as shown in Chapter 2 can be costly and slow. In order for this tool to be valid, a virtual system that sufficiently represents the actual system, blood flowing through microfluidic channel, is needed for testing. The complete mathematical modelling of blood flow is a multiscale problem involving the molecular scale, the mesoscale and the continuum scale [Fedosov et al., 2014]. Molecular scale methods, such as Molecular Dynamics, can theoretically model effects such as the Fåhræus-Lindqvist (FL) effect but are very demanding computationally [Li et al., 2018; Tang et al., 2017]. Scaling the molecular interactions to the required length scale and number of red blood cells (RBCs) involves unpractically large computational cost for most RBCs flow problems. Mesoscale models simplify the microscale models by making the "particles" represent a small volume of blood instead of individual molecules. These methods, such as dissipative particle dynamics (DPD) and smoothed particle hydrodynamics (SPH), discretise the domain into clusters of particles with a cluster type for each component [Ye et al., 2016]. Each cluster moves in accordance with the net force it experiences from surrounding groups of particles. For DPD these forces are determined from a set of arbitrary model parameters and for SPH they are a result of discretising the Navier-Stokes equations. The Lattice Boltzmann method (LBM), unlike DPD and SPH, is a hybrid mesh-particle method [Schiller et al., 2018]. The particle motion is governed by the Lattice Boltzman equation

over a discrete lattice mesh and the immersed boundary method is commonly used to model the fluid-RBC interaction. The main limitation of mesoscale scale models is they also have a high computational cost, which has restricted their use in industry and as a design tool.

Continuum models solve the Navier-Stokes equation modified with a non-linear viscosity term, which accounts for blood being a homogeneous non-Newtonian fluid. The shear thinning behaviour of blood is often modelled by empirically derived viscosity expressions such as a power-law relationship, the Carreau-Yassuda viscosity and others [Campo-Deaño et al., 2015; Johnston et al., 2004]. These models capture flow behaviour in large vessel diameters, but are not valid when the cell and flow length scales become comparable such as in micron-scale channels, where the fluid heterogeneity becomes important.

Mixture theory (the theory of interacting continua) is an alternative continuum theory and was developed to take into account the heterogeneity of the suspension [Kim et al., 2016]. In these models there are two superimposed continua, where one represents the fluid phase and the other the particle (cell) phase. For example the continuum effective medium (CEM) model, developed by Ley and Bruus [2016], uses mixture theory to simulate the migration of RBC in response to external force in a microfluidic device. The model simplifies the hydrodynamic particle interactions by making the effective suspension viscosity, particle diffusivity and motility functions of local particle concentration. The resulting model has a significantly lower computational cost than the mesoscale models. These models can be implemented in a commercially available finite element analysis (FEA) software such as COMSOL Multiphysics (COMSOL inc., Burlington, U.S.A.), which is widely used in the medical device and bioengineering industry.

The aim of the work, presented in this chapter, is to develop a phenomenological CEM model that allows the separation of healthy RBCs from whole blood in microfluidic channels, based on the FL effect. We use COMSOL to implement the

model as it has a simple workflow, user interface, with built in partial differential equation (PDE) function so coding is not required for running the simulation.

4.2 Model formulation

We will model the suspension of blood as a compressible single phase fluid based on the CEM model developed by Ley and Bruus [2016]. The CEM model consists of modified Navier-Stokes momentum equations, for non-newtonian fluid, and continuity equation coupled with a PDE that determines the local concentration of particles. This local concentration affects properties, such as the viscosity of the fluid, resulting in local variations in viscosity. The Ley and Bruus [2016] model used a single particle force to induce RBC migration due to an acoustic or magnetic field. However, here we will create a migration force that is a function of the shear gradient, in order to represent the formation of the cell-free layer (CFL). The derivation of the model is given in the next section.

4.2.1 Governing equations

The Navier-Stokes momentum equation is given as:

$$\rho(\phi)\frac{\partial \boldsymbol{u}}{\partial t} + \rho(\phi)(\boldsymbol{u}\cdot\nabla)\boldsymbol{u} = -\nabla p + \mu(\phi)\nabla^2\boldsymbol{u}, \tag{4.1}$$

where $\boldsymbol{u}$ is the velocity vector, $\rho(\phi)$ is the density of the suspension, and is assumed to be a function of the volume fraction, ϕ, so that $\rho(\phi) = (1-\phi)\rho_w + \rho_p\phi$ with ρ_p being the particle density and ρ_w the background fluid density. The volume fraction is related to the particle concentration, c by $\phi = \frac{4}{3}\pi a^3 c$, where a is the particle radius. In equation (4.1) t is time, $\nabla = \left(\frac{d}{dx}, \frac{d}{dy}, \frac{d}{dz}\right)$, p is pressure and $\mu(\phi)$ is the fluid viscosity, which is also assumed to be a function of the

volume fraction. The continuity equation is given as

$$\frac{\partial \rho(\phi)}{\partial t} + \nabla \cdot (\rho(\phi)\boldsymbol{u}) = 0. \tag{4.2}$$

As is standard in mathematical modelling, we will non-dimensionalise the governing equations to reduce the number of parameters required. Here we non-dimensionalise the variables as

$$\bar{\boldsymbol{u}} = \frac{\boldsymbol{u}}{U},\ \bar{x} = \frac{x}{W},\ \bar{y} = \frac{y}{W},\ \bar{t} = \frac{U}{W}t,\ \bar{\rho} = \frac{\rho}{\rho_w},\ \bar{p} = \frac{p}{U^2\rho_w},\ \bar{\mu} = \frac{\mu}{\mu_w}, \tag{4.3}$$

where U is a velocity scalar, such as the average velocity of fluid; W is a typical channel length scale, such as the width of the channel; ρ_w and μ_w are the density and viscosity of the continuous fluid phase respectively. The momentum equation in dimensionless form is then

$$\bar{\rho}(\phi)\frac{\partial \bar{\boldsymbol{u}}}{\partial \bar{t}} + \bar{\rho}(\phi)(\bar{\boldsymbol{u}} \cdot \nabla)\bar{\boldsymbol{u}} = -\nabla \bar{p} + \frac{1}{Re_w}\bar{\mu}(\phi)\nabla^2 \bar{\boldsymbol{u}}, \tag{4.4}$$

where $\bar{\rho}(\phi) = (1-\phi) + \frac{\rho_p}{\rho_w}\phi$; and Re_w is the Reynolds number for the fluid phase ($Re_w = \frac{UW\rho_w}{\mu_w}$). After nondimensionalising, the continuity equation then becomes

$$\frac{\partial \bar{\rho}(\phi)}{\partial \bar{t}} = -\nabla \cdot (\bar{\rho}(\phi)\bar{\boldsymbol{u}}). \tag{4.5}$$

4.2.2 Derivation of the concentration equation

The local volume fraction or the particle concentration is governed by the interactions between particle diffusion, advection, and migration which includes particle-particle interaction,

$$\frac{\partial \phi}{\partial t} = \nabla \cdot \left[J_{\text{diff}} + J_{\text{adv}} + J_{\text{mig}} \right]. \tag{4.6}$$

The flux of each component, diffusion (J_{diff}), advection (J_{adv}), migration (J_{mig}), is dependent on the local concentration and for the migration, a phenomenological force, F_{mig}, will be used. The governing equation for the concentration is taken as

$$\frac{\partial c}{\partial t} = \nabla \cdot \left[D(c)\nabla c - c\boldsymbol{u} - c\nu(c)F_{\text{mig}} \right], \tag{4.7}$$

where $D(c) = D_0 D(\phi)$ and $\nu(c) = \nu_0 \nu(\phi)$ are the effective particle diffusivity and mobility respectively [Ladd, 1990]. The hydrodynamic transport coefficients, the particle diffusivity, $D(\phi)$, particle motility, and $\nu(\phi)$, are used as correction functions for the diffusivity constant $D_0 = k_B T_c \nu_0$, where k_B is the Boltzmann constant, T_c is the temperature, and $\nu_0 = 1/(6\pi\mu_w a)$ is the dilute-limit motility constant. Ladd [1990] calculated these coefficients, as well as the viscosity needed in the momentum equation (4.1) for high density suspensions of rigid particles,

$$\begin{aligned}
\bar{\mu}(\phi) &= (2 + 2.476\phi + 7.53\phi^2 - 16.34\phi^3 + 83.7\phi^4), \\
D(\phi) &= (1 + 1.714\phi + 6.906\phi^2 - 17.05\phi^3 + 61.2\phi^4)^{-1}, \\
\nu(\phi) &= (1 + 5.55\phi + 43.4\phi^2 - 149.6\phi^3 + 562\phi^4)^{-1}.
\end{aligned}$$

As the transport coefficients equations are in terms of ϕ the concentration equation can be written as

$$\frac{\partial c}{\partial t} = \nabla \cdot \left[D(\phi)D_0\nabla c - c\boldsymbol{u} - c\nu_0\nu(\phi)F_{\text{mig}} \right]. \tag{4.8}$$

Non-dimensionalising the concentration equation (4.8) using $c = C\bar{c}$, where C is the average sample concentration, results in

$$\frac{CU}{W}\frac{\partial \bar{c}}{\partial \bar{t}} = \frac{1}{W}\nabla \cdot \left[D_0 D(\phi) C\nabla\bar{c} - CU\bar{c}\bar{\boldsymbol{u}} - C\bar{c}\nu_0\nu(\phi)F_{\text{mig}} \right]. \tag{4.9}$$

As mentioned previously, the migration force, F_{mig}, is known to be related to the shear rate. In this model we couple the migration force to the shear rate term, $\dot{\boldsymbol{\gamma}}$, by,

$$F_{mig} = C_{mig}(\dot{\boldsymbol{\gamma}})^b \tag{4.10}$$

where $\dot{\gamma} = \sqrt{(\frac{1}{2}\mathcal{D} : \mathcal{D})}$ is the magnitude of the shear-rate tensor with rate of deformation tensor $\mathcal{D} = (\nabla \boldsymbol{u} + (\nabla \boldsymbol{u})^T)$, C_{mig} is the coefficient of migration and b is a shear exponent, both of which will need to be experimentally determined. Substituting the migration force (4.10) into the concentration equation (4.9) results in

$$\frac{\partial \bar{c}}{\partial \bar{t}} = \nabla \cdot \left[\frac{1}{Pe} D(\phi) \nabla \bar{c} - \bar{c}\bar{\boldsymbol{u}} - St\, \bar{c}\, \nu(\phi)(\dot{\boldsymbol{\gamma}})^b \right], \tag{4.11}$$

where the Peclet number, Pe, which is the ratio of rate advection by the flow to diffusion, and the Stouhal number, St, which is the ratio of inertial forces due to the unsteadiness of the flow, are given by

$$Pe = \frac{WU}{D_0}$$

and

$$St = \frac{U^{b-1}}{W^b} \nu_0 C_{mig}.$$

4.2.3 Continuum effective medium (CEM) Model summary

A summary of the mathematical model equations to be solved is presented below. The governing equations for momentum, continuity and concentration are

$$\bar{\rho}(\phi) \frac{\partial \bar{\boldsymbol{u}}}{\partial \bar{t}} + \bar{\rho}(\phi)(\bar{\boldsymbol{u}} \cdot \nabla)\bar{\boldsymbol{u}} = -\nabla \bar{p} + \frac{1}{Re_w} \bar{\mu}(\phi) \nabla^2 \bar{\boldsymbol{u}}, \tag{4.12}$$

$$\frac{\partial \bar{\rho}(\phi)}{\partial \bar{t}} = -\nabla \cdot (\bar{\rho}(\phi)\bar{\boldsymbol{u}}) \tag{4.13}$$

and

$$\frac{\partial \bar{c}}{\partial \bar{t}} = \nabla \cdot \left[\frac{1}{Pe} D(\phi) \nabla \bar{c} - \bar{c}\bar{\boldsymbol{u}} - St\, \bar{c}\, \nu(\phi) (\dot{\boldsymbol{\gamma}})^b \right], \tag{4.14}$$

where ϕ is the volume fraction and $\bar{c}$ local particle concentration, such that $\phi = \frac{4}{3}\pi a^3 C \bar{c}$. The constitutive equations for density, $\bar{\rho}(\phi)$, viscosity, $\bar{\mu}(\phi)$, diffusivity, $D(\phi)$, and motility, $\nu(\phi)$, are

$$\begin{aligned}
\bar{\rho}(\phi) &= (1-\phi) + \frac{\rho_p}{\rho_w}\phi, \\
\bar{\mu}(\phi) &= (2 + 2.476\phi + 7.53\phi^2 - 16.34\phi^3 + 83.7\phi^4), \\
D(\phi) &= (1 + 1.714\phi + 6.906\phi^2 - 17.05\phi^3 + 61.2\phi^4)^{-1}, \\
\nu(\phi) &= (1 + 5.55\phi + 43.4\phi^2 - 149.6\phi^3 + 562\phi^4)^{-1},
\end{aligned}$$

and the model parameters are given in the following tables: Table 4.1, Table 4.2 and the simulation outputs given in Table 4.3.

Table 4.1: Input parameters

Parameter	Definition
W	Channel width
H	Channel height
a	Particle radius
ρ_p	Density of particles
ρ_w	Density of fluid phase
μ_w	Viscosity of fluid phase
k_B	Boltzmann constant
T_c	Temperature
C_{mig}	Coefficient of migration
b	Shear exponent
Q	Volumetric flow rate

Table 4.2: Derived and dimensionless parameters

Parameter	Expression	Definition
D_0	$k_B T_c \nu_0$	Diffusivity constant
ν_0	$\frac{1}{6\pi\mu_w a}$	Dilute-limit motility constant
U	$\frac{Q}{WH}$	Average fluid velocity
Re	$\frac{UW\rho_w}{\mu_w}$	Reynolds number
Pe	$\frac{WU}{D_0}$	Peclet Number
St	$\frac{U^{b-1}}{W^b}\nu_0 C_{mig}$	Strouhal Number

Table 4.3: Outputs of simulation

Output variable	Definition
$\bar{\boldsymbol{u}}$	Non-dimensional velocity
$\bar{p}$	Non-dimensional pressure
$\bar{c}$	Non-dimensional particle concentration
ϕ	Volume fraction

4.2.4 Numerical methodology: using COMSOL

As stated earlier, COMSOL multiphysics is a FEA software that is used in this chapter to implement the CEM model. The geometry was created in a simple computer aided design (CAD) interface, then the material parameters and the equations were inserted as coefficients of a generic set of fluid PDEs into the software. No actual coding is required unlike in other software such as openFoam. The boundary conditions for flow were set to be no-slip and non penetration, so that there is no fluid velocity at the wall. The inlet was prescribed with a parabolic flow profile and at the outlet a zero pressure condition was set to simulate no resistance. For the concentration equation, a no flux condition was used at the walls, the inlet condition was set to a fixed particle concentration and a normal flux condition prescribed at the outlet. Once the system of equations are set up, the mesh was generated and the simulation was run by using the user interface. COMSOL can do post-processing such as producing graphs and vector plots but it can also be interfaced with Matlab (Mathworks, Natick, U.S.A) to allow for more bespoke data post-processing.

4.3 Comparison of the continuum effective medium (CEM) model with the Carreau viscosity model

To investigate how the CEM model compares to a standard model that is frequently used to model blood flow, we considered a one-dimensional steady flow problem and compared it with the classical Carreau-Yassuda viscosity model, presented in Yasuda et al. [1981], often used to model the shear-thinning behaviour of blood [Johnston et al., 2004].

4.3.1 Continuum effective medium (CEM) model

1D steady compressible flow

In steady one-dimensional flow we have the channel orientated so that the boundaries of the channel are at $y = \pm\frac{W}{2}$ with the flow in the x-direction. The momentum equation (4.12) simplifies to

$$0 = -\frac{\partial \bar{p}}{\partial x} + \frac{1}{Re_w}\frac{d}{dy}\left(\bar{\mu}(\phi)\frac{d\bar{u}}{dy}\right), \tag{4.15}$$

the continuity equation (4.13) to

$$0 = -\frac{d}{dx}(\bar{\rho}(\phi)\bar{u}), \tag{4.16}$$

and the concentration equation (4.14) to

$$0 = \frac{d}{dy}\left[\frac{1}{Pe}D(\phi)\frac{d\bar{c}}{dy} - St\,\bar{c}\,\nu(\phi)\Big(\frac{d\bar{u}}{dy}\Big)^b\right]. \tag{4.17}$$

Solving the momentum equation (4.15), subject to the no slip boundary condition, gives

$$\frac{d\bar{u}}{dy} = \frac{Re_w}{\mu(\phi)}\frac{\Delta\bar{P}}{W}y, \tag{4.18}$$

where we have set $\frac{\partial \bar{p}}{\partial x} = \frac{\Delta\bar{P}}{W}$ as the pressure gradient, so that the concentration equation can be reduced to

$$0 = \frac{d}{dy}\left[\frac{1}{Pe}D(\phi)\frac{d\bar{c}}{dy} - St\bar{c}\nu(\phi)\left(\frac{Re_w}{\mu(\phi)}\frac{\Delta\bar{P}}{W}y\right)^b\right]. \tag{4.19}$$

To maintain the current directionality of the migration force, $du/dy < 0$ when $y > 0$ and $du/dy > 0$ when $y > 0$, we need to specify

$$y^b = \mathrm{sgn}(y)(|y|)^b. \tag{4.20}$$

The concentration equation (4.19) can therefore be simplified to

$$0 = \frac{d}{dy}\left[\frac{d\phi}{dy} + \mathrm{sgn}(y) A \left(|y|\right)^b \phi\right], \tag{4.21}$$

where

$$A = \frac{PeSt\nu(\phi)}{D(\phi)} \left|\frac{Re_w}{\mu(\phi)} \frac{\Delta \bar{P}}{W}\right|^b. \tag{4.22}$$

4.3.2 Carreau viscosity model

To model a shear-rate dependent viscosity, we consider a Carreau-Yassuda constitutive equation

$$\mu_{CAR} = \left(\frac{1}{\mu_w}\right)\left(\mu_{inf} + (\mu_0 - \mu_{inf})\left(1 + \left(\lambda \frac{du}{dy}\right)^a\right)\right)^{\left(\frac{n-1}{a}\right)} \tag{4.23}$$

where μ_0 and μ_{inf} are the zero shear rate viscosity and infinite shear rate viscosity respectively. The material constants λ and n are standard values that have been empirically derived by fitting a power law curve to experimental data [Johnston et al., 2004]. For the comparison with our CEM model, we set $a = 2$ so that the viscosity model reduces to the Carreau model widely used to model blood rheology [Cho and Kensey, 1991].

4.3.3 Numerical methodology

COMSOL with Matlab was used to implement the one-dimensional governing equations for both the CEM model and the Carreau model. The CEM model parameters domain space, that were simulated are 10 logarithmically spaced values from 1×10^{-20} to 1×10^{-18} for C_{mig} with b from 1 to 1.9 in steps of 0.1 for each value of C_{mig}. To implement the one-dimensional CEM model, an algorithm was created to numerically ascertain the pressure, ΔP, required for each combination of C_{mig} and b to achieve the correct flow rate (see Appendix A). The parameter

Table 4.4: Parameters used for (a) CEM model and (b) Carreau model [Johnston et al., 2004]

Parameter	Value	Description
C_{mig}	$1\times10^{-20} - 1 \times 10^{-18}$	Coefficient of migration
b	1-1.9	Shear exponent
Re	6.35	Reynolds number
Pe	1.43	Peclet number

(a)

Parameter	Value	Description
λ	3.313	Relaxation time (s)
n	0.36	Power index
μ_0	0.056	Zero shear viscosity
μ_{inf}	0.0035	Infinite shear viscosity

(b)

range and values are shown in Table 4.4a. This pressure was fed back into the model and the velocity profile was extracted. The same flow conditions were used in the Carreau model and the velocity profile was extracted, with model parameters shown in Table 4.4b. The overall relative error was then calculated using

$$RE = \frac{\int |u_{CEM}(y) - u_{CAR}(y)|\, dy}{\int u_{CAR}(y) dy}, \tag{4.24}$$

where u_{CEM} and u_{CAR} are the velocity of the fluid in the CEM model and Carreau model respectively. The b value with the minimum relative error for each C_{mig} value and the C_{mig} value with the minimum relative error for each b were recorded. The velocity profile of the CEM model for these values with the velocity profile of the Carreau model are shown in Figures 4.2a and 4.3a. The corresponding particle distribution of the CEM model are presented in Figures 4.2b and 4.3b.

4.3.4 Results and Discussion

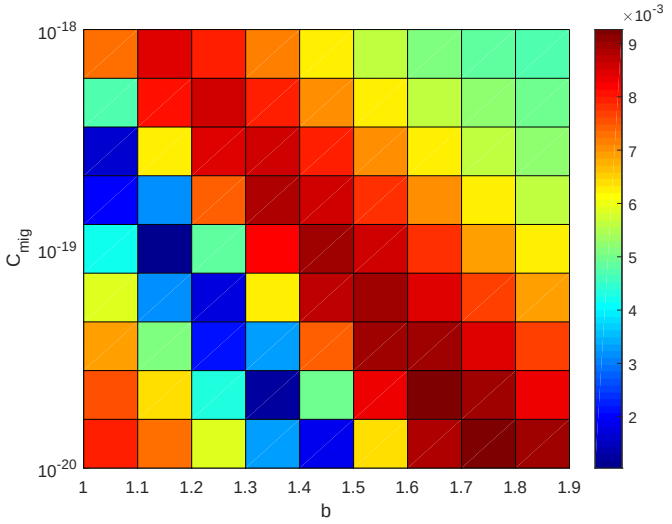

Figure 4.1: The overall relative error between CEM and Carreau model velocity profiles.

The overall relative error, calculated using equation (4.24), between the velocity profiles of the Carreau model and the CEM model is shown in Figure 4.1. The domain can be split into three regions; high error (red) along the diagonal, very low error (dark blue) line and low error for high C_{mig} and b values (green). The minimum relative error (1×10^{-3}) is found when $C_{\text{mig}} = 7.7426 \times 10^{-20}$ and $b = 1.1$. For each value of C_{mig} the velocity profiles, with the minimum relative error between the CEM and the Carreau models, as well as the Carreau velocity profile is presented in Figure 4.2a. The corresponding particle distribution is presented in Figure 4.2b. The minimum relative error along the other axis of Figure 4.1 was also investigated. The velocity profiles for each value of b is shown in Figure 4.3a and corresponding particle distributions is shown in Figure 4.3b.

The combination of C_{mig} and b in the dark blue region produces a close approximation to the Carreau model velocity profile (Figure 4.2a and 4.3a) but fails to produce a CFL (Figure 4.2b and 4.3b). The minimum error combination in the high C_{mig} and b region produced a plug flow velocity profile (Figure 4.2a and

4.3. Comparison of the continuum effective medium (CEM) model with the Carreau viscosity model

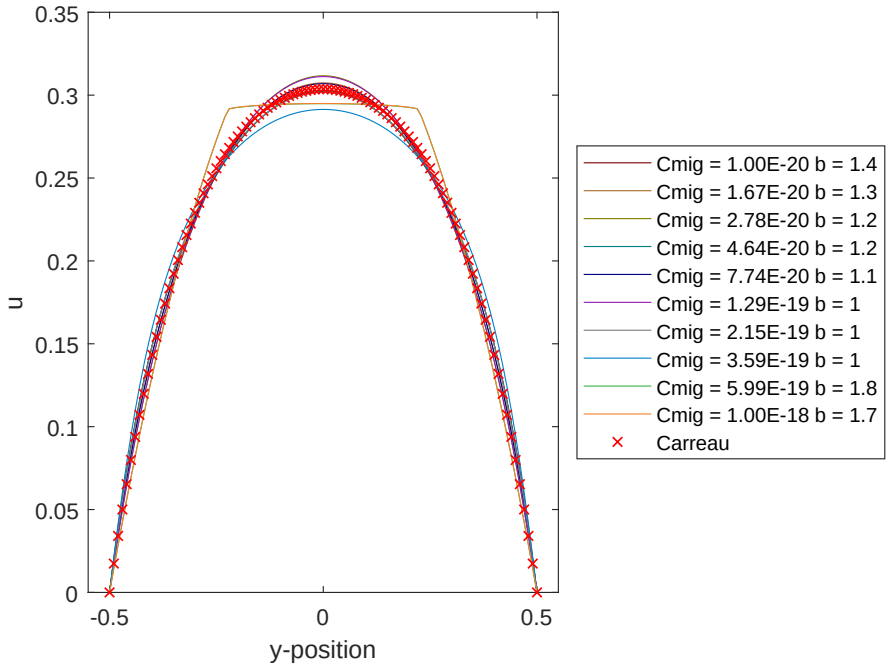

(a)

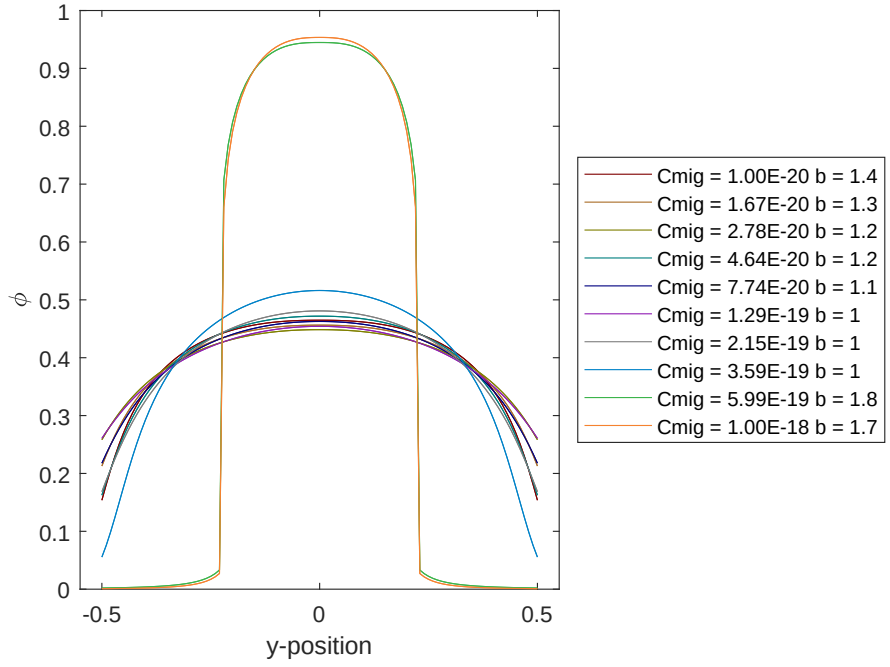

(b)

Figure 4.2: Comparison between the CEM and Carreau model. (a) Velocity profile of the minimum error between CEM and Carreau model for a each C_{mig} value tested while varying b. (b) Particle distribution of CEM for the cases in part a.

4.3. Comparison of the continuum effective medium (CEM) model with the Carreau viscosity model

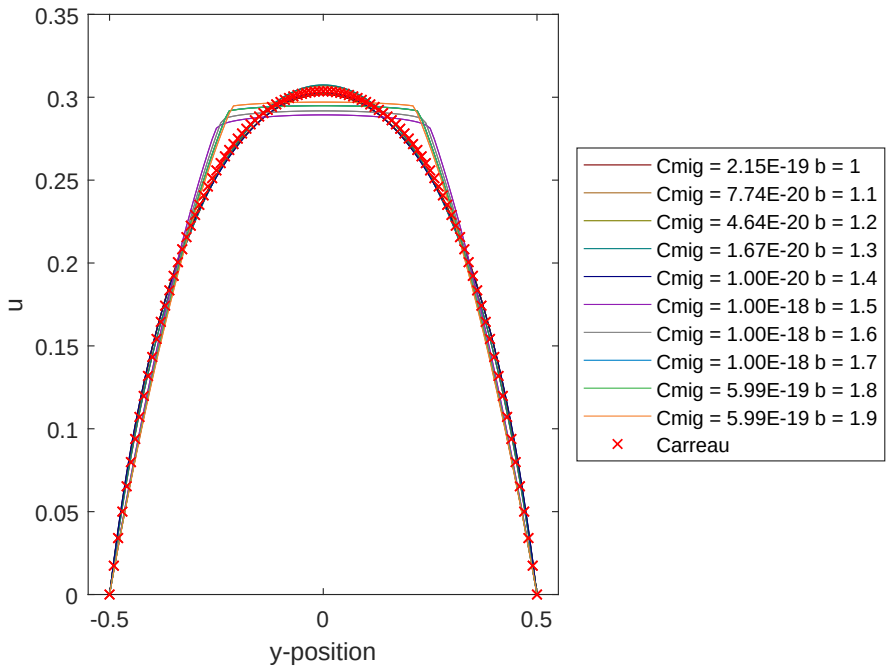

(a)

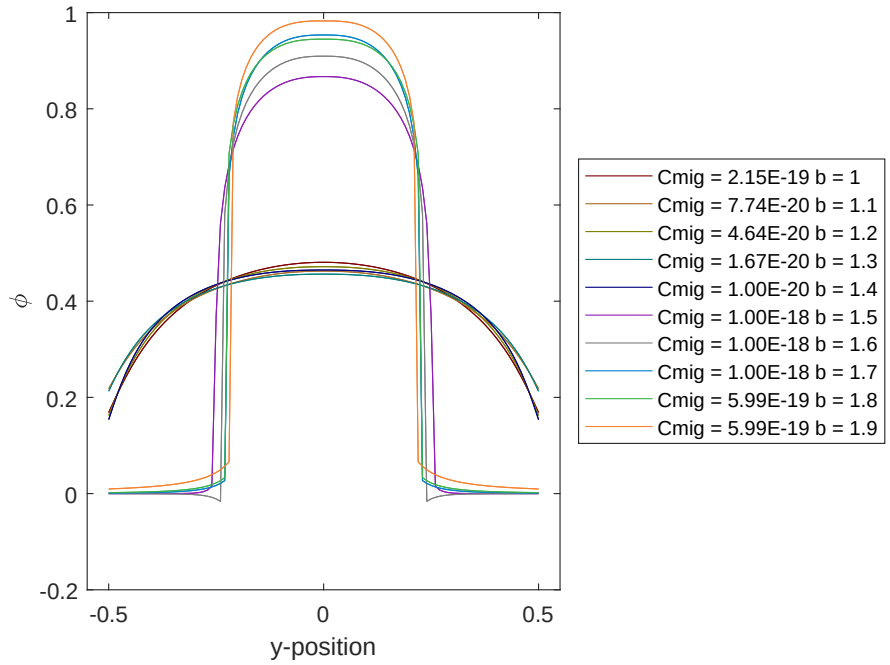

(b)

Figure 4.3: Comparison between the CEM and Carreau models. (a) Velocity profile of the minimum error CEM and the Carreau model for each b value tested while varying C_{mig}. (b) Particle distribution of CEM for the cases in part a.

4.3a) and a CFL, the region where the volume fraction is less than 0.05 (Figure 4.2b and 4.3b).

The one-dimensional CEM model can therefore simulate the formation of a CFL as indicated in Figure 4.2b and 4.3b. However, when the error between the velocity profile of the CEM model and the Carreau model is minimal, the CEM model does not produce a CFL. This is a result of continuum fluid models, such as the Carreau model, assuming that the fluid is a single phase and homogeneous, which is not true at small scales. Therefore, validating the CEM model with the Carreau model may only be valid for large vessels where the CFL has an insignificant thickness compared to the width of the channel. Matching the CEM to the continuum fluid models does provide the particle density distribution that is not present in just the continuum models but this has to be experimentally validated at the appropriate scale.

4.4 Numerical investigation of the continuum effective medium (CEM) model

There are many possible geometries that could perform cell separation for our needs. We will look at one of these, a contraction-expansion geometry (shown in Figure 4.4), comparing experimental and numerical simulations. This type of configuration has found some success in RBC separation processes, based on the enhancement of the CFL downstream of the expansion [Faivre et al., 2006; Yaginuma et al., 2013]. In addition, it is also interesting as a simplified model geometry where extensional effects are important, such as e.g. in stenosis or microfluidic networks composed of irregular vessel segments [Sousa et al., 2011; Yaginuma et al., 2013]. The dimensions of the geometry we considered are shown in Table 4.5. This study first finds the best mesh size, which is decided upon based on the convergence of the solution and the time needed to solve. Then,

Table 4.5: Dimensions of geometries used

Characteristics	Value
Width (W) (µm)	400
Contraction ratio (C_r)	8
Length (L_c)(µm)	500
Depth (µm)	30

a parametric study of the model parameters Pe and C_{mig} to gauge appropriate values and finally changes in the experimental parameters, haematocrit (HCT) and flow rate, were carried out to see the effect on the regions of low particle concentration.

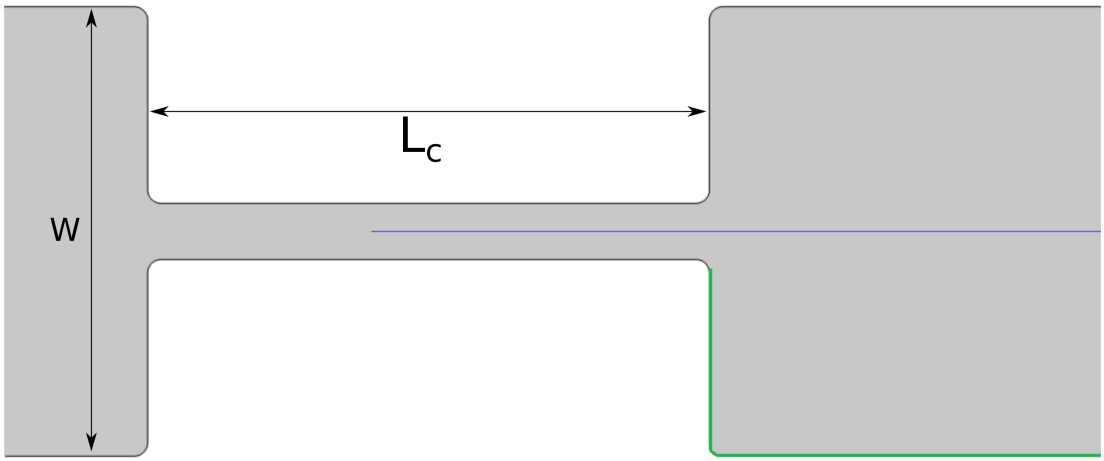

;

Figure 4.4: Geometry of contraction-expansion channel used for model testing. The lines along which results are taken are indicated; blue for midline and green for wall measurements.

4.4.1 Numerical Methodology

Initially, a parametric study was conducted to identify suitable numerical settings, mesh size and Peclet number and the effect of the CEM model parameter

C_{mig}, which would then be used for comparisons with experiments (Section 4.5). A contraction-expansion geometry was simulated as a two-dimensional problem in COMSOL v5.3a, the geometry of which is given in Figure 4.4. To prevent numerical error due to negative concentration values the concentration equation (4.14) was solved in terms of the artificial variable, s, where $\bar{c} = C_0 e^s$ [Ley and Bruus, 2016]. As with all numerical methods of this kind, the mesh size determines the accuracy of the result, and here we consider COMSOL's physics based meshes and one user defined mesh, details of which are shown in Table 4.6. The Peclet number is the ratio of rate advection by the flow to diffusion of the RBCs and the actual Peclet number for the system is $\approx 8 \times 10^6$. However, this high value causes increased computational cost. Therefore, to find an appropriate value for the Peclet number, for which the computational cost is acceptable while the model results are consistent, a parametric sweep for $Pe = 1 \times 10^2$ to 1×10^5 was conducted. Next the effect of the model parameter C_{mig} was explored using a parametric sweep for $C_{\text{mig}} = 4 \times 10^{-8}$ to 4×10^{-5} with the shear exponent, b, was set to 1 for initial model testing. The effect of changes in b could be investigated in the future. Plots, showing the concentration normalised to the inlet concentration ($\bar{c}/C_0$), are presented for the different studies at steady state.

Table 4.6: Mesh properties as defined in COMSOL

Physics based mesh	Maximum element size	Minimum element size	Maximum element growth rate	Curvature
Normal	0.067	0.003	1.2	0.4
Fine	0.045	0.002	1.15	0.3
Finer	0.035	0.001	1.13	0.3
Extra fine	0.028	4×10^{-4}	1.1	0.25
Extremely fine	0.013	1.5×10^{-4}	1.08	0.25
User defined	0.008	8×10^{-5}	1.07	0.25

The haematocrit (HCT) and the flow rate, Q, are the physical parameters

that can be controlled and in the model testing that follows, the haematocrit values were set to 0.1, 0.2 and 0.4. An undiluted peripheral blood sample, which has a haematocrit of around 0.4, would be used in the potential device, and the lower limit of 0.1 is tested, since it is sufficiently high that mescoscale methods mentioned in Section 4.1 would not be viable. The flow rate values of $Q = 10\ \mu\mathrm{l\,min^{-1}}$, $40\ \mu\mathrm{l\,min^{-1}}$ and $100\ \mu\mathrm{l\,min^{-1}}$ were chosen to be similar to those achievable in a real device and so that the Reynolds number is less than, around and greater than 1 respectively. The default parameters used in these tests are shown in Table 4.7 with the model parameters, Pe and C_{mig}, based on findings in the earlier parametric study and the experimental parameters $Q = 100\mu\mathrm{l\,min^{-1}}$ and HCT=0.4 were chosen as they were the desired operating parameters for the proposed microfluidic device.

Table 4.7: Default parameters used in the simulations.

Parameter	Value
Pe	1×10^4
C_{mig}	4×10^{-6}
Q	$100\ \mu\mathrm{l\,min^{-1}}$
HCT	0.4

4.4.2 Results and Discussion

4.4.2.1 Effect of Mesh size

As the mesh becomes more refined the numerical noise in the control region of the device reduces: the normal mesh (Figure 4.5a) and fine mesh (Figure 4.5b) showing large variations in normalised concentration, which is clearly seen in the recirculation region. Subjectively there is very little difference in the surface plots for the extra fine (Figure 4.5d), extremely fine (Figure 4.5e) and the user defined mesh (Figure 4.5f). Refining the mesh also decreases the global (across whole domain) maximum normalised concentration (2.29 to 1.5) while increasing the

global minimum (0.54 to 0.7), except for the user define mesh (0.69 and 1.51). Figure 4.6 quantitatively shows that the global average normalised concentration of the domain has the same trend as the global maximum and minimum with increasing refinement. Figure 4.7 then shows, quantitatively, that the numerical error in the normalised concentration along the midline of the channel (see Figure 4.4) reduces with increasing mesh refinement. As the mesh is refined, the peak normalised concentration moves closer to the contraction outlet, the extra fine and extremely fine meshes produce similar profiles whereas the rest have larger values as well as large oscillations. The normalised concentration at the wall (green line in Figure 4.4) shows that the positions of the global minimum and the local minimum do not change with mesh refinement (Figure 4.8) but their values increase with increasing mesh refinement. The computational cost for the different mesh sizes is then shown in Table 4.8. There is over 100% increase in time cost between extra fine and extremely fine meshes as well as from extremely fine to the user defined mesh. Since our study shows that the extra fine mesh computes average concentration of the domain very close to user define mesh (0.99479 compared to 0.99499) and is lot less computational costly, therefore it was decided that it would be used for further investigations of the model.

Table 4.8: Computation time (s) comparison between mesh sizes. For $Q = 100$ µl min^{-1}, HCT $= 0.4$, $C_{\text{mig}} = 4 \times 10^{-6}$ and $Pe = 1 \times 10^{4}$.

Mesh	Computation time (s)
Normal	371
Fine	582
Finer	1125
Extra fine	2347
Extremely fine	6185
User defined	17458

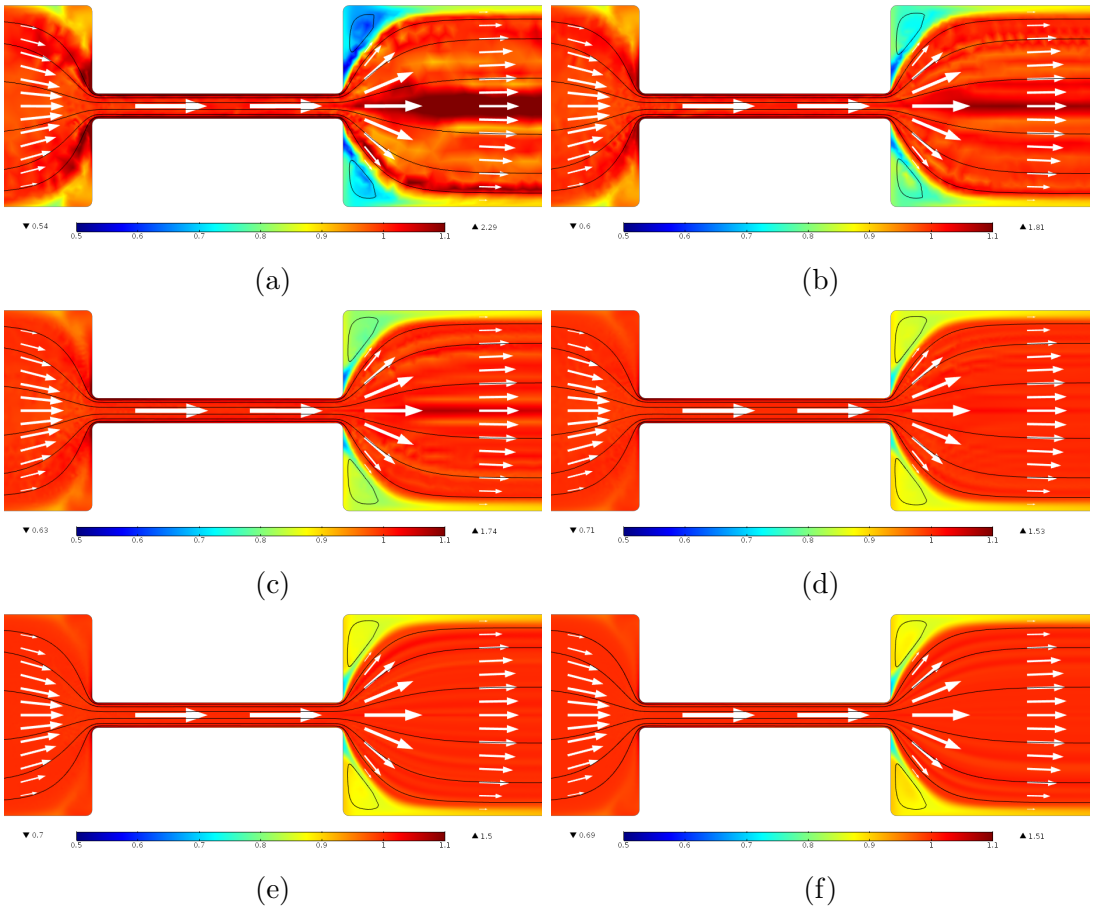

Figure 4.5: Normalised concentration (c/C_0) with streamlines (black) and velocity vectors (white) plot for different meshes: (a) Normal, (b) Fine, (c) Finer, (d) Extra fine, (e) Extremely fine and (f) User defined. For $Q = 100\ \mu\mathrm{l\,min^{-1}}$, HCT $= 0.4$, $C_{\mathrm{mig}} = 4 \times 10^{-6}$ and $Pe = 1 \times 10^4$.

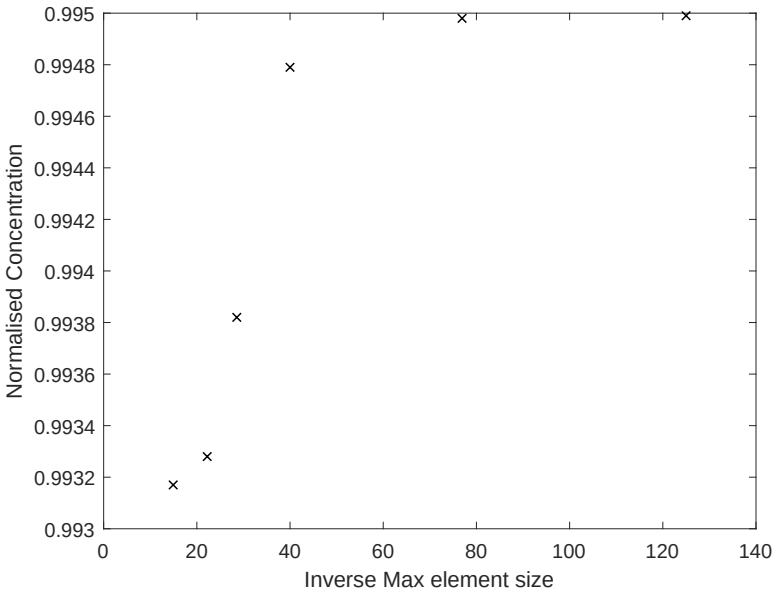

Figure 4.6: Mesh convergence study: Average global normalised concentration versus the inverse of the maximum mesh element size. For $Q = 100$ µl min^{-1}, HCT $= 0.4$, $C_{\text{mig}} = 4 \times 10^{-6}$ and $Pe = 1 \times 10^{4}$.

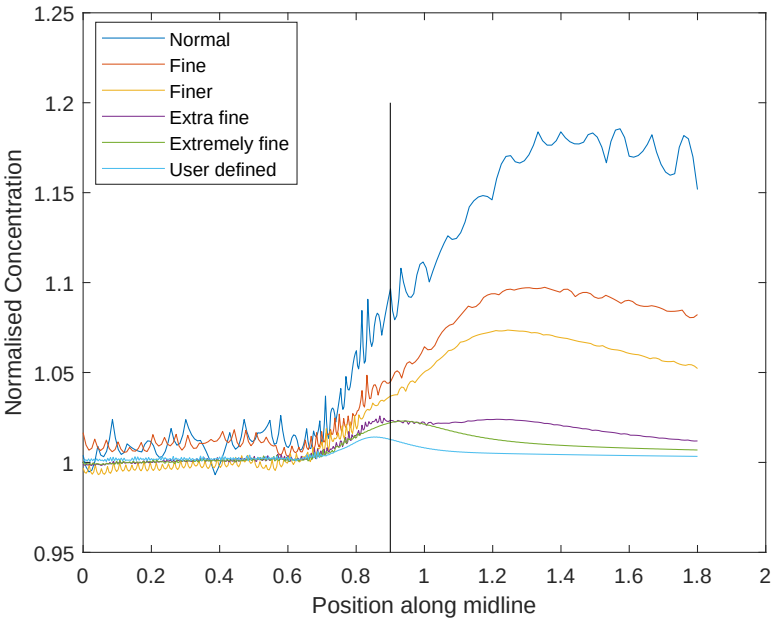

Figure 4.7: Mesh convergence study: Normalised concentration at positions along middle of channel (blue line in Figure 4.4) at steady state. For $Q = 100$ µl min^{-1}, HCT $= 0.4$, $C_{\text{mig}} = 4 \times 10^{-6}$ and $Pe = 1 \times 10^{4}$. Vertical line indicates start of expansion

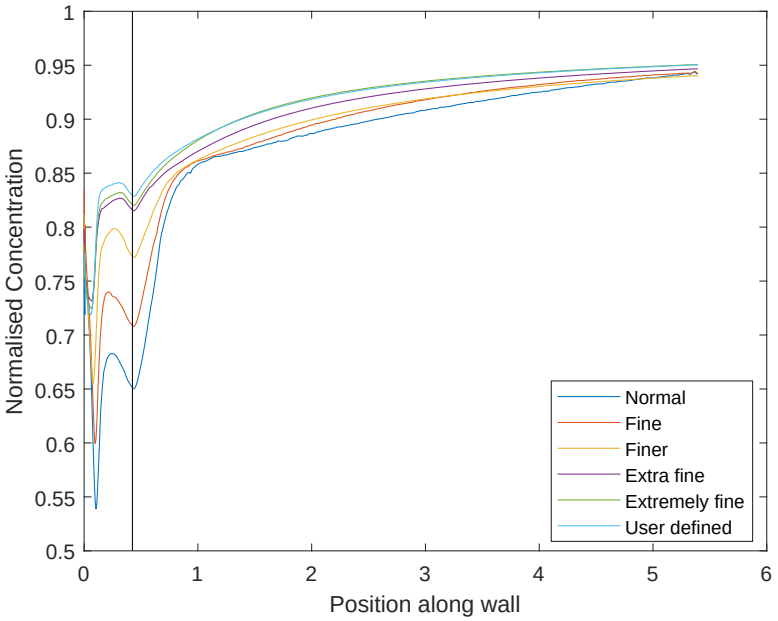

Figure 4.8: Mesh convergence study showing normalised concentration at positions along the channel wall (green line in Figure 4.4) at steady state. Vertical line is the point along the path where the horizontal wall starts. For $Q = 100$ µl min^{-1}, HCT $= 0.4$, $C_{\text{mig}} = 4 \times 10^{-6}$ and $Pe = 1 \times 10^4$

4.4.2.2 Effect of Peclet number

Figure 4.9 shows the normalised concentration for low, medium and high Peclet numbers, Pe= 1×10^3, 1×10^4 and 4.6×10^4 respectively. Figure 4.9a shows that the normalised concentration being around 0.9 in the corners after the contraction for $Pe = 1 \times 10^3$ whereas it is around 0.8 and 0.5 in Figure 4.9b and Figure 4.9c corresponding to $Pe = 1 \times 10^4$ and $Pe = 4.6 \times 10^4$ respectively. This indicates that the higher the Peclet number, the less diffusion occurs in steady state, as expected. For the remaining calculations we use Peclet number of 1×10^4, which is sufficiently high to show heterogeneity of the flow.

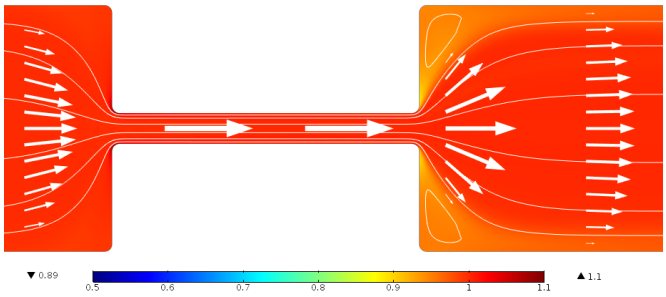

(a) $Pe = 1 \times 10^3$

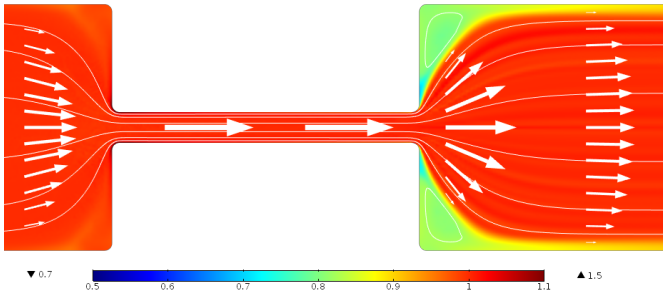

(b) $Pe = 1 \times 10^4$

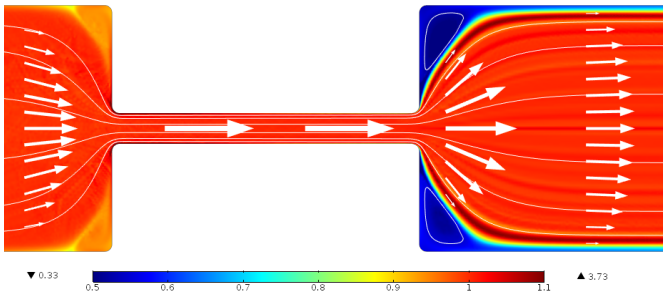

(c) $Pe = 4.6 \times 10^4$

Figure 4.9: Normalised concentration (c/C_0) with streamlines (white lines) and velocity vectors (white arrows) for different Peclet numbers and for $Q = 100$, HCT =0.4 and $C_{\text{mig}} = 4 \times 10^{-8}$.

4.4.2.3 Effect of coefficient of migration ($C_{\mathbf{mig}}$)

Figure 4.10 shows the effect of increasing the migration force coefficient, C_{mig}. Figure 4.10a presents the lowest value of C_{mig} where there migration effect, movement from areas of high shear, i.e away from the boundaries and recirculation regions, is present. Here we notice that the value of the normalised concentration at the walls on the outlet side of the contraction is around 0.8, whereas in Figure 4.10b and 4.10c the values are 0.7 and around 0.5 respectively. Increasing the value of C_{mig} therefore decreases the width of the transitional region between the wall concentration and the bulk. Determining the appropriate coefficient would rely on experimental validation but for further testing $C_{\mathrm{mig}}= 4\times10^{-6}$ was selected for convenience.

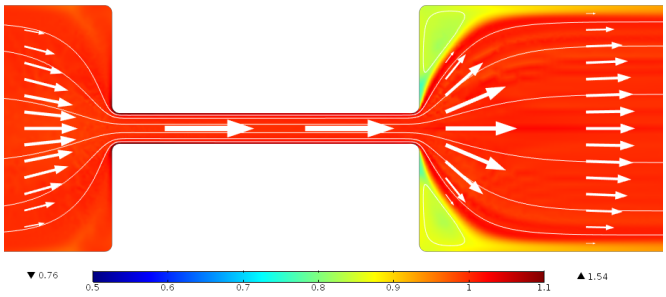

(a) $C_{\text{mig}} = 4 \times 10^{-8}$

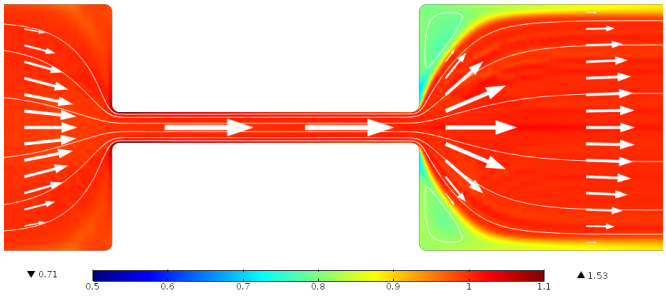

(b) $C_{\text{mig}} = 4 \times 10^{-6}$

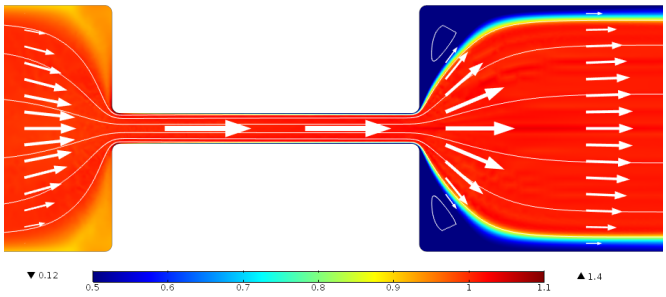

(c) $C_{\text{mig}} = 4 \times 10^{-5}$

Figure 4.10: Normalised concentration (c/C_0) with streamlines (white lines) and velocity vectors (white arrows) for different C_{mig} values and for $Q = 100$, HCT =0.4 and $Pe = 1 \times 10^4$.

4.4.2.4 Changing haematocrit (HCT) and flow rate (Q)

Figure 4.11 shows the effect of changes in the value of haematocrit on the normalised concentration field, with Figure 4.12a showing the normalised concentration at the wall as well as the global minimum and the global maximum. The position of the global minimum of the normalised concentration on the vertical wall (Figure 4.12b) moves away from the outlet with increasing HCT. The concentration in recirculation region also increases with increasing HCT as expected.

In considering changes to the flow rate, we note that for fluids at low flow rates the normalised concentration is higher in the corners of the expansion (Figure 4.13a). Therefore, for low flow rates the migration force is reduced, which can be explained by the presence of lower shear gradients. This is seen in Figure 4.14a where the normalised concentration at the wall is higher for $Q = 10\ \mu\mathrm{l\,min^{-1}}$ compared to $40\ \mu\mathrm{l\,min^{-1}}$ and $100\ \mu\mathrm{l\,min^{-1}}$. Increasing flow rates increases the shear gradient and leads to a higher migration force (Figures 4.13b and 4.13c). Figure 4.14b shows that the higher flow rate produces a lower concentration minimum and is closer to the contraction outlet. This particular investigation is key to our device development, and shows the best position for collecting plasma is on the vertical wall, where the normalised concentration is lowest, and that the location of which will change depending on a combination of the haematocrit of the intended blood sample and the flow rate chosen. To collect plasma at these locations a new channel with collection channels at these locations would need to be designed and fabricated.

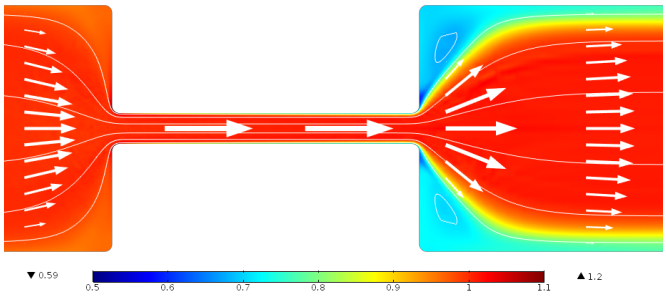

(a) HCT = 0.1

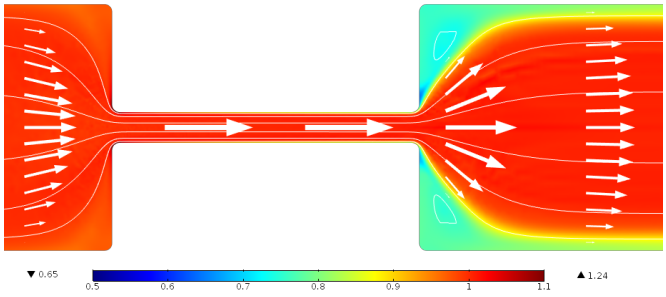

(b) HCT = 0.2

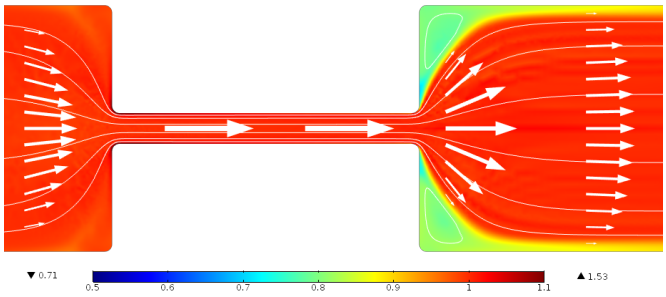

(c) HCT = 0.4

Figure 4.11: Contour plot of normalised concentration (c/C_0) with streamlines (white lines) and velocity vectors (white) for different HCT values. Parameter values $C_{\text{mig}} = 4 \times 10^{-6}$, $Q = 100$ and $Pe = 1 \times 10^4$.

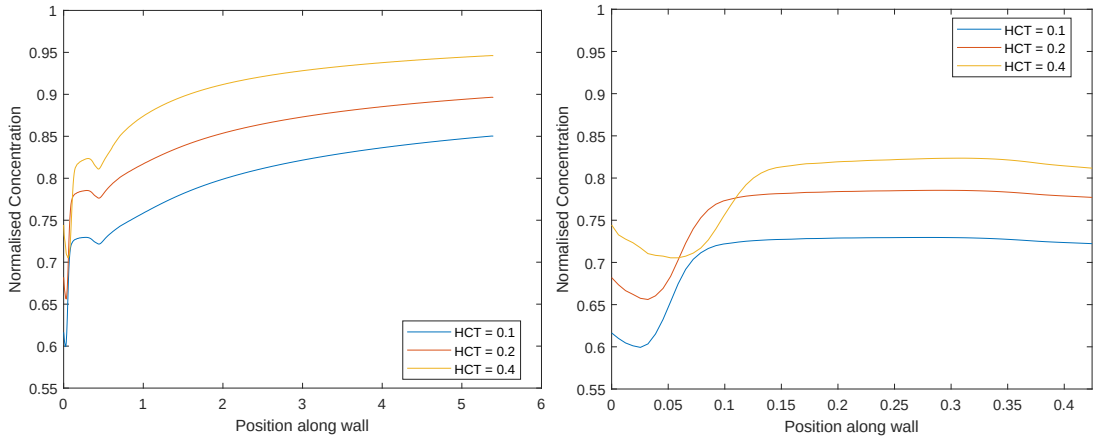

(a) (b)

Figure 4.12: Normalised concentration (c/C_0) plot along the wall (green line in Figure 4.4) for different HCT values. a) Full length of wall, b)on the vertical section of the wall only. Parameter values $C_{\text{mig}} = 4 \times 10^{-6}$, $Q = 100$ and $Pe = 1 \times 10^4$.

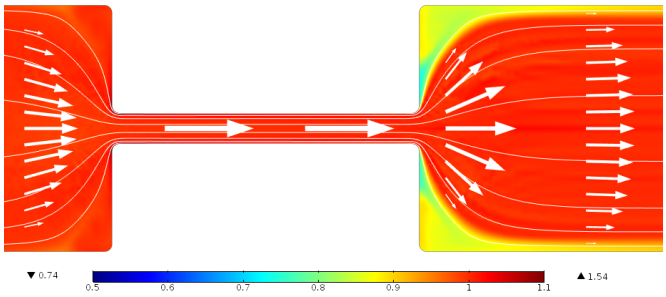

(a) $Q = 10\mu l\,min^{-1}$

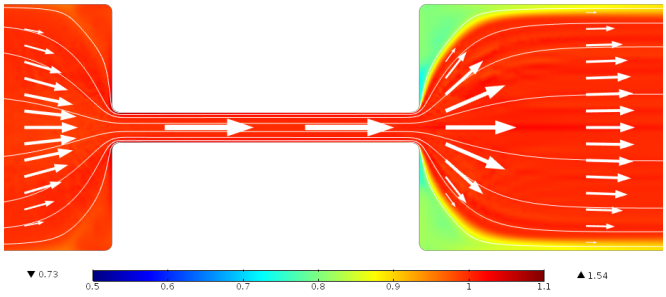

(b) $Q = 40\mu l\,min^{-1}$

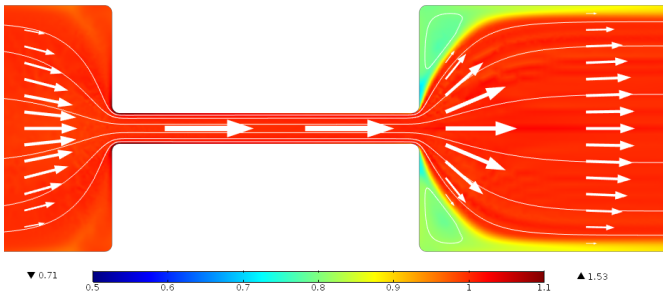

(c) $Q = 100\mu l\,min^{-1}$

Figure 4.13: Contour plot of normalised concentration (c/C_0) with streamlines (white lines) and velocity vectors (white) for different Q values. Parameters values $C_{\text{mig}} = 4 \times 10^{-6}$, HCT =0.4 and $Pe = 1 \times 10^4$.

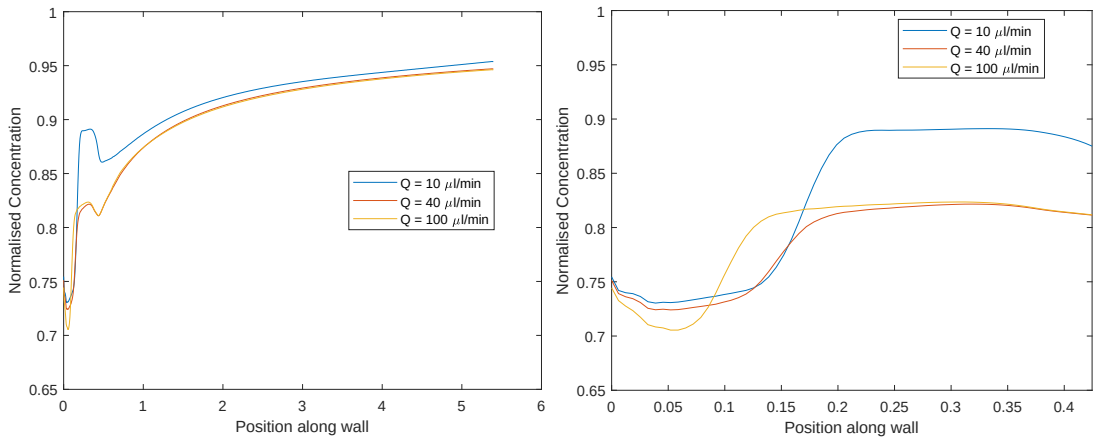

Figure 4.14: Normalised concentration (c/C_0) plot along the wall (green line in Figure 4.4 for different Q values. a) full wall b) on the vertical section of the wall only. Parameters values $C_{\text{mig}} = 4 \times 10^{-6}$, HCT =0.4 and $Pe = 1 \times 10^4$.

4.5 Experimental comparison

To ensure that the numerical model captures the flow behaviour, visualisations were carried out at the microscale for comparison. Numerical simulations, using the default parameters shown in Table 4.7 with extra fine mesh, were compared to the flow of RBCs in microfluidic contraction-expansion channels with three different configurations (see Figure 4.15 and Table 4.9). The effect of changing HCT and Q were investigated for both numerical simulation and experiment.

4.5.1 Experimental Methodology

4.5.1.1 Sample preparation

In the microfluidic experiments, we use suspensions of horse RBCs in saline to model different hematocrit sample values. Horse blood in ethylenediamine tetraacetic acid (EDTA) (TCS Biosciences Ltd, Buckingham, UK) was pipetted into centrifuge tubes. The tubes were centrifuged (Jouan BB3V, Thermo Scientific) for 5 minutes at 3000 rpm, the supernatant (liquid component) was discarded using a pipette and replaced with fresh saline. The samples were then gently agitated and centrifuged again. This process was repeated until the saline remained clear and colourless. The saline was discarded and the RBCs was pipetted into 10 ml sample tube with fresh saline to make up stock suspensions with different hematocrit (HCT=0.1, 0.2 and 0.4) to be used in the experiments.

Table 4.9: Dimensions of geometries used

Characteristics	1	2	3
Width W (µm)	400	400	400
Channel depth (ChD) (µm)	30	30	30
Contraction ratio (C_r)	8	8	4
Length (L_c) (µm)	500	90	90

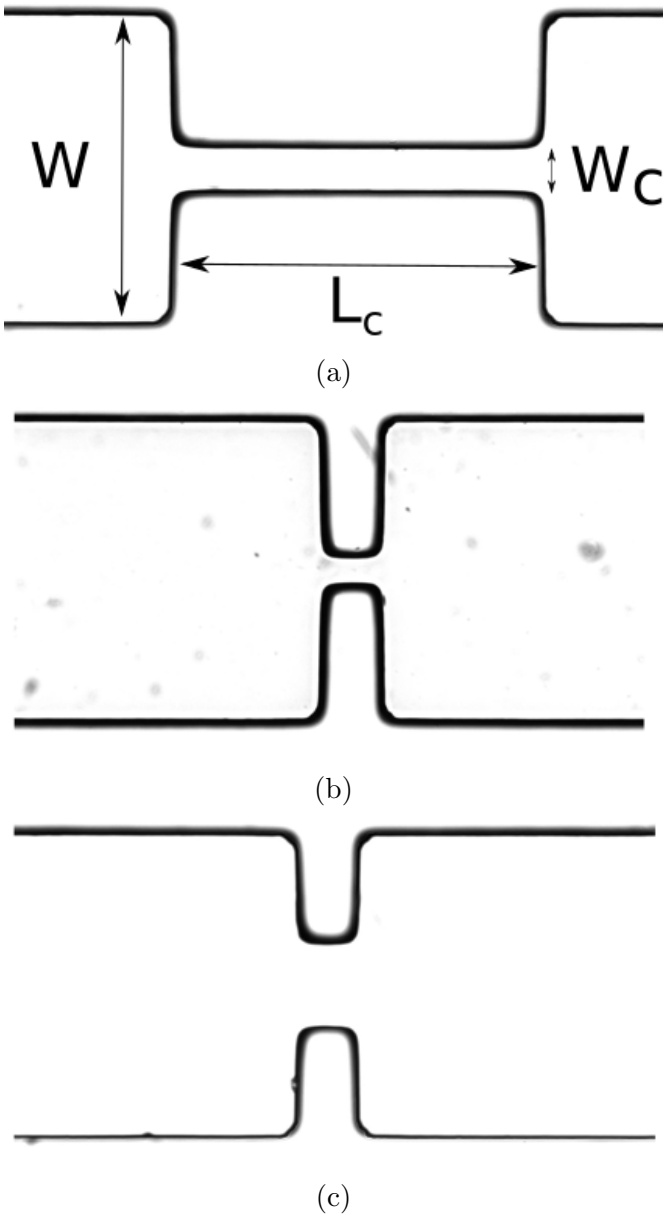

(a)

(b)

(c)

Figure 4.15: Micrographs of the geometries used: a) channel 1 b) channel 2 and c) channel 3 and important geometrical parameters.

4.5.1.2 Fabricating Channels

Simple contraction-expansion geometries of constant depth were used. The channels were fabricated from polydimethylsiloxane (PDMS) using standard photolithography and soft lithography processes. These techniques are nowadays well established, as described in Sections 2.3.1 and 2.3.2, and are ideal for our experiments as they allow for reproducible and inexpensive fabrication of microdevices that are optically transparent and biocompatible. The mould was manufactured externally (microLiquid, Gipuzkoa, Spain) using photolithography and the channels were produced in house using soft lithography. Schematics for the generic process have been presented in Chapter 2 (Figure 2.10) and the steps that were followed are:

1. Preparing mould: Cleaning mould with isopropanol and drying with compressed air. Surround the mould in tin foil to contain the polymer

2. Preparing polymer: PDMS (Sylgard 184, Dow Corning) prepolymer kit composed of a PDMS oligomer and a curing agent were mixed at 9:1 w/w ratio PDMS : curing agent to produce 50 g elastomer.

3. The elastomer was mixed in two steps, mixing (2000 rpm for 5 min) and defoaming (1600 rpm for 1 min)

4. The elastomer was poured over the mould until it was suitably covered

5. The mould covered in PDMS was placed in a vacuum desiccator to remove dissolved gas bubbles from elastomer

6. While mould was degassed, a microscope slide was spin coated with PDMS. The slide was prepared by cleaning with isopropanol and dried with compressed air. The slide was then placed in the spin-coater and small drop of PDMS was placed in the centre of the slide. Spin-coater rotates the slide at

6000rpm for 1min following 10 s ramp. This produces a thin film covering of PDMS on the slide of ≈13(±3)µm

7. Once degassing and spin coating was complete, both the PDMS and spin coated slide were placed in the oven at 80 °C for 25 min to cure.

8. The channels were cut out of the mould using a scalpel and cleaned with isopropanol. The inlets and outlets to the channels were punched (Harris Uni-core 1.00 mm puncher)

9. Sealing the channels with the glass slide was carried out using oxygen plasma. The slide and channels were placed in the unit and the surface was activated. The activated surfaces were placed together forming a seal. To improve the bonding the sealed chip was placed in the oven for further 10 min.

4.5.1.3 Experimental set up

Optical microscopy was used to visualise the flow of the RBC suspensions in the microfluidic devices. The sample flow rate for the experiments was controlled using syringe pump (neMESYS, Cetoni, Germany) (Figure 4.16). A 250 µl glass syringe (SGE Analytical Science (now Trajan), Australia) was used for the RBC suspensions. Microbore tubing (Tygon, Saint Gobain, France) was used to connect the syringe to the inlet and connect the outlet to waste container.

The chip was placed on an Olympus IX71 inverted microscope stage (Figure 4.16) and illuminated with white light. A ×10 objective magnification (NA=0.25) was focused into the midplane, which gave a depth of field of 8.5µm. As this is less than the depth of the channels (30µm), therefore a lot of the RBCs was not be in the focal plane. Still images were captured by a monochrome charged couple device camera (Olympus XM10, Japan) and recorded as videos using Cellsens (Olympus, Japan) software.

The parameters for the experiment is shown in Table 4.10. Before each run, the channel was washed with distilled water to wash out debris from fabrication and from previous runs. Videos were captured once the flow becomes stable and at least 500 frames were recorded with three repeats for each condition.

Figure 4.16: Experimental set up: Showing image of syringe pump and inverted microscope (Olympus XI71).

Table 4.10: Experimental parameters tested for all channels

HCT	Flow rate (Q)(µl min^{-1})
0.1 0.2 0.4	100
0.4	10 40 100

4.5.1.4 Image Processing

The videos were saved as .avi files and Matlab code was created to import and process the individual video files. The first 500 frames (Figure 4.17a) from each video were converted from 8 bit grayscale to a numeric matrix. The numeric matrix was needed to allow for the mean intensity frame to be calculated as 8 bit structure saturates during addition of frames. The mean intensity is an array of average pixel intensities over the 500 frames. In steady flow condition, this would cause pixels where more cells that pass through to be darker compared to where

there is just matrix fluid [Faivre et al., 2006]. Finally the matrix is converted back to an 8 bit grayscale image for comparison with numerical results (Figure 4.17b).

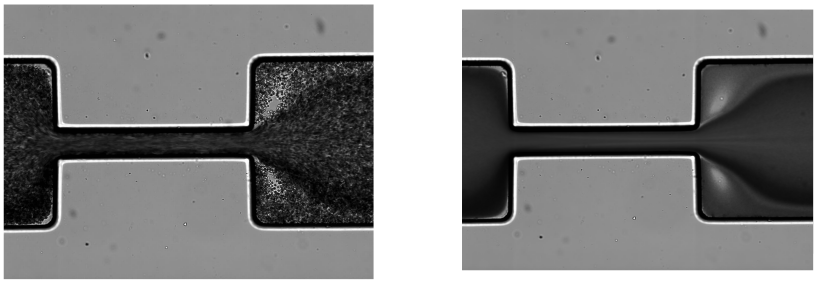

(a) (b)

Figure 4.17: Image processing; (a) single frame and (b) Mean intensity of 500 frames.

4.5.2 Results: Changing haematocrit and flow rate (Q)

Increasing the haematocrit in the numerical model results in a relatively small reduction in the size of the recirculation region for all three geometries (Figure 4.18, 4.19 and 4.20). Experimentally, in geometries 1 and 2, the region of recirculation downstream of the expansion, indicated by the lighter areas, disappears (Figure 4.18b, 4.18d and 4.19b, 4.19d) and a small CFL is present in the corners (Figure 4.18f and Figure 4.19f). Additionally, in geometry 1 the shape of RBC distribution is different between the numerical and experimental results; the presence of recirculation in the experiment seems to focus the RBCs (Figures 4.18b and 4.18d), which is not replicated numerically, where the centre of recirculations are located further away from the midline (Figures 4.18a and 4.18c). For these conditions, the experimental results shows that geometry 3 does not have flow recirculation at HCT= 0.1, which is indicated by the lack of RBCs in the region, but has a large CFL (Figure 4.20b), the size of which decreases with increasing

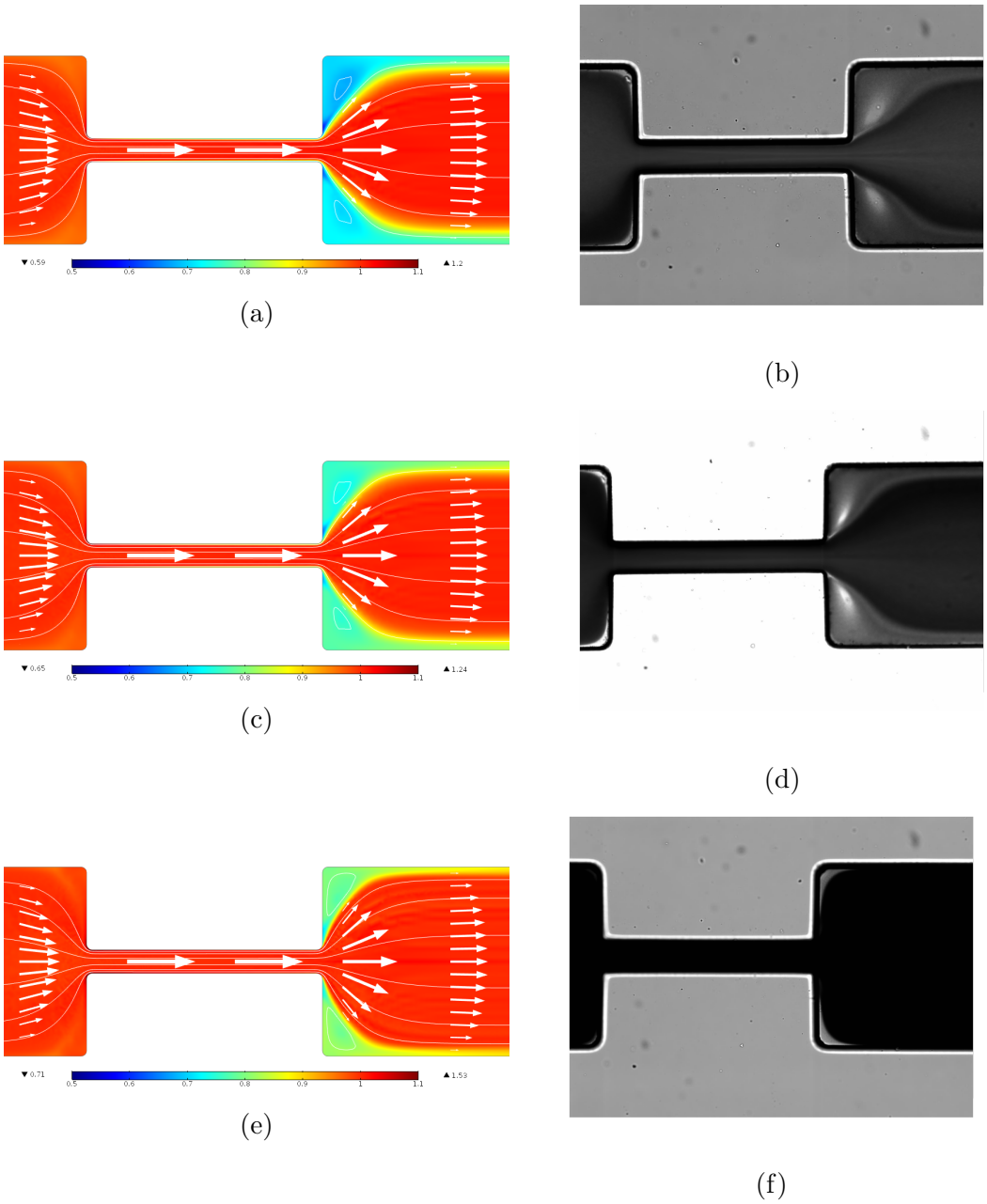

Figure 4.18: Comparison between numerical simulation and experimental results for a range of HCT using channel 1 (Q= 100 µl min^{-1}). (a), (c) and (e) are the numerical results, showing the normalised concentration (c/C_0), for HCT= 0.1, 0.2, 0.4 respectively. (b), (d) and (f) are the corresponding experimental results, showing the mean intensity of 500 frames.

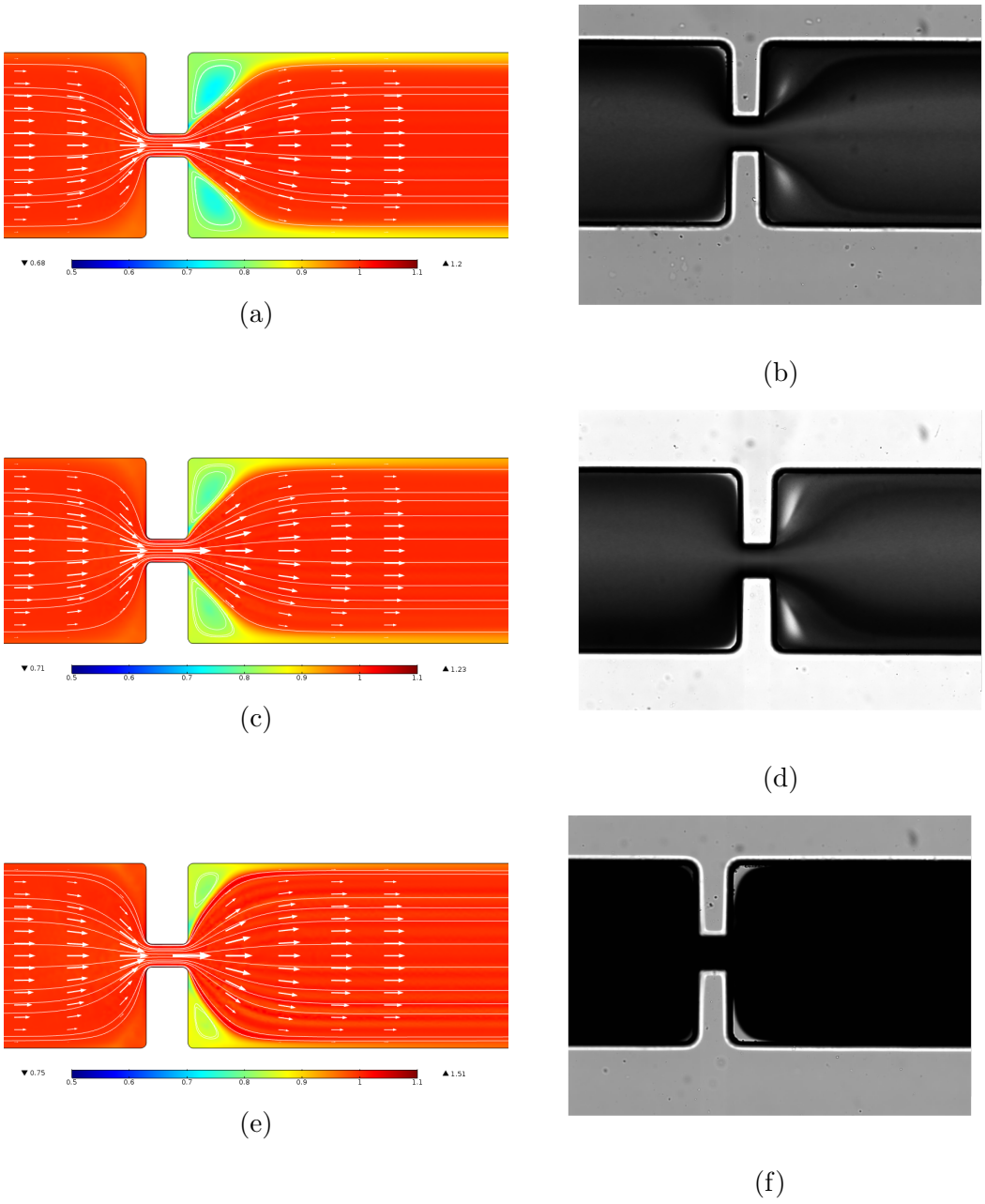

Figure 4.19: Comparison between numerical simulation and experimental results for a range of HCT using channel 2 (Q= 100 µl min^{-1}). (a), (c) and (e) are the numerical results, showing the normalised concentration (c/C_0), for HCT= 0.1, 0.2, 0.4 respectively. (b), (d) and (f) are the corresponding experimental results, showing the mean intensity of 500 frames.

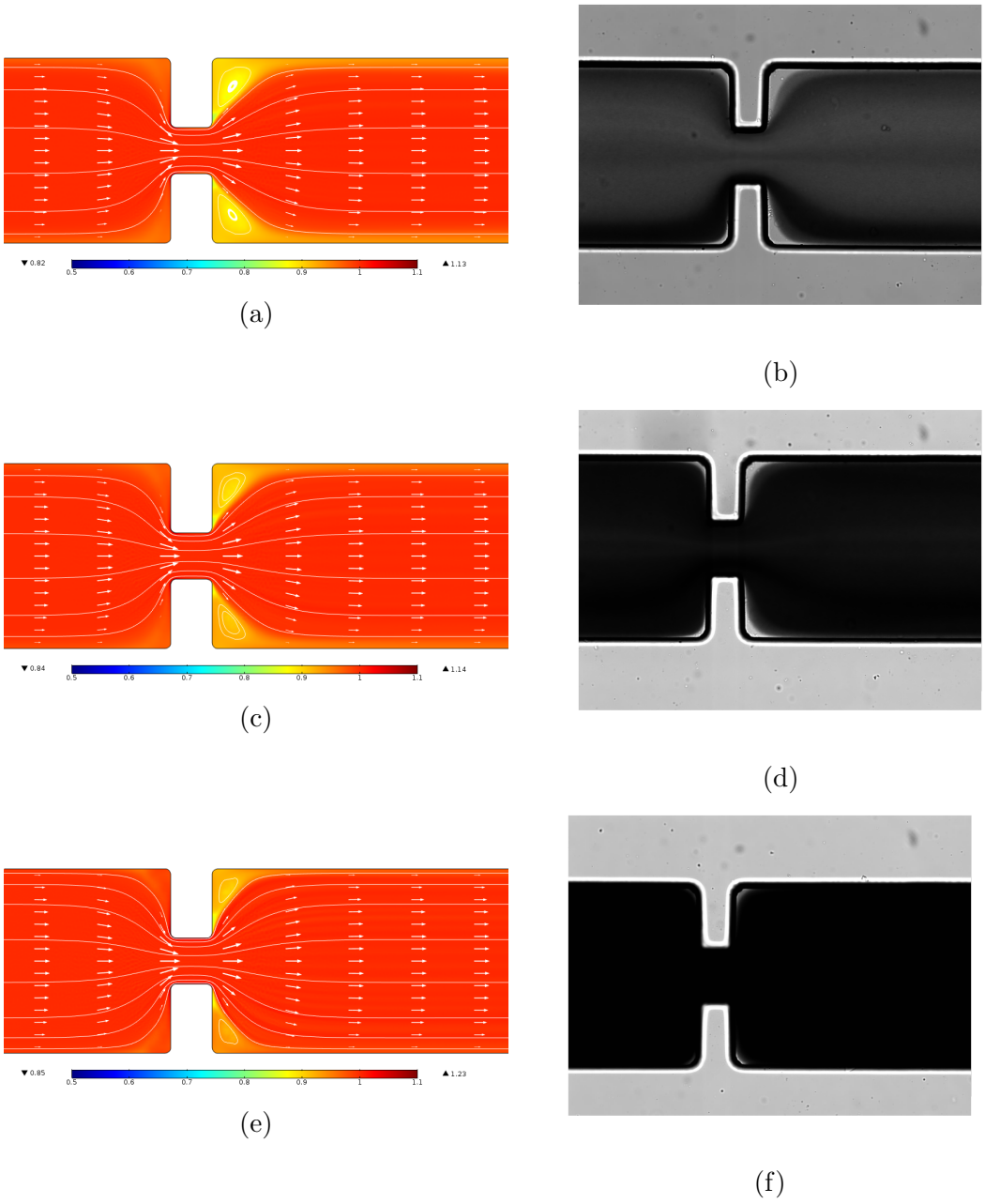

Figure 4.20: Comparison between numerical simulation and experimental results for a range of HCT using channel 3 (Q= 100 µl min^{-1}). (a), (c) and (e) are the numerical results, showing the normalised concentration (c/C_0), for HCT= 0.1, 0.2, 0.4 respectively. (b), (d) and (f) are the corresponding experimental results, showing the mean intensity of 500 frames.

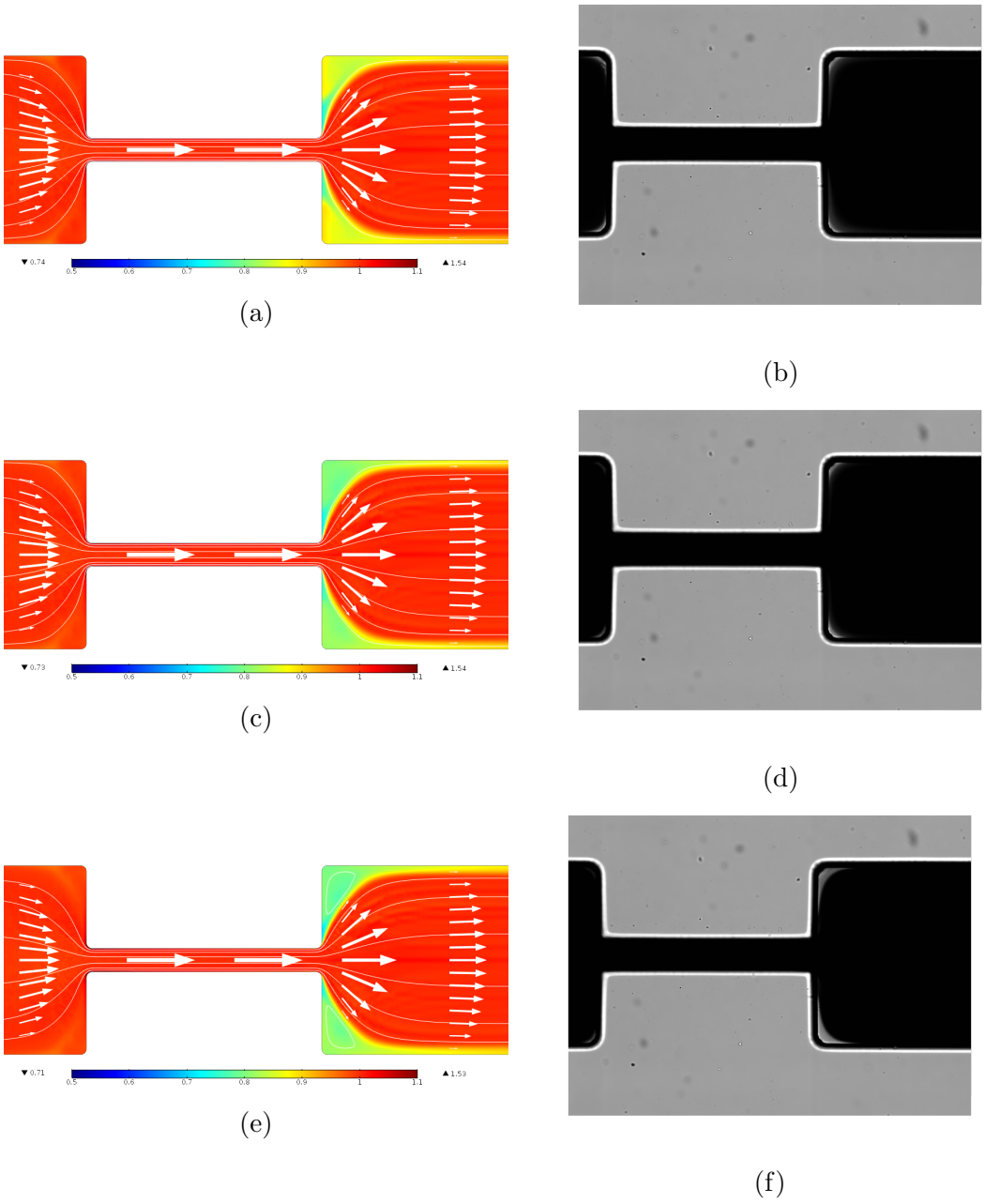

Figure 4.21: Comparison between numerical simulation and experimental results for a range of flow rate (Q) using channel 1 (HCT= 0.4). (a), (c) and (e) are the numerical results, showing the normalised concentration (c/C_0), for Q= 10 µl min^{-1}, 40 µl min^{-1}, 100 µl min^{-1} respectively. (b), (d) and (f) are the corresponding experimental results, showing the mean intensity of 500 frames.

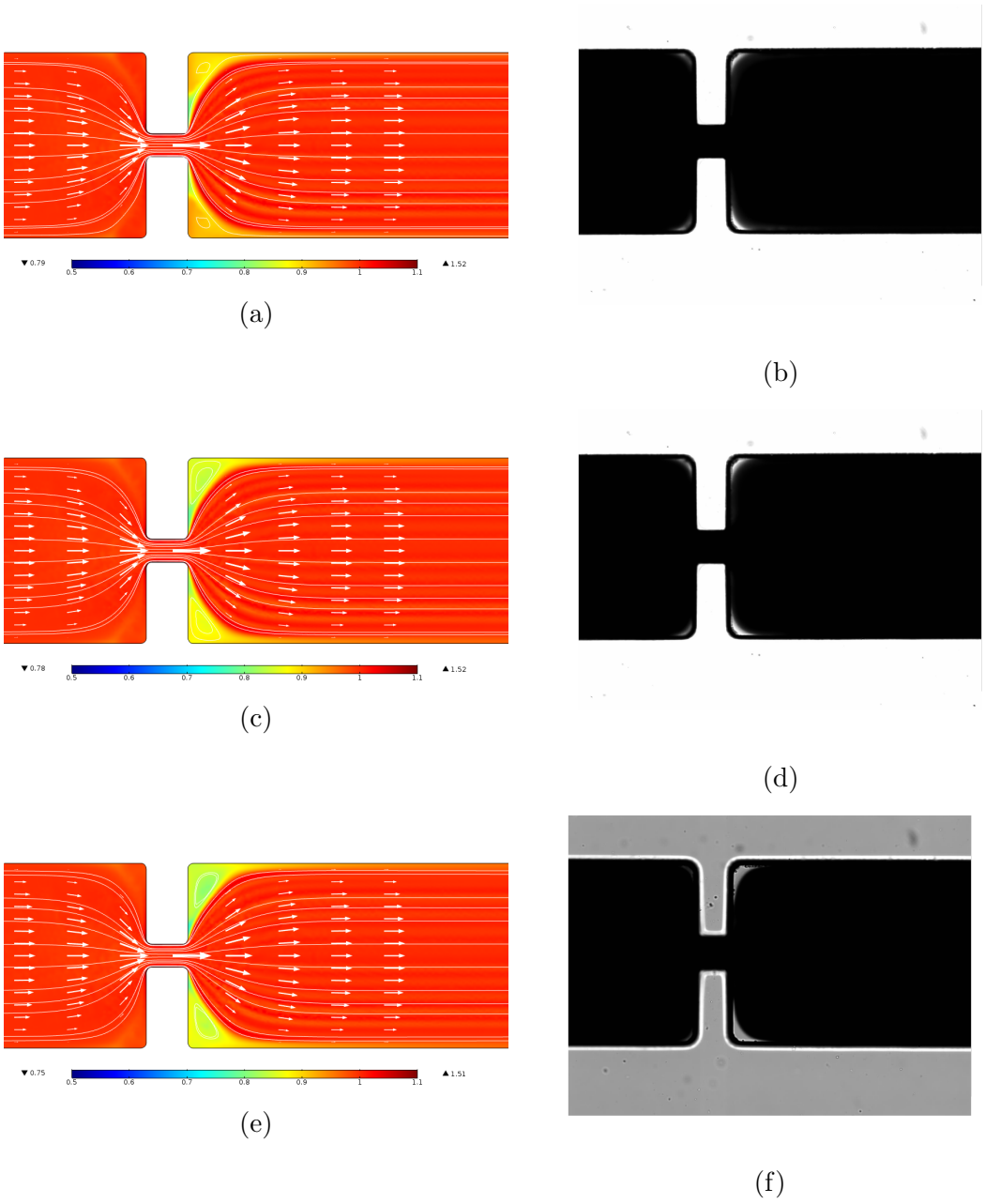

Figure 4.22: Comparison between numerical simulation and experimental results for a range of flow rate (Q) using channel 2 (HCT=0.4). (a), (c) and (e) are the numerical results, showing the normalised concentration, for Q=10 µl min^{-1}, 40 µl min^{-1}, 100 µl min^{-1} respectively. (b), (d) and (f) are the corresponding experimental results, showing the mean intensity of 500 frames.

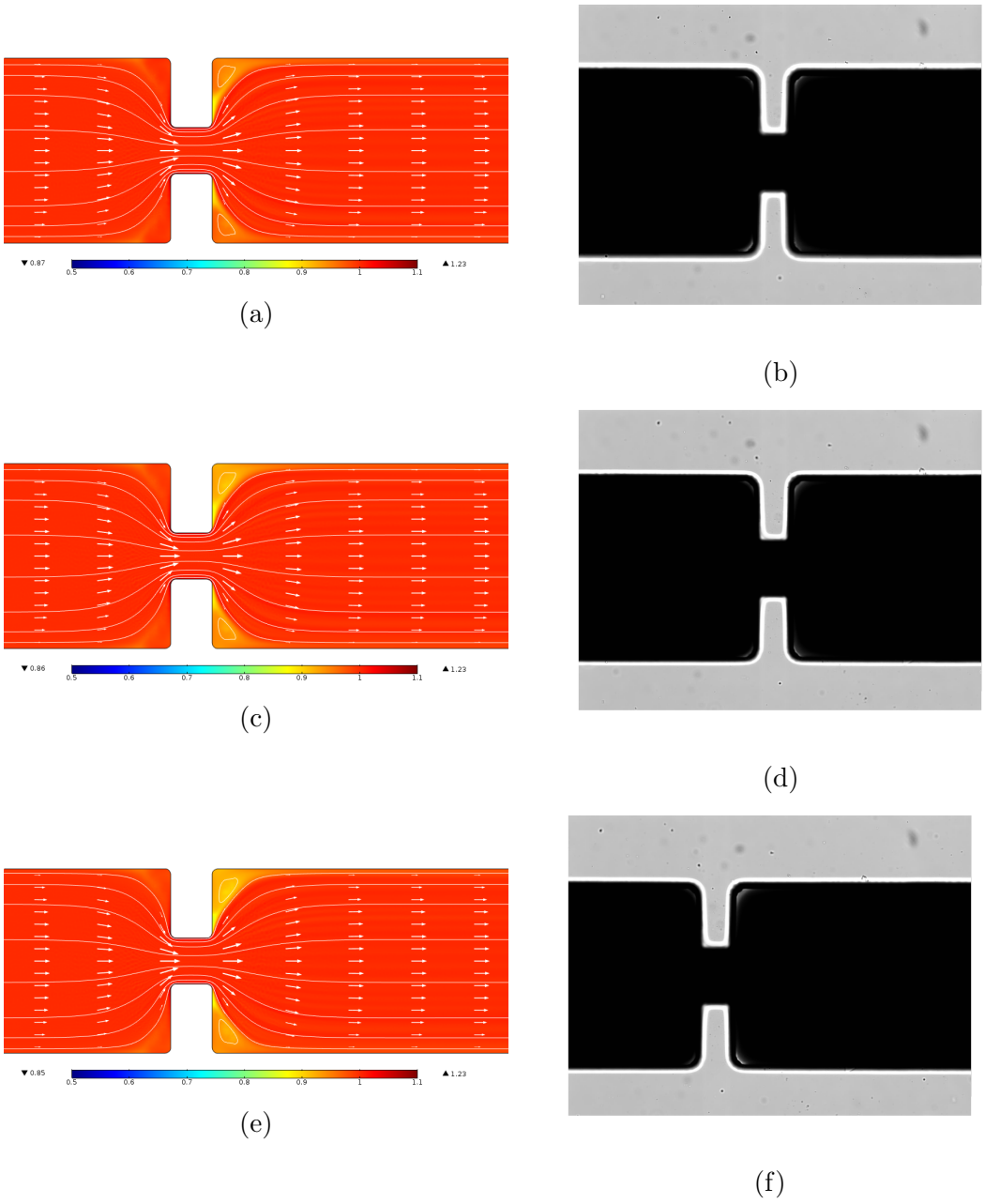

Figure 4.23: Comparison between numerical simulation and experimental results for a range of flow rate (Q) using channel 3 (HCT= 0.4). (a), (c) and (e) are the numerical results, showing the normalised concentration (c/C_0), for Q= 10 µl min^{-1}, 40 µl min^{-1}, 100 µl min^{-1} respectively. (b), (d) and (f) are the corresponding experimental results, showing the mean intensity of 500 frames.

haematocrit (Figure 4.20d and 4.20f). The lack of flow recirculation is incompatible with the numerical model, which can be explained by the fact the numerical model assumes no resistance at the outlet but experimentally this was not the case. The tubing that connects the outlet of the channel to the waste collection container adds resistance which was significant for these haematocrit values.

Increasing the flow rate increases the CFL in all three geometries for both the numerical model and the experiment (Figures 4.21, 4.22 and 4.23). The differences in the pattern between the numerical model and the experiments can also be attributed to the numerical model not capturing the back pressure caused by the RBCs slowing down when transitioning from the chip to the outlet tubing. Comparing the geometries, we can clearly see that geometry 1 produces the largest CFL with geometry 3 producing the smallest. Comparing geometry 1 with geometry 2, which has the same contraction ratio but shorter contraction length, the flow is able to fully develop in geometry 1 and the more inertial effects lead to larger recirculation regions. In geometry 3, the contraction ratio is less then that of geometry 2 but with the same contraction length, the RBCs are less focused and the lower inertial effects lead to smaller recirculation region in the numerical model and experimentally, this is seen as a thinner CFL.

4.5.3 Discussion

Quantitative analysis was not possible using just bright field microscopy, as the pixel intensities recorded do not have a linear relationship with the number of cells. This is due to light not being absorbed uniformly in the cell, scattering of light by the cell membrane as well as the detector not being able to differentiate between increasing concentrations once the light path is blocked. At the haematocrit values used, the majority of the channel is opaque and therefore local variation in cell concentration could not be measured. Therefore, qualitative analysis of how the flow changed with the different geometry and conditions was

used.

The experiments showed that using a geometry with a longer constricted section causes a more defined CFL which is in agreement with Faivre et al. [2006]. The increase in the width of the contraction, geometry 3, resulted in a less defined CFL which is also in agreement with the findings of Faivre et al. [2006]. The differences between the findings of this study and Faivre et al. [2006], the effect of increasing haematocrit, can be attributed to the higher haematocrit used in this study. Faivre et al. [2006], using 0.001 and 0026 haematocrit, showed that increasing haematocrit resulted in an increase in the CFL but here it has been shown that increasing haematocrit decreases the CFL. The interactions between the RBCs were insignificant in Faivre et al. [2006] but at 0.1 haematocrit in our experiment it becomes significant. The flow rate was also shown to have a more significant effect than what was found by Faivre et al. [2006], this can be attributed to the suspending fluid. Faivre et al. [2006] used a high viscosity buffer, whereas here the viscosity was close to that of water. This combined with the larger mass of RBC created more inertia.

With the set up used, it was not possible to track individual cells between frames due to the velocity of the cells and individual cells were hard to resolve. This could be overcome by using a higher speed camera; where a higher frame rate could be able to capture a cell before it travelled outside the field of view. One method of tracking cells by their streamlines is to use fluorescent labels. Labelling some of the cells would then allow tracking of individual cells and the inference of RBCs distribution [Lima et al., 2008]. The proportion of cells that would be required to be labelled would need to be investigated to ensure that the fluorescence does not saturate the camera, and so that the labelled cells are discrete entities. As the initial position of the cell would be random, the capture time would also need to be very long to ensure that the full cross-section of the channel would be covered. The numerical model can be evaluated with low

heamatocrit and dextran 40, where it is easier to measure the CFL and widen the use of the model.

4.6 Conclusion

In summary, we have successfully coupled the distribution of RBCs, via density, with the velocity field in our CEM model and showed the formation of a CFL. We have compared our CEM model and the classical Carreau model in one dimension, and determined that the Carreau model may not be suitable for the conditions in our device. Our CEM model was numerically implemented in two dimensions, and we determined that the extra fine mesh, a physics based mesh produced by COMSOL, was suitable. In order to reduce the computational cost we determined that a Peclet number of 1×10^4 was sufficiently high enough to not affect the steady state behaviour. We also investigated the effect of changing the C_{mig}, the migration parameter, which behaved as expected, with a higher level of migration leading to more pronounced CFL. We made initial comparisons of the model with experiments but we will need to undertake more testing to produce a validated model. The outlet conditions of the numerical model assumed no resistance, which simulates the conditions in a potential microfluidic chip but this was not achieved in the experiment. Therefore, more work on the CEM model is needed to fit the experimental conditions. Once this has been achieved our CEM model has the potential to be used as a design tool for developing microfluidic chips that separate cells based on Fåhræus-Lindqvist effect and cell margination.

4.7 References

Campo-Deaño, L., Oliveira, M. S. and Pinho, F. T. [2015], 'A review of computational hemodynamics in middle cerebral aneurysms and rheological models

for blood flow', *Applied Mechanics Reviews* **67**(3).

Cho, Y. I. and Kensey, K. R. [1991], 'Effects of the non-newtonian viscosity of blood on flows in a diseased arterial vessel. part 1: Steady flows', *Biorheology* **28**(3-4), 241–262.

Faivre, M., Abkarian, M., Bickraj, K. and Stone, H. A. [2006], 'Geometrical focusing of cells in a microfluidic device: an approach to separate blood plasma', *Biorheology* **43**(2), 147–159.

Fedosov, D. A., Noguchi, H. and Gompper, G. [2014], 'Multiscale modeling of blood flow: from single cells to blood rheology', *Biomechanics and modeling in mechanobiology* **13**(2), 239–258.

Johnston, B. M., Johnston, P. R., Corney, S. and Kilpatrick, D. [2004], 'Non-newtonian blood flow in human right coronary arteries: steady state simulations', *Journal of biomechanics* **37**(5), 709–720.

Kim, J., Antaki, J. F. and Massoudi, M. [2016], 'Computational study of blood flow in microchannels', *Journal of Computational and Applied Mathematics* **292**, 174–187.

Ladd, A. J. [1990], 'Hydrodynamic transport coefficients of random dispersions of hard spheres', *The Journal of chemical physics* **93**(5), 3484–3494.

Ley, M. W. and Bruus, H. [2016], 'Continuum modeling of hydrodynamic particle–particle interactions in microfluidic high-concentration suspensions', *Lab on a Chip* **16**(7), 1178–1188.

Li, H., Chang, H., Yang, J., Lu, L., Tang, Y. and Lykotrafitis, G. [2018], 'Modeling biomembranes and red blood cells by coarse-grained particle methods', *Applied Mathematics and Mechanics* **39**(1), 3–20.

Lima, R., Ishikawa, T., Imai, Y., Takeda, M., Wada, S. and Yamaguchi, T. [2008], 'Radial dispersion of red blood cells in blood flowing through glass capillaries: the role of hematocrit and geometry', *Journal of biomechanics* **41**(10), 2188–2196.

Schiller, U. D., Krüger, T. and Henrich, O. [2018], 'Mesoscopic modelling and simulation of soft matter', *Soft matter* **14**(1), 9–26.

Sousa, P., Pinho, F., Oliveira, M. and Alves, M. [2011], 'Extensional flow of blood analog solutions in microfluidic devices', *Biomicrofluidics* **5**(1), 014108.

Tang, Y.-H., Lu, L., Li, H., Evangelinos, C., Grinberg, L., Sachdeva, V. and Karniadakis, G. E. [2017], 'Openrbc: A fast simulator of red blood cells at protein resolution', *Biophysical journal* **112**(10), 2030–2037.

Yaginuma, T., Oliveira, M. S., Lima, R., Ishikawa, T. and Yamaguchi, T. [2013], 'Human red blood cell behavior under homogeneous extensional flow in a hyperbolic-shaped microchannel', *Biomicrofluidics* **7**(5), 054110.

Yasuda, K., Armstrong, R. and Cohen, R. [1981], 'Shear flow properties of concentrated solutions of linear and star branched polystyrenes', *Rheologica Acta* **20**(2), 163–178.

Ye, T., Phan-Thien, N. and Lim, C. T. [2016], 'Particle-based simulations of red blood cells-a review', *Journal of biomechanics* **49**(11), 2255–2266.

Chapter 5: Progress and Future Work

5.1 Introduction

The aim of this project was to investigate the development of a portable device that can process a whole blood sample into serum, infected red blood cells (RBCs), white blood cells (WBCs) and circulating tumour cells (CTCs) for ATR-FTIR spectroscopy. This chapter will summarise the findings and indicate future works and the potential of this project.

5.2 Summary of findings

As part of the design process (Chapter 2), we investigated the main components required for creating a microfluidic device; flow generation, separation of particles (active and passive), mixing methods of fluids and the potential manufacturing process. We have shown the need to understand these components in order to generate a feasible design and then presented the design process; firstly we considered the specification needed by ATR-FTIR spectroscopy, then the existing technology and conclude with a 4 stage design that prepares serum, infected RBCs, WBCs and CTCs for ATR-FTIR spectroscopy.

In Chapter 3 we have shown, by spiking pooled serum with different amounts of RBCs, the futility in quality testing serum without being coupled to a diagnostic test. By comparing spectra from plasma and serum samples, we have shown that plasma is a preferable sample type for ATR-FTIR spectroscopy than serum in point-of-care (POC) diagnostics. This is due to the time saved by avoiding clotting and that there is more variation in the spectra between subjects than

between plasma and serum using ATR-FTIR spectroscopy. Therefore, the device could produce plasma without the need to coagulate blood to form serum, which would result in a simpler system to design.

In order to aid investigation and optimisation of microfluidic channel designs for sample preparation, a phenomenological model has been developed based on the continuum effective medium (CEM) created in Ley and Bruus [2016]. The migration force was adapted to be a function of the shear gradient, governed by two material parameters: C_{mig} and b. The model, created in Chapter 4, follows the main trends of the experimental results but still needs to be suitably validated once further device experimentation has been undertaken. Parameters, C_{mig} and b, need to be determined by testing with more geometries, flow rates and hematocrit values. Once validated, the model can then be used to design plasma separation microfluidic modules more cost effectively by reducing the number of geometries needing to be manufactured and tested.

5.3 Final Thoughts

Sample preparation is usually integrated with a detection method, such as immunoassays, in a diagnostic device. As no specifications of sample properties are available in the literature for ATR-FTIR spectroscopy, only a generic universal blood preparation device to produce the requested outputs, serum, infected RBCs, WBCs and CTCs, could be envisaged. The technology is too premature to be used, as no market data, work flows or intended use statements are available to aid the design process.

The main blood product, that is used in ATR-FTIR spectroscopy, is serum but we have shown in Chapter 3 that for POC applications plasma is preferable. There are many existing solutions just for plasma separation that can be used (see section 2.4.2). The hand powered spinning disc plasma separator developed

by Bhamla et al. [2017], is a low cost and simple enough to be used by anyone and so is ideal for this application. Recently, Han and DeVoe [2020] developed a syringe, used for blood drawing, that can produce diluted plasma. Such a device would fit easily into the standard phlebotomy work flow and therefore, would easily be adopted. Infected RBCs have been tested for malaria in the field [Wood et al., 2014], but there is no indication for combined testing with other diseases. The sample preparation protocol requires methanol fixation which is incompatible with separating multiple cell types. There is limited literature on diagnostics using WBCs and CTCs with ATR-FTIR spectroscopy: therefore no specifications exist for these outputs. Sample preparation methods can only be commercially successful, in a competitive market, if the product carves out a niche application. Therefore, the device has to be optimised and integrated with a specific detection method. The main future step for this project is therefore to wait until the infrared clinical spectroscopy community has developed the intended use statement for a proposed device, as well as determined performance requirements for the outputs that could be designed for. Once this has occurred the work in this thesis provides an extremely useful guide for device development.

5.4 References

Bhamla, M. S., Benson, B., Chai, C., Katsikis, G., Johri, A. and Prakash, M. [2017], 'Hand-powered ultralow-cost paper centrifuge', *Nature Biomedical Engineering* **1**(1), 1–7.

Han, J. Y. and DeVoe, D. L. [2020], 'Plasma isolation in a syringe by conformal integration of inertial microfluidics', *Annals of Biomedical Engineering* pp. 1–10.

Ley, M. W. and Bruus, H. [2016], 'Continuum modeling of hydrodynamic particle–

particle interactions in microfluidic high-concentration suspensions', *Lab on a Chip* **16**(7), 1178–1188.

Wood, B. R., Bambery, K. R., Dixon, M. W., Tilley, L., Nasse, M. J., Mattson, E. and Hirschmugl, C. J. [2014], 'Diagnosing malaria infected cells at the single cell level using focal plane array fourier transform infrared imaging spectroscopy', *Analyst* **139**(19), 4769–4774.

Appendix A: Matlab code used in 1D CEM model in Chapter 4

This appendix contains the code for determining pressure for the COMSOL 1D CEM model

```
%% Script for COMSOL error between Carreau and CEM model
cd 'I:\Science\MS\users\students\Radhakrishnan_Pretheepan\
    Modelling\COMSOL model Files\Inertial focussing\
    Straight Channels\1D model'
%%
imagefolder=uigetdir;
%% Input
Q2=40; %(ul/min)
phi_0=0.10; %volume fraction initial

%% CEM Model finding Pu initalisation
C_migval=logspace(24,18,40);
nc=length(C_migval);
bvals=1:0.1:1.9;
nb=length(bvals);
w = (100:100:400)*10^6;
nw = length(w);
d = [10 30 50]*10^6;
nd=length(d);
l=(800:100:1000)*10^6;
nl=length(l);
% Pressure parameters
```

```
21 step_size=10;
22 x_mag=1;
23
24
25 %initialisation of pressure solution
26 Pu_sol=zeros(nd,nw);
27
28 %% CEM finding pressure
29 %This section finds pressure input for the COMSOL model so
       that the flow rate matches is consistent between the
     desired conditions and the model
30
31 % pressure initialisation
32 Pu_init=23;
33 for i=1:nl
34     for j=1:nw
35         mess=['Width = ',num2str(w(j)),' ',num2str(j),'/',
              num2str(nw),' : length = ', num2str(l(i))];
36         disp(mess)
37
38         try
39
40             if i==1 && j==1
41                 x=Pu_init; %1st pressure is set
42             elseif j==1
43                 x=Pu_sol(i 1,1); % if first value of Cmig
                      then use pressure solution of previous
                      Cmig value
```

```
44              else
45                  x=Pu_sol(i,j-1); % if subsequent b value
                        use pressure solution of previous b
                        value
46              end
47              disp(['pressure = ', num2str(x)])
48
49              %if i>=2 && isnan(Pu_sol(i-1,j))
50              %    disp(['Previous Cmig value NaN move to
                    next Cmig ', num2str(C_migval(i+1))])
51              %    Pu_sol(i,j)=NaN;
52              %    break
53              %end
54
55
56
57              Puvals=x-x_mag:x_mag/step_size:x+x_mag;
58              nPu=length(Puvals);
59              Q2val=zeros(1,nPu);
60
61              for k=1:nPu
62                  out = CEM_find_pressure_aspect_ratio(w(j),
                        l(i), d(2), C_migval(round(nc/2)),
                        bvals(6), Puvals(k), Q2, phi_0);
63                  Tabl_real= out.result.table('tbl1').
                        getReal;
64                  Q2val(k)=Tabl_real(end,2);
65              end
```

```
66
67          WL=0;
68          WL_fail=0;
69          while max(Q2val)<Q2 || min(Q2val)>Q2 %Q2
                outside range of Q2val
70          WL=WL+1;
71              if WL>1000 %break condition to prevent
                    infinite loop
72                  WL_fail=1;
73                  disp('reached iteration limit')
74                  break
75              end
76          disp(['while loop = ', num2str(WL)])
77          disp(['maxQ2val = ',num2str(max(Q2val)), '
                minQ2val= ',num2str(min(Q2val))])
78
79              if max(Q2val)<Q2
80                  x=x+x_mag;
81                  disp(['Pressure increased: P= ',
                        num2str(x)])
82              elseif min(Q2val)>Q2
83                  x=x x_mag;
84                  disp(['Pressure reduced: P= ',num2str(
                        x)])
85              else
86                  error('fail new Q2 range')
87              end
88              Puvals=x x_mag:x_mag/step_size:x+x_mag;
```

```
89                  %nPu=length(Puvals);
90                  Q2val=zeros(1,nPu);
91                  for k=1:nPu
92                      out = CEM_find_pressure_aspect_ratio(w
                            (j),l(i),d(2), C_migval(round(nc/2)
                            ), bvals(6), Puvals(k), Q2,phi_0);
93                      Tabl_real= out.result.table('tbl1').
                            getReal;
94                      Q2val(k)=Tabl_real(end,2);
95                  end
96              end
97              if WL_fail==1
98                  disp('pressure not found')
99                  Pu_sol(i,j)=NaN;
100                 break
101             else
102                 disp(['Final: maxQ2val =',num2str(max(
                        Q2val)), ' minQ2val=',num2str(min(Q2val
                        ))])
103                 Pu_sol(i,j)= interp1(Q2val,Puvals,Q2);
104             end
105             disp(['Pressure = ', num2str(Pu_sol(i,j))])
106         catch ME
107             disp(['Error move to next Cmig ', num2str(
                    C_migval(i+1))])
108             Pu_sol(i,j)=NaN;
109             break
110         end
```

```
111     end
112 end
113 disp('finished finding pressure')
114 % output Pu for CMig, b value
115
116 %% Extracting u velocity and particle distribution from
      CEM with correct Pressure
117 %This section runs the model with the correct pressure
      found in previous section and extract the
118 %velocity and particle distrubution data.
119
120 % input Loops for CMig, B,and Pu for each comnination
121 % output: U_CEM
122 for i=1:nl
123     mess1=['loop = ', num2str(i),' of ', num2str(nl)];
124     for j=1:nw
125         mess=[mess1,' loop = ', num2str(j),' of ', num2str
              (nw)];
126         disp(mess)
127         out = CEM_find_pressure_aspect_ratio(w(j),l(i),d
              (2), C_migval(round(nc/2)), bvals(6), Pu_sol(i,
              j), Q2,phi_0);
128         if i==1 && j==1
129             x_temp = mpheval(out, 'x');
130             x_vals=x_temp.d1(end,:);
131             vel_CEM=zeros(length(x_vals),nl,nw);
132             Conc_temp = mpheval(out, 'phi');
```

```
133                 Conc_CEM=zeros(size(Conc_temp.d1(end,:),2),nl,
                        nw);
134             end
135             Conc_temp = mpheval(out, 'phi');
136             Conc_CEM(:,i,j)=Conc_temp.d1(end,:)';
137             vel_temp = mpheval(out, 'u');
138             vel_CEM(:,i,j)=vel_temp.d1(end,:);
139         end
140 end
141 disp('Extracting Velocity and particle distribution form
      CEM finished')
142
143
144 %% Plotting velocity distibution
145 % Section just plots the velocity distribution
146
147 %1st dimension variation
148 figure (1)
149 leg =cell(nl,1) ;
150 for i=1:nl
151     %figure (i)
152     hold on
153     plot(x_vals,vel_CEM(:,i,round(nw/2)))
154     leg{i}=strcat('length:', num2str(l(i)*10^6),' um');
155 end
156 legend(leg)
157 xlabel('position from centreline')
158 ylabel('velocity')
```

```
159 hold off
160 %2nd Dimension variation
161
162 figure (2)
163 leg2 =cell(nw,1) ;
164 for i=1:nw
165     %figure (i)
166     hold on
167     plot(x_vals,vel_CEM(:,round(nl/2),i))
168     leg2{i}=strcat('width:', num2str(w(i)*10^6),' um');
169 end
170 legend(leg2)
171 xlabel('position from centreline')
172 ylabel('velocity')
173 hold off
174
175 %% Plotting Particle distibution
176 %This section just plots the particle distribution
177
178 %1st dimension variation
179 figure (3)
180 leg =cell(nl,1) ;
181 for i=1:nl
182     %figure (i)
183     hold on
184     plot(x_vals,Conc_CEM(:,i,round(nw/2)))
185     leg{i}=strcat('length:', num2str(l(i)*10^6),' um');
186 end
```

```
187 legend(leg)
188 xlabel('position from centreline')
189 ylabel('particle distribution')
190 hold off
191 %2nd Dimension variation
192
193 figure (4)
194 leg2 =cell(nw,1) ;
195 for i=1:nw
196     %figure (i)
197     hold on
198     plot(x_vals,Conc_CEM(:,round(nl/2),i))
199     leg2{i}=strcat('width:', num2str(w(i)*10^6),' um');
200 end
201 legend(leg2)
202 xlabel('position from centreline')
203 ylabel('particle distribution')
204 hold off
205 %% save workspace
206 Wfilename=('CEM_workspace');
207 Filename=fullfile(imagefolder,Wfilename);
208 save(Filename,'Q2','imagefolder','Pu_init','C_migval','
    bvals','comb','Pu_sol','x_vals','vel_CAR','vel_CEM','
    Final_error','Final_RE','step_size','x_mag','Min_error'
    ,'min_Cmig','min_b','min_Pu_sol','phi_0')
```

Appendix B: Presented posters

This appendix contains the posters presented over the course of the project

- Research presentation day 2016, Faculty of Engineering, University of Strathclyde
- Transmed Conference 2016, Edinburgh
- Centre for doctoral training in medical devices & health technologies networking event. 2016, Glasgow
- Scottish Fluid Mechanics Meeting 2017, University of Strathclyde
- Spec 2018 Conference , University of Strathclyde
- BioMedEng18, Imperial College London

Simple model for the separation of plasma from whole blood using inertial focussing

P. Radhakrishnan[1], Prof N.J. Mottram[2], Dr M.S.N. Oliveira[3], Dr M.J. Baker[4]

1- Medical Devices CDT, University of Strathclyde, **pretheepan.radhakrishnan@strath.ac.uk**
2- Department of Mathematics and Statistics, University of Strathclyde
3- Department of Mechanical and Aerospace Engineering, University of Strathclyde
3- Department of Pure and Applied Chemistry, University of Strathclyde

University of Strathclyde Engineering

1. Introduction

Inertial Focussing:

- In low aspect ratio (height / width) rectangular channels, particles stabilise in two regions determined by the balance of forces between wall effects (F_w) and flow shear gradient (F_s).

Aim

- Generate a model of inertial focussing that has a reduced computational load compared to the existing 3D models.

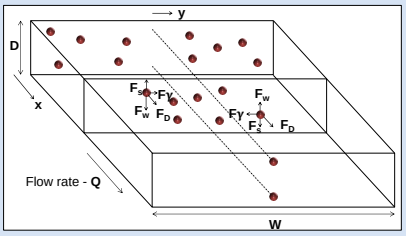

Figure 1: Schematic showing effect of inertial focussing on particles. Dashed lines are the particle equilibrium positions

3. Model

A 2D phenomenological model to simulate inertial focussing from plan view using COMSOL5.2 with MATLAB

- Two step model
  - 1st step : fluid flow model – stationary time solver
  - 2nd step: particle tracing – time-dependent solver

Fluid Flow

- Stokes' Flow
- $u\_inlet = \frac{12Q}{DW^3}(y^2 - \left[\frac{W}{2}\right]^2)$

Particle flow

- Force on Particles:

$$F = F_\gamma + F_D$$

$$C_{mig}\left(\frac{du}{dy}\right)^a$$ Stokes' drag

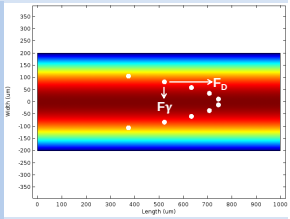

Figure 2: COMSOL plot showing particles (white) overlapped with velocity surface plot (red higher speed)

Results:

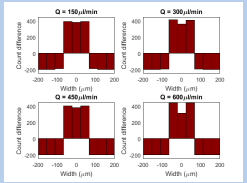

Figure 3: Particle distribution difference at outlet between C_{mig} = 4x10^{-12} and C_{mig}=0 (a=1) for different flow rates at Length 1mm.

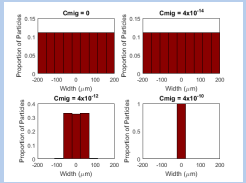

Figure 4: Particle distribution at outlet for different values of C_{mig} (a=1) at length 1mm. Q=150μl/m^3.

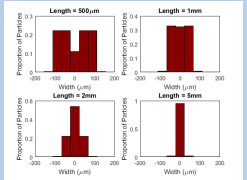

Figure 5: particle distribution at outlet for different lengths. For Q= 150μl/m^3 and C_{mig} = 4x10^{-12} (a=1)

Summary of results

- Increasing velocity does not increase the effect of C_{mig}
- Increasing C_{mig} decreases particle spread at outlet
- Increasing channel length allows particles to concentrate

4. Experimental

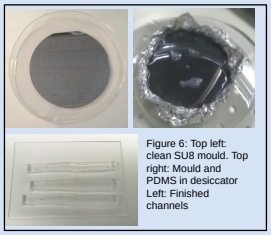

Figure 6: Top left: clean SU8 mould. Top right: Mould and PDMS in desiccator Left: Finished channels

Manufacturing of Channels:

- Straight channels made of PDMS (Sylgard 184)
- Bound to Microscope Slide 76 x 110mm (LOGITECH) using plasma system

Experimental set up:

- Inverted Light Microscope (Olympus IX71)
- Syringe Pump (Harvard Apparatus PHD 2000)
- Figures 8 is example of raw image of particles taken.
- 10μm polystyrene tracer particles used

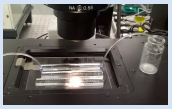

Figure 7: Channels with attached inlet and outlet tubes on stage

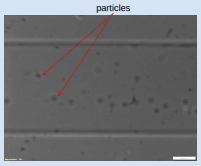

Figure 8: An example of a raw image of particle taken near outlet.

5. Future Work

- Measure the outlet particle distribution from experiments
- Validate model by determining the value for the C_{mig} and a coefficients.
- Testing with blood

Acknowledgements

Colleague Joana Sales Fidalgo for designing and manufacturing SU8 mould needed for creating the straight channel.

EPSRC Engineering and Physical Sciences Research Council

Figure B.1: Poster presented at Strathclyde Engineering faculty research presentation day 2016

Simple model for the separation of plasma from whole blood using inertial focussing

Pretheepan. Radhakrishnan[1], Prof Nigel.Mottram[2], Dr Mónica Oliveira[3], Dr Matthew Baker[4]

1- Medical Devices CDT, University of Strathclyde, Glasgow, **pretheepan.radhakrishnan@strath.ac.uk**
2- Department of Mathematics and Statistics, University of Strathclyde
3- Department of Mechanical and Aerospace Engineering, University of Strathclyde
4- Department of Pure and Applied Chemistry, University of Strathclyde

University of Strathclyde Engineering

1. Introduction

Blood:

- Most easily accessible biofluid for diagnostic tests.
- Disease biomarkers from all over the body can collect in the blood and be detected.
- Blood is 55% Plasma of which 92% is water
- Rest is composed of cells and cellular structures

Inertial Focussing[1]:

- In low aspect ratio (height / width) rectangular channels, particles stabilised in two regions. Balance of forces between wall effects (F_w) and flow shear gradient (F_s).

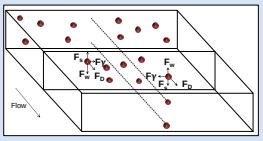

Figure 1: Schematic showing effect of inertial focussing on particles. Dashed lines are the particle equilibrium positions

2. Motivation

- Point of care devices in remote regions need to be able to prepare samples on site.
- Microfluidics provide simple process using small sample volumes
- The proposed model provides a tool with reduced computational load for designing microfluidic channels using inertial focussing compared to 3D models[2].

3. Model

A 2D phenomenological model to simulate inertial focussing from plan view using COMSOL5.2 with MATLAB

- Two Step model
  - 1st step : Fluid Flow Model – Stationary time solver
  - 2nd step: Particle Tracing – Timed dependent solver

Fluid Flow

- Stokes Flow
- Boundary conditions:

$$u\_inlet = \frac{12Q}{DW^3}\left(y^2 - \left[\frac{W}{2}\right]^2\right)$$

Normal outlet flow: P= 0Pa

Where u_inlet is the inlet velocity profile, Q is flow rate, D is channel depth, W is the channel width, y is the y position and P is pressure.

Particle flow

- Force on Particles:

$$F = F_Y + F_D$$

$C_{mig}\frac{du}{dy}$ — Stokes drag

Model Parameters

Parameter	Value
Width	400µm
Depth	50µm
Viscosity	3E-3Pa.s
Fluid Density	1025kg.m^{-3}
Particle Density	1125kg.m^{-3}
Particle Diameter	10µm
Number of Particles	9

Table 1: Shows the parameter values used in the model

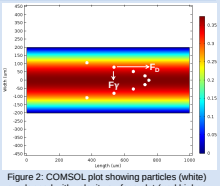

Figure 2: COMSOL plot showing particles (white) overlapped with velocity surface plot (red higher speed)

Results:

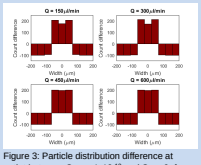

Figure 3: Particle distribution difference at outlet between C_{mig} = 4x10^{-12} and C_{mig}=0 for different flow rates at Length 1mm.

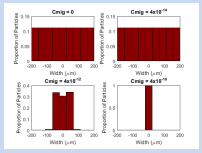

Figure 4: Particle distribution at outlet for different values of C_{mig} at length 1mm. Q=150ul/m^3.

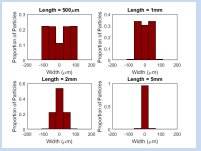

Figure 5: particle distribution at outlet for different lengths. For Q= 150ul/m^3 and C_{mig} = 4x10^{-12}

Summary of results

- Increasing velocity does not increase the effect of C_{mig}
- Increasing C_{mig} decreases particle spread at outlet
- Increasing channel length allows particle to concentrate

4. Experimental

Manufacturing of Channels:

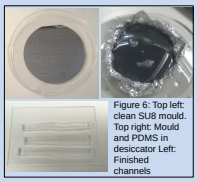

Figure 6: Top left: clean SU8 mould. Top right: Mould and PDMS in desiccator Left: Finished channels

- Externally made SU8 mould
- PDMS (Sylgard 184) mixed with curing agent (ratio 1:9) and poured into mould
- Placed in desiccator to remove bubbles
- Cured in Oven 80^{0}C for 20 mins
- Bound to Microscope Slide 76 x 110mm (LOGITECH) using plasma system

Experimental set up:

Figure 7: Channels with attached inlet and outlet tubes on stage

- Inverted Light Microscope (Olympus IX71)
- Syringe Pump (Harvard Apparatus PHD 2000)

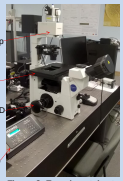

Figure 8: Experimental set up

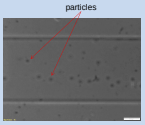

Figure 9: Image showing particle flow near outlet.

- Figures 9 is example of raw image of particles taken.
- Particles used 10um spheromeres

5. Still To Do

- Measure the outlet particle distribution from experiments
- Validate model by determining the value for the C_{mig} coefficient
- Testing with blood

References

1) Di Carlo D. Inertial microfluidics. Lab Chip. 2009;9(21):3038–46.
2) Martel J, Toner M. Modelling Inertial Focusing in Straight and Curved Microfluidic Channels. COMSOL News. 2013;42–3.

Acknowledgements

Pretheepan Radhakrishnan would like to acknowledge the EPSRC for funding via the Medical Devices CDT, University of Strathclyde.
Colleague Joana Sales Fidalgo for designing and manufacturing SU8 mould needed for creating the straight channel.

EPSRC Engineering and Physical Sciences Research Council

Figure B.2: Poster presented at Transmed conference 2016

Blood Partitioning for Spectral Disease Detection using Microfluidic Devices

P. Radhakrishnan[1], Dr M.J. Baker[2], Prof N.J. Mottram[3], Dr M.S.N. Oliveira[4]

1- Medical Devices CDT, University of Strathclyde, **pretheepan.radhakrishnan@strath.ac.uk**
2- Department of Pure and Applied Chemistry, University of Strathclyde
3- Department of Mathematics and Statistics, University of Strathclyde
4- Department of Mechanical and Aerospace Engineering, University of Strathclyde

Introduction

- Attenuated total reflection Fourier transform infrared spectroscopy (ATR-FTIR) is a small sample volume (1µl) technique able to analyse blood samples.
- The peaks in the absorbance spectra (right) indicate different molecule types
- There is a difference in the location of peaks between healthy and disease samples which algorithms can use to detect the difference.
- The steps of the diagnostic process are shown below:

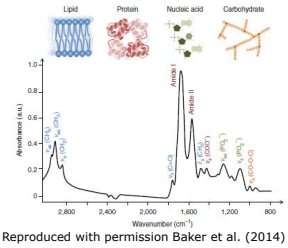

Reproduced with permission Baker et al. (2014)

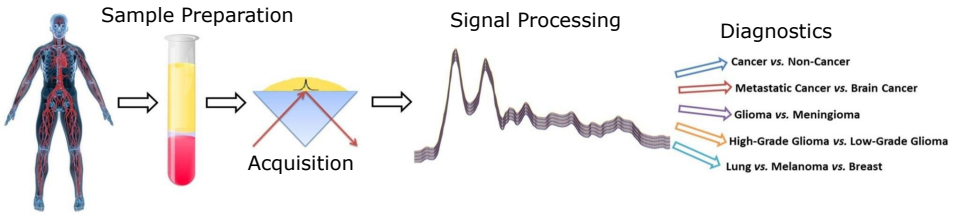

Aim

Develop a microfluidic platform that can separate a single blood sample into components that can be analysed by ATR-FTIR

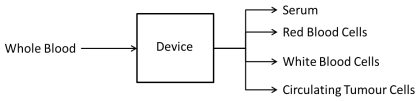

A limitation of the current protocol for point of care diagnostics is the preparation of the blood sample.

Application

Still many people around the world do not have access to basic healthcare. This device combined with ATR-FTIR can provide a more cost effective method of initial diagnostic tests in the field.

Benefits:

- Rapid sample preparation and diagnostic results
- Device useable in remote hospitals and clinics
- Rapid deployment to makeshift clinics in emergency situations such as the Ebola crisis.

Research:

Determining serum output

Dilution of samples may effect the ability to detect disease. Different concentrations of PBS and serum was analysed by ATR-FTIR. A spectral quality test was set up to find the limit of dilution for serum.

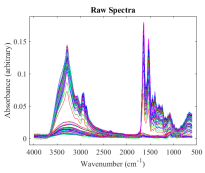

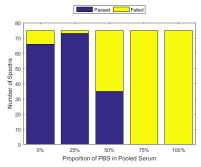

Results from Quality test

Microfluidics

Inertial focussing is a possible method of separating plasma form blood. Two models were created to simplify inertial focussing to two dimensions. A discrete particle model (right) and a single phase model(below).

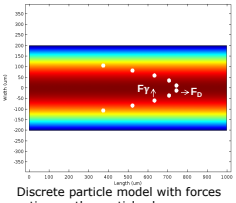

Discrete particle model with forces acting on the particle shown over fluid flow field

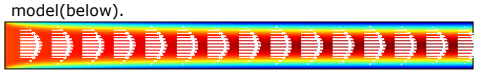

Single phase model showing concentration field with fluid velocity indicated by arrows

References
Baker, M.J. et al., 2014. Nature protocols, 9(8), pp.1771–91.

EPSRC Engineering and Physical Sciences Research Council

Figure B.3: Poster presented at Medical devices and healthcare technologies CDT networking event

A 1D phenomenological model for plasma skimming in a microfluidic device

P. Radhakrishnan[1], Prof N.J. Mottram[2], Dr M.S.N. Oliveira[3] ,Dr M.J. Baker[4]
1- CDT in Medical Devices & Healthcare Technologies, Department of Biomedical Engineering, University of Strathclyde,
pretheepan.radhakrishnan@strath.ac.uk
2-Department of Mathematics and Statistics, University of Strathclyde
3- James Weir Fluids Laboratory, Department of Mechanical and Aerospace Engineering, University of Strathclyde
4-Department of Pure and Applied Chemistry, University of Strathclyde

University of Strathclyde Engineering

1) Introduction

- Plasma: liquid component of blood, contains diagnostically useful markers.
- Red blood cells: make up ~45% of blood, can hinder disease markers form detection.
- Cell free layer (CFL) forms during blood flow, described by the Fahraeus effect.
- Collecting plasma from the CFL is known as plasma skimming.
- Microfluidics allow detection from small volume resulting in faster test results.
- Ley and Bruus[1] used the continuum effective medium model (CEM), where migration depends on an external force; F_{mig}.

Aim

- Develop a CEM model to use as a predictive tool for device design.
- Validate against the Carreau viscosity model.

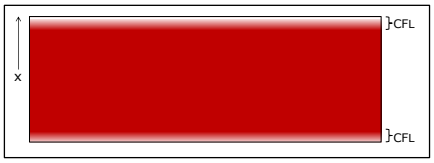

Schematic of blood flow in channel showing CFL region

2) Model:

A non-dimensional 1D CEM model was develop using a migration dependent on shear gradient:

$$F_{mig} = C_{mig}(\nabla \bar{u})^b$$

where coefficient of migration (C_{mig}) and shear exponent (b) are parameters that need to be determined.

The governing equations are solved with COMSOL.

Momentum Conservation:

$$\bar{\rho}\frac{\partial \bar{u}}{\partial \bar{t}} + \bar{\rho}(\bar{u}\cdot\nabla)\,\bar{u} = \frac{-\bar{p}}{L} + \frac{1}{\mathrm{Re}_w}\,\bar{\mu}\frac{d\bar{u}}{dx}$$

Fluid Mass Conservation:

$$\frac{\partial\,\bar{\rho}}{\partial\,\bar{t}} = -\frac{d(\bar{\rho}\bar{u})}{dx}$$

Cell Mass Conservation:

$$d_a\frac{\partial \phi}{\partial \bar{t}} = \frac{d}{dx}\left[\nabla\phi + A\cdot\mathrm{sign}(x)\left(\left|\frac{d\bar{u}}{dx}\right|\right)^b\cdot\phi\right]$$

where $A = \frac{\mathrm{Pe}\cdot\mathrm{St}\cdot\nu(\phi)}{D(\phi)}$

Constitutive equations[2]:

Viscosity:
$$\bar{\mu}(\phi) = (1 + \mathrm{M}_1\phi + \mathrm{M}_2\phi^2 - \mathrm{M}_3\phi^3 + \mathrm{M}_4\phi^4)$$

Diffusivity:
$$D(\phi) = (1 + \mathrm{D}_1\phi + \mathrm{D}_2\phi^2 - \mathrm{D}_3\phi^3 + \mathrm{D}_4\phi^4)^{-1}$$

Motility:
$$\nu(\phi) = (1 + \mathrm{N}_1\phi + \mathrm{N}_2\phi^2 - \mathrm{N}_3\phi^3 + \mathrm{N}_4\phi^4)^{-1}$$

Density:
$$\bar{\rho} = (1-\phi) + \mathrm{B}\phi$$

Parameters:

Reynolds number: $\mathrm{Re} = \frac{\mu_w}{UL\rho_w}$

Péclet Number: $\mathrm{Pe} = \frac{L\,U}{D_0}$

Strouhal Number: $\mathrm{St} = \frac{U^{b-1}}{L^b}\nu_0 C_{mig}$

Buoyancy Constant: $\mathrm{B} = \frac{\rho_p}{\rho_w}$

3) Validation:

We compared the 1D CEM model to a dimensionless Carreau viscosity model (Re= 6.35):

$$\bar{\mu}_c = \frac{1}{\mu_w}\cdot(\mu_{inf} + (\mu_0 - \mu_{inf})\cdot(1 + (\lambda\nabla\bar{u})^2)^{\frac{n-1}{2}}$$

where μ_0 is the zero shear rate viscosity,
μ_{inf} is the infinite shear rate viscosity,
λ and n are empirical parameters.

The relative error (RE) was calculated:

$$RE = \frac{\int \mathrm{abs}(\bar{u}_{CEM}(x) - \bar{u}_{car}(x))\,dx}{\int \bar{u}_{car}\,dx}$$

where $\bar{u}_{CEM}$ is the velocity from CEM model
$\bar{u}_{car}$ is from the Carreau model.

4) Results:

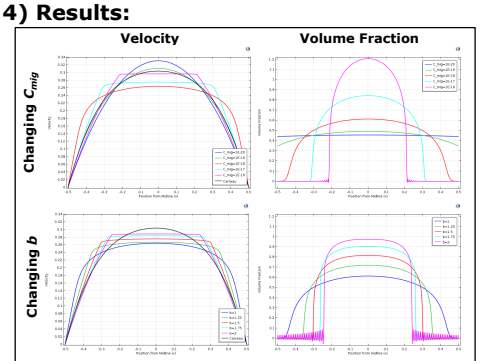

C_{mig} increases CFL, b decreases interface thickness

5) Discussion and Future Work:

- Model parameters C_{mig} and b affect the CFL
- We find best fit when C_{mig} = 1×10^{-19}Ns and b = 1
- We plan to extend this to 2D and model plasma skimming devices

References
1) M. W. H. Ley and H. Bruus, *Lab Chip*, 2016, **16**, 1178–1188.
2) A. J. C. Ladd, *J. Chem. Phys.*, 1990, **93**, 3484.

EPSRC
Engineering and Physical Sciences Research Council

Figure B.4: Poster presented at Scottish Fluid Mechanics Meeting 2017

Developing a microfluidic blood preparation device for ATR-FTIR spectroscopy

P. Radhakrishnan[1], Prof N.J. Mottram[2], Dr M.S.N. Oliveira[3], C. Jenkins[4], Dr M.J. Baker[4]
1-Medical Devices CDT, University of Strathclyde, Glasgow, UK, **pretheepan.radhakrishnan@strath.ac.uk**
2-Department of Mathematics and Statistics, University of Strathclyde, Glasgow, UK
3-James Weir Fluids Laboratory, Department of Mechanical and Aerospace Engineering, University of Strathclyde, Glasgow, UK
4-WestChem, Department of Pure and Applied Chemistry, University of Strathclyde, Glasgow, UK

University of Strathclyde Engineering

1) Introduction

ATR-FTIR spectroscopy has great potential as a biofluid diagnostic technique. For ATR-FTIR spectroscopy to be used as a point of care diagnostic technology, processing samples has to be carried out on site.
This work has conceptualised a microfluidic device to process a single blood sample (10ml) to multiple diagnostic outputs.

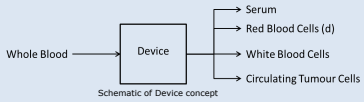

Schematic of Device concept

The numerical tool being developed in this project will help in the design of microfluidic modules to separate healthy red blood cells (RBCs) from the diagnostic fluid based on the Fahraeus-Lindquist effect.

Healthy RBCs make up majority of the sample, provide limited diagnostic information and therefore needs to be removed.

The model has low computational cost allowing for adoption in industry and reduction in the cost for module commercialisation

2) Model:

We want to model concentration and velocity of RBCs flowing in microfluidic channels.

COMSOL Multiphysics was used to solve the model equations[1] for investigating cell free regions. The migration force on the RBCs is given as:

$$F_{mig} = C_{mig}(\nabla u)^b$$

where C_{mig} and b are parameters that need to be determined.

The governing equations for velocity($\bar{u}$), pressure ($\bar{p}$) and concentration ($c = e^s$) are given below:

$$\bar{\rho}(\phi)\frac{\partial \bar{u}}{\partial \bar{t}} + \bar{\rho}(\phi)(\bar{u}\cdot\nabla)\,\bar{u} = \nabla\cdot(-\bar{p}) + \frac{1}{Re_w}\bar{\mu}(\phi)\,\nabla^2\,\bar{u}$$

$$\frac{\partial\,\bar{\rho}(\phi)}{\partial\,\bar{t}} = -\nabla\cdot(\bar{\rho}(\phi)\bar{u})$$

$$c\frac{\partial s}{\partial \bar{t}} = \nabla\cdot\left[\frac{1}{Pe}D(\phi)\bar{c}\,\nabla s - c\bar{u} - Stcv(\phi)(|\nabla\bar{u}|)^b\right]$$

The material properties; viscosity ($\bar{\mu}(\phi)$), diffusivity ($D(\phi)$), motility ($v(\phi)$) and density ($\bar{\rho}(\phi)$) are functions of volume fraction (ϕ) and are given in the constitutive equations[2]:

$$\bar{\mu}(\phi) = (1 + M_1\phi + M_2\phi^2 - M_3\phi^3 + M_4\phi^4)$$

$$D(\phi) = (1 + D_1\phi + D_2\phi^2 - D_3\phi^3 + D_4\phi^4)^{-1}$$

$$v(\phi) = (1 + N_1\phi + N_2\phi^2 - N_3\phi^3 + N_4\phi^4)^{-1}$$

$$\bar{\rho}(\phi) = (1 - \phi) + B\phi$$

Dimensionless parameters:

$$Re = \frac{\mu_w}{UL\rho_w} \quad Pe = \frac{L\,U}{D_0} \quad V = \frac{4}{3}\pi a^3 C \quad B = \frac{\rho_p}{\rho_w}$$

$$St = \frac{U^{b-1}}{L^b}v_0 C_{mig}$$

3) Experimental Validation:

- Red blood cell in Saline at 10%, 20% and 40% Haematocrit (HCT)
- Flow rate (Q) of 10µl/min, 40µl/min, 100µl/min
- 3 types of Microfluidic contraction channels used

ID	L (cm)	w (µm)	h (µm)	l (µm)	c (µm)
1	2	400	100	90	50
2	2	400	100	500	50
3	2	400	100	90	100

Dimensions of Channels used

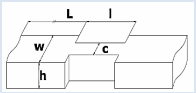

Schematic of channel dimensions

4) Results:

Numerical Simulations

Concentration (ratio of inlet) surface plot with velocity vectors and streamlines at steady state.

Experimental Validation

The average frame intensity of videos taken at steady state are presented below.

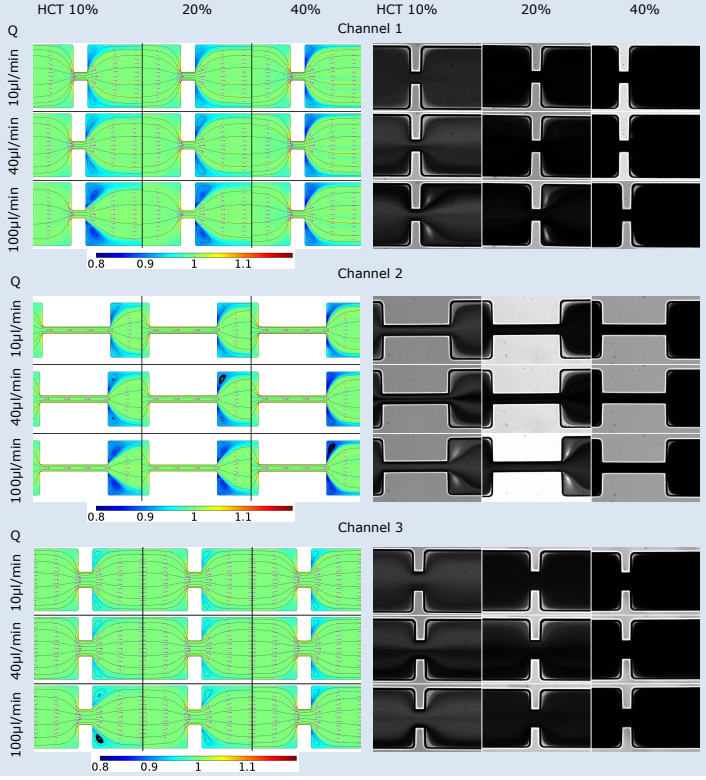

5) Conclusion

- Single simulation takes of the order 10 minutes on standard PC (intel i5) making it accessible to all.
- High flow rates causes recirculation of RBCs and needs to be avoided.
- The size of the cell free regions decreases with increasing HCT.
- Model still being developed to get better correlation with experiment.

References
1 M. W. H. Ley and H. Bruus, *Lab Chip*, 2016, **16**, 1178–1188
2 A. J. C. Ladd, *J. Chem. Phys.*, 1990, **93**, 3484.

EPSRC Engineering and Physical Sciences Research Council

Figure B.5: Poster presented at SPEC 2018 conference

Developing a microfluidic blood preparation device for ATR-FTIR spectroscopy

P. Radhakrishnan[1], Prof N.J. Mottram[2], Dr M.S.N. Oliveira[3], C. Jenkins[4], Dr M.J. Baker[4]
1-Medical Devices CDT, University of Strathclyde, Glasgow, UK, **pretheepan.radhakrishnan@strath.ac.uk**
2-Department of Mathematics and Statistics, University of Strathclyde, Glasgow, UK
3-James Weir Fluids Laboratory, Department of Mechanical and Aerospace Engineering, University of Strathclyde, Glasgow, UK
4-WestChem, Department of Pure and Applied Chemistry, University of Strathclyde, Glasgow, UK

University of Strathclyde Engineering

Introduction

- Attenuated total reflection Fourier transform infrared spectroscopy (ATR-FTIR) is a small sample volume (1µl) technique able to analyse blood samples.
- The peaks in the absorbance spectra can indicate different molecule types
- There is a difference in the location of peaks between healthy and disease samples which algorithms can use to detect the difference.
- The steps of the diagnostic process are shown on right:

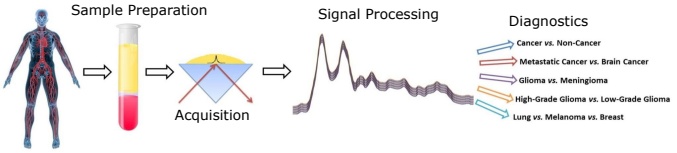

Aim:

Develop a microfluidic platform that can separate a single blood sample into components that can be analysed by ATR-FTIR

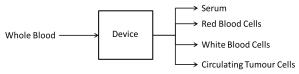

A limitation of the current protocol for point of care diagnostics is the preparation of the blood sample.

Application:

Still many people around the world do not have access to basic healthcare. This device combined with ATR-FTIR can provide a more cost effective method of initial diagnostic tests in the field.

Benefits:

- Rapid sample preparation and diagnostic results
- Device useable in remote hospitals and clinics
- Rapid deployment to makeshift clinics in emergency situations such as the Ebola crisis.

Design:

A modular design intended to maximise purity while minimising the number of processing steps is presented below:

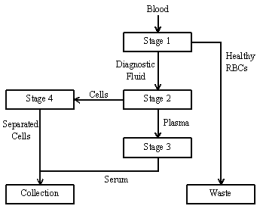

For developing stage 1, a numerical tool being developed in this project will help in the design of microfluidic modules to separate healthy red blood cells (RBCs) from the diagnostic fluid based on the Fahraeus-Lindquist effect.

Another aspect that was looked at stage 3. This stage involves the conversion of a plasma like fluid to serum. The monitoring of this change with ATR-FTIR spectroscopy was investigated.

Stage 1: Developing Numerical Model

The model has low computational cost allowing for adoption in industry and reduction in the cost for module commercialisation. We want to model concentration and velocity of RBCs flowing in microfluidic channels.
COMSOL Multiphysics was used to solve the model equations[1] for investigating cell free regions. The migration force on the RBCs is given as:

$$F_{mig} = C_{mlg}(\nabla u)^b$$

where C_{mig} and b are parameters that need to be determined.
The governing equations for velocity($\bar{u}$), pressure ($\bar{p}$) and concentration ($c = e^s$) are given below:

$$\bar{\rho}(\phi)\frac{\partial \bar{u}}{\partial t} + \bar{\rho}(\phi)(\bar{u}\cdot\nabla)\,\bar{u} = \nabla\cdot(-\bar{p}) + \frac{1}{Re_w}\,\bar{\mu}(\phi)\,\nabla^2\,\bar{u}$$

$$\frac{\partial\,\bar{\rho}(\phi)}{\partial\,t} = -\nabla\cdot(\bar{\rho}(\phi)\bar{u})$$

$$c\frac{\partial s}{\partial t} = \nabla\cdot\left[\frac{1}{Pe}D(\phi)\bar{c}\,\nabla s - c\bar{u} - Stcv(\phi)(|\nabla\bar{u}|)^b\right]$$

The material properties; viscosity ($\bar{\mu}(\phi)$), diffusivity ($D(\phi)$), motility ($v(\phi)$) and density ($\bar{\rho}(\phi)$) are functions of volume fraction (ϕ) and are given in the constitutive equations[2]:

$$\bar{\mu}(\phi) = (1 + M_1\phi + M_2\phi^2 - M_3\phi^3 + M_4\phi^4)$$
$$D(\phi) = (1 + D_1\phi + D_2\phi^2 - D_3\phi^3 + D_4\phi^4)^{-1}$$
$$v(\phi) = (1 + N_1\phi + N_2\phi^2 - N_3\phi^3 + N_4\phi^4)^{-1}$$
$$\bar{\rho}(\phi) = (1-\phi) + B\phi$$

Results:

Simulation (top) and experiments (below) carried out while changing the haematocrit (HCT) and flow rate (µl/min) (Q)

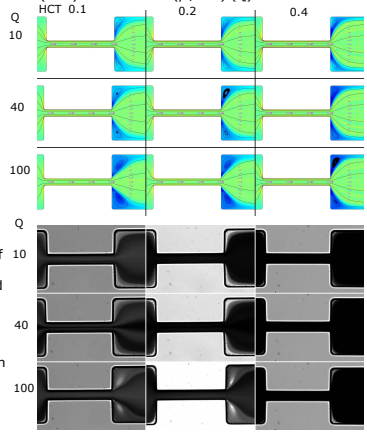

Stage 3: ATR-FTIR spectroscopic sample characteristics

Spectra was collected on Spectrum 2 (Perkin Elemer, USA) of frozen patient plasma and serum samples. A separate experiment on fresh volunteer plasma and serum samples was analysed for comparison

Processing of the spectra consisted of:

- mean spectra for each machine replicate
- rubber band baseline correction
- noise reduction
- vector normalisation
- Savisky-Golay algorithm was used to calculate the second derivative spectra.
- The carbon dioxide spectral bands (2403-2272cm^{-1} and 682-655 cm^{-1}) were removed.
- Principle component discriminant functional analysis.

Results:

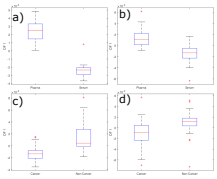

Figure showing PC-DFA plots for Patient samples: a) Cancer: plasma vs serum b) Non-Cancer: plasma vs serum c) Plasma: Cancer vs Non Cancer d) Serum: Cancer vs Non Cancer

Only figure a) shows separation

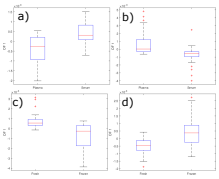

Figure showing PC-DFA plots for volunteer samples: a) Fresh: plasma vs serum b) Frozen: plasma vs serum c) Plasma: Fresh vs Frozen d) Serum: Fresh vs Frozen

No separation can be seen form any of the combinations

ATR-FTIR spectra for Plasma and Serum samples are very similar

Conclusion and Future work:

- Numerical model is still being developed. Validation with experiment is being carried out.
- Determined that using plasma is a better sample to use for Point of care diagnostics
- Once the model is suitably developed designing of stage 1 can be started.
- The other stages of the presented design will need to be developed.

EPSRC Engineering and Physical Sciences Research Council

Figure B.6: Poster presented at BIOMEDENG 2018 conference